DIRECT FIELD-FEEDBACK CONTROL FOR PERMANENT MAGNET SPHERICAL MOTORS

A Dissertation
Presented to
The Academic Faculty

By

Kun Bai

In Partial Fulfillment
Of the Requirements for the Degree
Doctor of Philosophy in the
School of Mechanical Engineering

Georgia Institute of Technology

December 2012

DIRECT FIELD-FEEDBACK CONTROL FOR PERMANENT MAGNET SPHERICAL MOTORS

Approved by:

Dr. Kok-Meng Lee, Advisor
School of Mechanical Engineering
Georgia Institute of Technology

Dr. Magnus Egerstedt
School of Electrical and Computer Engineering
Georgia Institute of Technology

Dr. Nader Sadegh
School of Mechanical Engineering
Georgia Institute of Technology

Dr. David G. Taylor
School of Electrical and Computer Engineering
Georgia Institute of Technology

Dr. Jun Ueda
School of Mechanical Engineering
Georgia Institute of Technology

Date Approved: August 22, 2012

==========

ACKNOWLEDGEMENTS

First of all, I would like to sincerely thank my advisor Dr. Kok-Meng Lee for being a constant source of encouragement throughout this research. He is very knowledgeable and his enthusiasm to seize and realize new ideas has always inspired me and played a vital role in the successful completion of this thesis.

It is also my pleasure thank my thesis committee members Dr. Magnus Egerstedt, Dr. Nader Sadegh, Dr. David G. Taylor, and Dr. Jun Ueda for their time and efforts as well as valuable insights on this thesis.

I also want to thank John Graham, Louis Boulanger and students at the ME machine shop for their help with experimental test-beds of a spherical motor; and Vladimir Bortkevich, Kyle French and students at the ME Electronics Lab for their help with current amplifiers.

During this research, I have also obtained suggestions and help from the former team members Dr. Hungsun Son, Dr. Chih-Hsing Liu, Dr. Shaohui Foong; and fellow students Jiajie Guo, Daxue Wang, Jungyoul Lim, Yang Xie, Xianmin Chen, Min Li, Chun-Yeon Lin, Ying Chen, Jingjing Ji. Their assistances on this research are greatly appreciated.

Throughout my life and educational career, my parents Guangzhi Bai and Huirong Sun have been an endless source of love and encouragement. I would like to thank for their support and understanding. Without their encouragement it would have been impossible for me to complete this work.

The financial support from the Korea Institute of Machinery and Materials (KIMM), the US Poultry and Eggs Association, the Georgia Agriculture Technological Research Program (ATRP), and National Science Foundation (NSF) is gratefully acknowledged.

TABLE OF CONTENTS

LIST OF TABLES

LIST OF FIGURES

NOMENCLATURE

Capital Symbols

B	Magnetic flux density
H	Magnetic field intensity
I	Motor inertia
J	Current density
[K]	Torque characteristic matrix
K	Torque characteristic vector
$\mathbf{K}_P$, $\mathbf{K}_I$, $\mathbf{K}_D$	Controller gain matrices
M_0	Magnetization strength of permanent magnet
[**M**]	Inertia matrix
N_E	Number of electromagnets
N_P	Number of permanent magnets
N_W	Number of turns in the winding of an EM
S	Sensor index vector
T	Motor torque
$T_\alpha, T_\beta, T_\gamma$	α, β, γ component of torque
XYZ	Stator coordinate frame
Θ, Φ, R	Stator spherical coordinates
Γ	Bijective domain
Ω	MFD-defined domain
Φ	Magnetic scalar potential

Lower Case Symbols

g	Gravity torque vector
i_j	Current input of $j^{th.}$ stator EM
m	Magnetic dipole strength
n	Normal vector
q	Rotor orientation
u	Current input vector
xyz	rotor coordinate
α, β, γ	XYZ Euler angles
θ, ϕ, r	Rotor spherical coordinates
λ	Pole separation angle
μ	Permeability of magnetic material
μ_o	Permeability of free space (air)

Abbreviations

DC	Direct current
DFC	Direct field-feedback control
DMP	Distributed multi pole
DOF	Degree of freedom
EM	Electromagnetic magnet
MFD	Magnetic flux density
PMSM	Permanent magnet
PMSM	Permanent magnet spherical motor
TCV	Torque characteristic vector
WCR	Weight compensating regulator

SUMMARY

There are emerging requirements for high accuracy multi-DOF actuators in numerous applications. As one of the novel motors capable of multi-DOF manipulation, permanent magnet spherical motors (PMSMs) that can provide continuous and dexterous motion in one joint have been widely studied for their advantages in structure and energy efficiency. The demands to bring forward the performance of PMSMs for precision applications have motivated this thesis to develop a closed-loop orientation control system with high accuracy and bandwidth.

Unlike traditional control methods for PMSMs, which rely on explicit orientation feedback, a new control method (referred to here as direct field-feedback control or in short DFC) directly utilizing the magnetic fields for feedback have been developed in this thesis. Because magnetic field measurements are almost instantaneous and the need for real-time orientation estimation is eliminated in DFC, the system sampling time is greatly reduced. Meanwhile, several field-based methods have been developed for the major components in the DFC system and each component can be processed independently and concurrently with the magnetic field measurements. The parallel computation further improves the system bandwidth and also reduces accumulated error. The DFC system has been experimentally implemented and evaluated. The results show excellent control performances in terms of accuracy and bandwidth.

To facilitate the design and analysis of the DFC system, several new algorithms have been developed, which include the modeling and computing of magnetic fields as well as forces and torques, an analysis of bijective relationship between orientation and magnetic fields, and a method for calibration and reconstruction of the rotor

magnetic field in 3 dimensional space. These algorithms not only enable the implementation of the DFC system for a PMSM, but also benefit the PMSM studies in design, modeling and field-based sensing.

While the immediate outcome of this research is a control system for PMSMs, this new control method can be applied to a broad spectrum of electromagnetic motion systems.

CHAPTER 1

INTRODUCTION

1.1 Background and Motivation

Recent advances in intelligent flexible manufacturing, robotics and bio-medicine have necessitated the further development of multiple degree-of-freedom (DOF) actuators with continuous and smooth motion, high accuracy as well as volumetric torque capacity. In modern manufacturing industries, the trend to downscale equipment for manufacturing products on "desktops" [1] has motivated the development of platforms capable of performing various machining tasks. One typical example is a micro-factory system [2] as shown in Figure 1.1(a), which consists of a high speed spindle cutter and a multi-DOF rotational stage. The position and/or orientation of a work piece mounted on the stage can be adjusted and the work piece can actively cooperate with the feeding motion of the cutter in order to accomplish complicated machining. It is required that the actuator driving the stage can offer dexterous motion in negotiating the orientation of the work piece. Figure 1.1(b) shows a live-object handling system [3] which presents another example where such multi-DOF actuators are desired. In this system, live-objects (such as birds) transferred from a prior conveyor are separated and re-orientated by the drums (equipped with flexible fingers) so that the birds can be individually delivered to the shackling line. As the body sizes of the birds vary, it is desired that the drums can tilt while they rotate so that the fingers are adaptive to the body variations in this process where the smooth cradling is essential to minimize injury. There are also a variety of

industrial applications, such as robotic joints (as shown in Figure 1.1c) as well as stereoscopic active vision systems (as shown in Figure 1.1d), where multi-DOF orientation must be achieved rapidly, continuously and uniformly.

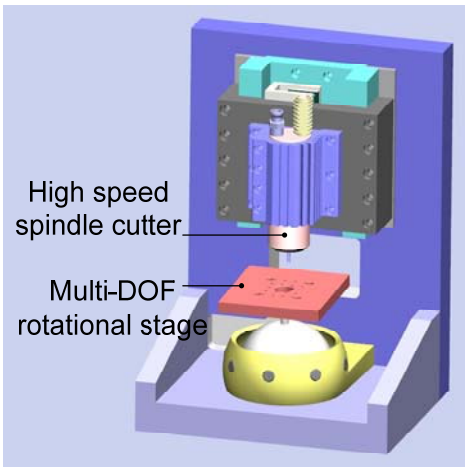

(a) Micro-factory [2]

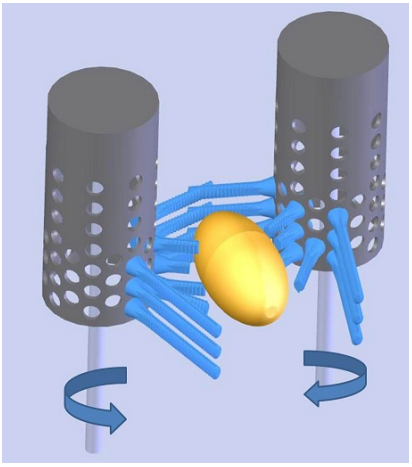

(b) Live-object handling system [3]

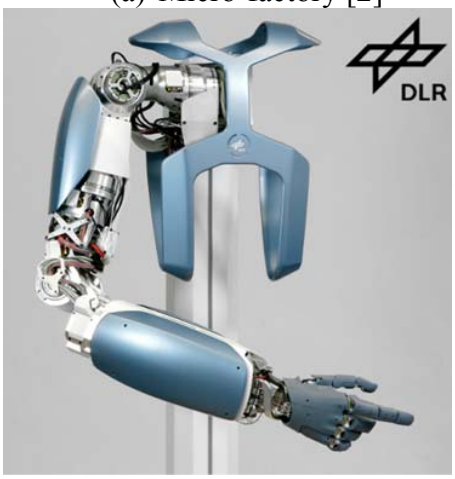

(b) DLR Hand Arm System [4]

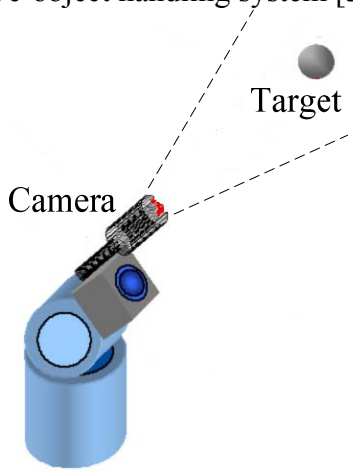

(c) Active vision tracking

Figure 1.1 Applications of multi-DOF actuators

Existing multi-DOF actuators usually achieve multi-DOF motion through serial/parallel connected single-axis motors with external gearing. Driven by the stringent accuracy and tolerance requirements, various forms of parallel mechanisms

with three or more single-axis motors were proposed; for example [5-7]. These multi-DOF mechanisms are generally bulky and lack of dexterity. A number of novel actuators have been developed. Among these are the ball-joint-like spherical motors capable of providing multi-DOF motion in a single joint. The spherical motors can provide continuous multi-DOF motion without external gearing mechanism and thus can eliminate unwanted frictions and singularities in conventional multi-DOF actuators. Permanent magnet spherical motors (PMSMs) with relative large torque-to-inertia ratio have attracted much research attention because they are structurally simple for precision operation with rapid and continuous responses. The tradeoff, however, is the need to develop a real-time feedback control system for precisely controlling the orientation of the spherical motors.

Traditional closed-loop control systems for PMSMs depend on external orientation sensing systems. Firstly, like control systems for most motion systems, the control law is derived using the error between desired and measured position/orientation; secondly, in order to realize the desired torque derived by the control law, the torque characteristic vectors (TCVs) which relate the current inputs of EMs to the applied torque on the rotor are determined with an orientation-dependent model. However, a multi-DOF orientation system is usually computational demanding or requires complicated external structures. Moreover, the dependence of control law and TCV computations on the orientation requires in sequential computations. Therefore, the feedback of orientation sensing in traditional control systems has affected the sampling rate and accuracy.

As the conversion media between the mechanical and electrical energy in electromagnetic motors (including spherical motors), the magnetic field existing in the motors has direct relationship with the orientation and magnetic force/torque and thus can be utilized in developing a control system. Meanwhile, the magnetic field are invariant to environmental factors (such as pressure, light, temperature *etc.*) and can be measured instantaneously with sensors (like hall-effect sensors) of low costs and small footprints. Therefore, a novel control method that directly utilizes the magnetic field measurements as feedback is desired as a solution to the sampling rate and accuracy issues (due to feedback of explicit orientation) in traditional control systems for PMSMs.

1.2 Prior and Related Works

The following review of the prior and related publications is organized in three parts. The first part reviews the development of spherical motors. Next, sensing systems for detecting orientation of multi-DOF motion systems are investigated. The last part summarizes the control methods applied for spherical motors in previous studies.

1.2.1 Spherical Motors

Spherical motors take a number of forms which include induction[8-11], direct current (DC) [12, 13], stepper [14, 15], variable-reluctance (VR) [16, 17], and ultrasonic [18, 19] motors. Many spherical motors are based on the principle of electromagnetism. The earliest form of electromagnetic spherical motor is spherical induction motor, and the concept was first introduced by Williams and Laithwaite [8]. Davey *et al*. [9] then analyzed the magnetic field and torque of this spherical

induction motor. Vachtsevanos and Lee [10] later proposed a three-DOF spherical induction motor for a robotic wrist. Although the induction spherical motor generates torques in three dimensional spaces, it is difficult to apply in practice because of its mechanical complexity and stator winding design. Foggia *et al.* [11] designed an induction type motor capable of rotating around three independent axes; experimental results showed significant noise and a rather long response time of five seconds. There are also spherical motors based on the principle of DC drive developed by Hollis *et al.* [12] and Kaneko *et al.* [13] respectively, which could offer orientation and/or translation motion.

With the wide availability of high-coercive rate-earth permanent magnets (PMs) at low cost, electromagnetic spherical motors with PM poles have been developed for a variety of applications because of their advantages of energy-efficiency and low mechanical wear (brushless motors). The basic concept of a spherical stepper, which has a relatively simple and compact design, was originally proposed by Lee *et al.* [14, 15]. The spherical stepper offered a relatively large range of motion ($\pm 45^{\circ}$) and possesses isotropic properties in motion. Chirikjian *et al.* [20] designed a spherical stepper motor and developed a commutation algorithm for the spherical stepper Lee [21] extended the design concept of a spherical stepper to that of a variable reluctance spherical motor (VRSM) such that high-resolution motion can be achieved with a relatively small number of rotor and stator poles. A spherical wheel motor (SWM) was proposed by Lee and Son in [22, 23], which achieved control of 2-DOF inclination of continuous spinning rotor shaft. Several researchers had proposed spherical motors with different designs targeted for a variety of applications: A

spherical motor that can achieve two or three DOF motion with the spherical rotor entirely made of magnetized rare-earth magnets was developed by Wang *et al.*[24]; Week *et al*. [25] developed a spherical motor with high stiffness and low friction; Yan [26] , Xia [27] and Wang [28] have also recently reported and developed spherical motors in similar concept.

In addition to the electromagnetic spherical motors, ultrasonic spherical motors have also been studied by several researchers. For instance, Shigeki *et al*. [18] proposed a spherical motor that uses ultrasonic vibrations of the rotor to generate torque to cause desired motion. Amano et al. [19] developed a 3-DOF ultrasonic actuator with three sets of piezoelectric elements in the stator. Two bending vibrations perpendicular to each other and a longitudinal vibration can be excited independently with three separate electrical ports. The spherical rotor was revolved on all three axes by the combination of these vibrations. The ultrasonic actuators have the advantages of high resolution and low power consumption, and the disadvantages such as complex fabrication and instability due to the wear of frictional material.

1.2.2 Orientation Sensing Systems

Traditional control systems for spherical motors rely on orientation sensing systems. In [29], orientation measurements of a ball-joint-like motor was achieved by multiple single-axis encoders with an external mechanism to mechanically decouple the motion into three independent directions. The motion-constraining mechanism introduces additional inertia and friction; the former limits the bandwidth of the PMSM while the latter is a primary cause of physical wear and tear. Inclinometers, accelerometers and other inertia/gyroscopic sensors offer an alternative means to

measure the orientation and position through direct attachment to the moving body as it is done in aircrafts and Unmanned Aerial Vehicles (UAVs) [30]. However, the installation of these sensors not only introduces additional inertia and dynamical imbalance to the system but also requires constrictive bridging connections for power and measurement transmission. To overcome these problems, several non-contact orientation sensors such as optical [31] and vision-based [32] sensors have been developed. However, these sensors either require a specially treated surface or have relatively low sampling rate. More recently methods utilizing the magnetic-field measurements of the moving rotor PMs have been reported by several researchers. As compared to its other non-contact counterparts, magnetic sensors do not require "a line of sight" and permit sensing across multiple non-ferromagnetic mediums. In [24], Wang *et al.* derived the 2-DOF rotor orientation in close-form using the analytical results of the magnetic field. In [33], inverse computation of the rotor position was achieved using a nonlinear optimization algorithm to minimize the deviation between measured and modeled magnetic field (using a single dipole analytical model). This approach was relatively slow, high in complexity and requires a good initial guess of the parameters. A similar methodology was adapted in [34] for a decoupled multi-axis translational system. Lee and Son used the distributed multi-pole (DMP) model [22] to characterize the magnetic field of a single PM and designed a magnetic field-based 2-DOF orientation sensor using methodically placed sensors [35]. Lee and Foong [36, 37] developed a field-based method which used an artificial neural network (ANN) as a direct mapping for orientation determination. This method allowed the determination of the 3-DOF orientation directly from measurements of

the existing magnetic field of rotor PMs. Magnetic field offers a stable and accurate solution to orientation estimation in the above-mentioned methods. However, due to the complexities and nonlinearities in the inverse computation in these methods, the sampling rate of the field-based algorithm must be comprised to some degree in order to achieve high accuracy, which adversely affects the performances of the resulting control systems using these sensing systems for feedback.

1.2.3 Control Methods of Spherical Motors

Motivated by the growing requirement of precise operation for multi-DOF manipulation, significant research efforts have been focused on the closed-loop orientation control of spherical motors. Lee *et al.* presented the dynamic of a VR spherical motor in [15] and formulated a reaction-free control strategy based on the principle of magnetic levitation in [16]. They also derived a maximum torque formula and used a loop-up table based nonlinear scheme for online optimization of current inputs. Lee *et al*. [29] developed a robust back-stepping controller to compensate for imperfect modeling and computational approximations. The performance was evaluated experimentally against a classical PD controller. However, the external mechanism for orientation measurement introduced large inertia and friction to the system and restricted the accuracy as well as the bandwidth of the control system. Wang *et al.* [38] used magnetic field sensors to detect the 2-DOF rotor orientation and experimentally investigated a PID controller for closed-loop orientation control in 2-DOF. In [23], Lee and Son proposed a method for decoupling the continuous spinning motion and the inclination of spinning shaft and A control method was presented which incorporated an open-loop controller for spinning motion and a

closed-loop controller for 2-DOF inclination of the spinning shaft. Other than classical PID controllers, modern control methods have also been applied on spherical motors. Xia [39] applied a fuzzy controller and a neural network identifier to identify the uncertainties in a spherical motor and simulation results showed self-adaptive ability and strong robustness. Similar strategy was also proposed by Li [40] on a spherical stepper motor.

Other than the multi-DOF control law, the development of a closed-loop control system also requires a torque model which is used to determine current inputs based on the desired torque derived from the control law. Lee *et al.* [15] developed torque model of a VR spherical motor and the permanence-based torque model was further investigated theoretically by Pei [21] using finite element methods, and experimentally investigated by Roth [29]. In [29], a closed-form torque model was also formulated that used curve-fitting functions to estimate torques based on the relative positions between PMs and EMs and an inverse torque model to find the optimal current input minimizing the total input energy from desired torque was presented. Similar methods were also used in [28] and [41]. Even though the magnetic torque in a spherical motor is dependent on both magnetic fields and orientation, the torque models in the above-mentioned studies were all formulated in terms of orientation due to the complexity and implicit relationship between magnetic fields and torque.

1.3 Problem Description

Figure 1.2(a) and (b) present two typical PMSM designs. As shown in both designs, a PMSM is composed of a rotor (with embedded PMs) and a stator that houses a set of electromagnets (EMs). Both PMs and EMs have their radial magnetization axes passing through the motor center.

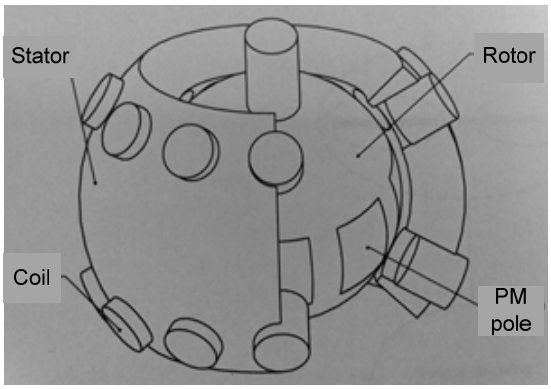

(a) Schematic of a PMSM [42]

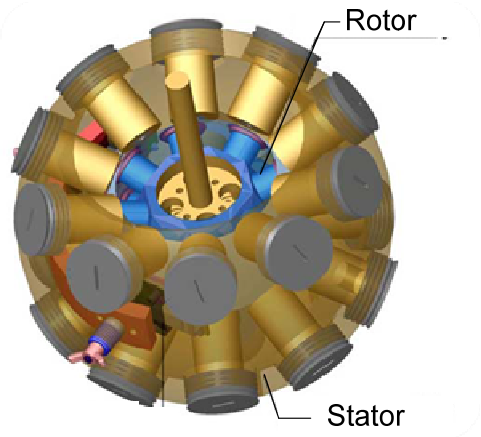

(b) CAD model of a PMSM [22]

Figure 1.2 Conceptual designs of PMSM

Mathematically, a PMSM can be modeled as a combination of two subsystems, rotor dynamics and torque-current relationship. The equation of motion of the PMSM can be derived using Lagrange formulation which is given by

$$\mathbf{[M]\ddot{q} + C(q,\dot{q})\dot{q} + g(q) = T} \tag{1.1}$$

where $\mathbf{q}$ is the orientation; $\mathbf{[M]}$ is the inertia matrix; $\mathbf{C(q,\dot{q})\dot{q}}$ is the centripetal and Coriolis torque vector; $\mathbf{g}$ is the gravitational torque vector; and $\mathbf{T}$ is the total torque on the rotor applied by the EMs on the stator. The detailed derivation of the dynamic model of a PMSM can be found in the appendix (Appendix A).

The torque applied by the j^{th} EM can be characterized by the Lorentz force equation [43]:

$$\mathbf{T}_j = -i_j \int_V \mathbf{r} \times (\mathbf{B} \times d\mathbf{l}) \tag{1.2}$$

where i is the current flowing through the EM and $d\mathbf{l}$ is the unit vector along current direction vector; $\mathbf{r}$ is the vector from the rotation center to the field point; $\mathbf{B}$ is the magnetic flux density at the field point; V is the volume of the coil winding. The torque is proportional to the current input and the coefficient vector referred here as the torque characteristic vector (TCV) can be characterized with:

$$\mathbf{K}_j = -\int_V \mathbf{r} \times (\mathbf{B} \times d\bar{l}) = \mathbf{T}_j / i_j \tag{1.3}$$

The total torque is the summation of the individual torques contributed by each EM, which has the form

$$\mathbf{T} = [\mathbf{K}]\mathbf{u} \tag{1.4a}$$

$$\text{where } [\mathbf{K}] = [\mathbf{K}_1 \quad \ldots \quad \mathbf{K}_j \quad \ldots \quad \mathbf{K}_{Ns}] \tag{1.4b}$$

$$\text{and } \mathbf{u} = [i_1 \quad \ldots \quad i_j \quad \ldots \quad i_{Ns}]^T \tag{1.4c}$$

where N_E is the total number of EMs. Since there are more current inputs than the mechanical DOF, an optimal current vector minimizing the total input energy [29] can be found for a given torque using

$$\mathbf{u} = [\mathbf{K}]^T ([\mathbf{K}][\mathbf{K}]^T)^{-1} \mathbf{T} \tag{1.5}$$

(1.4a) and (1.5) are the forward and inverse torque models of a PMSM.

Figure 1.3 presents the basic components of a PMSM control system. The major challenges involved in an orientation control system for a PMSM are two folds: 1) the control law determines the desired torque (control effort) required to track the desired orientation based on the feedback information, 2) in order to find the optimal current input to realize the desired torque determined by the control law, the TCVs must be

computed in real-time at any orientation and the optimal current input can be found by (1.4c). Traditional control systems rely on orientation feedback for deriving both desired torque and TCVs. For the above-mentioned drawbacks of using explicit orientation feedback in real-time control systems, it is desired that the magnetic field measurements are directly utilized for orientation control.

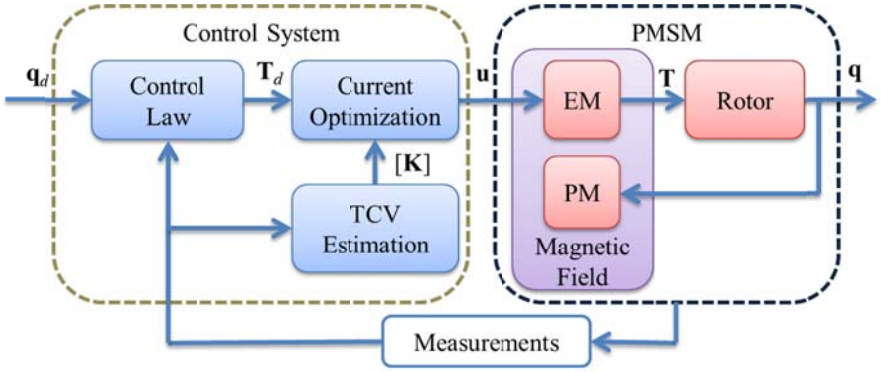

Figure 1.3 Control System for PMSM

It is obvious that the magnetic field of the rotor PMs measured by a sensor installed in the stator is a function of the rotor orientation. For a certain range, the error between the desired and actual orientation can be uniquely characterized by the error between the desired and actual magnetic fields at the sensor point. Since the magnetic field measurements are much easier and faster to acquire than the multi-DOF orientation, it is desired to replace the error of orientation with the error of magnetic fields in the control system.

1.4 Objective and Major Challenges

The objective of this research is to develop a new control method to improve the performances in terms of accuracy and bandwidth of the multi-DOF orientation

control system by directly utilizing magnetic field measurements for feedback in real-time. The major challenges to achieve the objective are summarized as follows.

The domain of a given set of sensors (where the bijective relationship between the orientation and the measured magnetic field exists) must be determined. Also, the relationship between the errors of orientation and magnetic field measurements must be studied such that controller parameters can be properly chosen (since the direction and magnitude of the error in a control law will affect the system stability and performances). The relationship between the rotor orientation and the magnetic field can be explored by investigating their partial derivatives. As shown in later chapters, the bijective domain can be determined by locating the non-zero determinant of the Jacobian matrix (consisting of partial derivatives of magnetic field with respect to orientation).

While the bijective domains for a given set of sensors only correspond to a portion of the entire working space of a PMSM, a multi-sensor network completely covers the workspace with connected bijective domains of multiple sensor sets is introduced so that the DFC system can switch measurements from different sensor sets in the entire working space. The boundaries of the bijective domains are well-defined with respect to magnetic field and are also used as switching criteria among different sensor measurements.

The TCV of an EM depends on both rotor orientation and rotor magnetic field, as can be seen in (1.3). Existing models and methods for estimating TCVs are generally based on rotor orientation or position. Although explicit models to compute the TCVs with scattered magnetic field measurements are difficult to find, a direct mapping characterizing the relationship between TCVs and magnetic field measurements can

be established, which eliminates the explicit orientation for real-time TCV estimation. Meanwhile, models (like ANN) that only requires algebraic computations well suits real-time applications.

There are also practical issues including both hardware and software problems that are important in developing the DFC system for a PMSM. These issues will be elaborated in later chapters.

1.5 Thesis Outline

The remainder of the dissertation is outlined as follows.

Chapter 2 presents the DFC system and compares it with conventional control systems for PMSMs. A 1-DOF example illustrates the process and identifies the key issues in developing a DFC system. New algorithms for realizing the major components of the DFC system are presented and numerically investigated in the context of multi-DOF orientation control.

In Chapter 3, methods for modeling and computing the magnetic fields as well as forces and torques are presented. These methods allowing closed-form solutions have greatly reduced the computational time and have been validated with experimental data. These new methods not only facilitate the development of the DFC system, but also benefit the design and analysis of spherical motors.

Chapter 4 starts with numerical simulation of the static loading capacity of a PMSM. The maximum current inputs are investigated for given specifications. The major components of the DFC system are numerically analyzed on the PMSM and the control responses are simulated. The simulation results offer theoretical basis and insights for the implementation of the DFC system in Chapter 5.

In order to relate the motion trajectories (in terms of rotor orientations) to the corresponding magnetic fields as command inputs of the DFC system, the magnetic fields of the rotor PMs must be precisely calibrated. Chapter 6 presents new algorithms for calibrating and reconstructing the rotor magnetic field in three dimensional space. With these new algorithms, the experimental procedures are greatly simplified while reducing the calibration time and accumulated error. The calibration and reconstruction results with the new algorithms are compared with experimental data and the results show good match.

Based on the numerical investigation of Chapter 4, the DFC system is implemented on a PMSM test-bed in Chapter 6. The control performances of the point-to-point as well as trajectory-tracking motions are experimentally evaluated and the controlled orientation is verified with a commercial gyroscope which operates independently of the control loop. The results show excellent performances in both transient and steady states. The comparison of the sampling rates of the DFC system and the gyroscope acquisition system indicates the capability of the DFC in improving the system bandwidth.

Finally, Chapter 7 summarizes the contributions of this research as well as some future works that can extend and enrich the studies of PMSMs.

CHAPTER 2

DIRECT FIELD-FEEDBACK CONTROL

2.1 Overview

In this chapter the direct field-feedback control (DFC) method for controlling the orientation of PMSMs is presented. The major components of this new method is described and compared to traditional control systems for PMSMs. A 1-DOF example illustrates the process and identifies the key issues in developing a DFC system. Algorithms for realizing the major components of the DFC system for multi-DOF applications are presented and numerical illustrations are provided.

2.2 Control System Description

This subsection begins with comparing the proposed DFC system against with a typical traditional control system for PMSMs. This is followed by a 1-DOF example for illustrating key components of the DFC.

2.2.1 Comparison of Control Systems

Figure 2.1 compares a conventional orientation-dependent control system against the alternative solution based on the DFC system on a PMSM. In Figure 2.1(a), the control law determines the desired torque $\mathbf{T}_d$ in order to track an orientation input $\mathbf{q}_d$ based on the error $\mathbf{e}_q$ between the desired and measured orientations. The TCVs (included in the matrix [**K**]) are computed through an orientation-dependent model. The optimal current vector **u** to realize the desired torque can be found using (1.5). This approach relies on explicit orientation feedback. To assure accuracy, the orientation estimation often requires large amount of computation resulting in long

time delay. Meanwhile, the serial computation (orientation then TCVs) also leads to error accumulation. Both the time delay and accumulated errors have an adverse effect on the overall control performances.

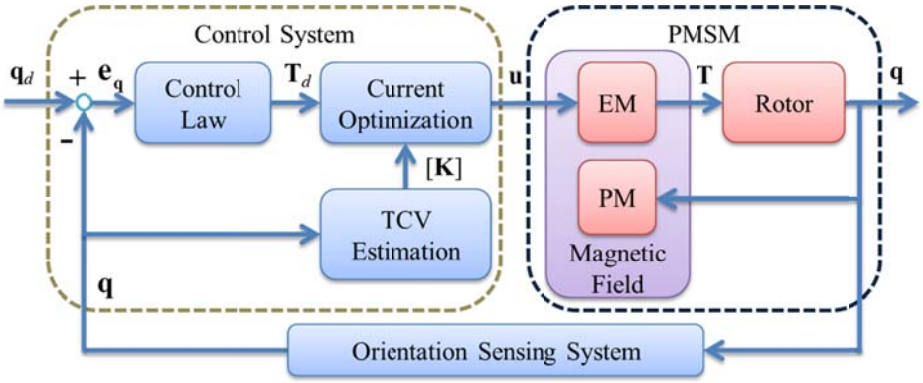

(a) Orientation-feedback control system

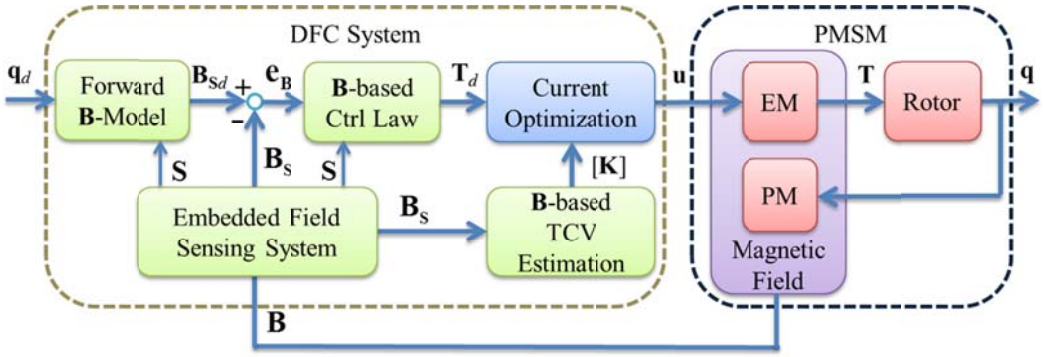

(b) Direct field-feedback control (DFC) system

Figure 2.1 Comparison of control systems

The DFC method is shown in Figure 2.1(b), where the controlled magnetic flux density (MFD) vector $\mathbf{B}_S$ is composed of the MFDs for specified sensors (installed on the stator) at any orientation $\mathbf{q}$. The sensor index vector $\mathbf{S}$ contains the indices of the specified sensors. $\mathbf{B}_{Sd}$ is composed of the MFDs of $\mathbf{S}$ at $\mathbf{q}_d$; and has the same dimension as $\mathbf{B}_S$ (equal to the mechanical DOF of the system). As illustrated in the

diagram, $\mathbf{B}_{Sd}$ can be obtained for any $\mathbf{q}_d$ with the forward **B**-model and **S**. The control law of the DFC system utilizes the error $\mathbf{e}_\mathbf{B}$ between $\mathbf{B}_{Sd}$ and $\mathbf{B}_\mathbf{S}$ to determine $\mathbf{T}_d$. The control parameters are dependent on **S**. Meanwhile, the TCVs can be estimated directly from the MFD measurements, in parallel with the computations involved in the control law. The embedded field sensing system (as shown in Figure 2.1b) determines **S** based on the present orientation and pre-stored information and selects the components of $\mathbf{B}_\mathbf{S}$ from the raw MFD measurements **B**.

With the direct feedback of measured MFD, an explicit orientation feedback is not required in the real-time control system and the computation efficiency is greatly improved in two aspects:

- The acquisition of the MFD measurements requires much less time than that of the orientation measurements.
- Because the control law and TCV estimation can be independently obtained from measured MFD, and $\mathbf{B}_d$ from the forward **B**-model independently of the control loop, the DFC system permits parallel processing of these three components in real-time computation.

As a result, DFC has a potential to dramatically improve the sampling rate and accuracy of the closed-loop PMSM orientation control system.

It is worth emphasizing that since a direct correspondence only exists between the orientation and the MFDs of the rotor PMs, the MFDs of the EMs (when supplied with current inputs) acquired by the magnetic sensors concurrently with the rotor MFDs must be compensated. The MFD compensation of the EM (in the embedded

field sensing system) will be elaborated in Chapter 6 and the MFD (denoted by **B** or **B** with subscripts) in the following discussion specifically refer to the MFDs from rotor PMs.

2.2.2 Illustrative 1-DOF Example

The DFC system is best illustrated with the following example. Figure 2.2 shows a 1-DOF model consisting of a PM and a pair of stationary EMs. The PM is fixed with the rotor free to rotate in the YZ plane. When current flows into the EMs, a torque (perpendicular to the YZ plane) is generated causing the rotor to rotate with an angle θ. The equation of motion is given in (2.1), where the resultant torque applied on the rotor is the summation of the individual torques contributed by each of the EMs as shown in (2.2):

$$J\ddot{\theta} + b\dot{\theta} = T_X \tag{2.1}$$

$$T_X = \begin{bmatrix} k_{X1} & k_{X2} \end{bmatrix} \begin{bmatrix} u_1 & u_2 \end{bmatrix}^T = [\mathbf{K}]\mathbf{u} \tag{2.2}$$

where k_{x1} and k_{x2} are the TCVs (one-dimensional in this case) of EM_1 and EM_2 and u_1 and u_2 are the current inputs of EM_1 and EM_2.

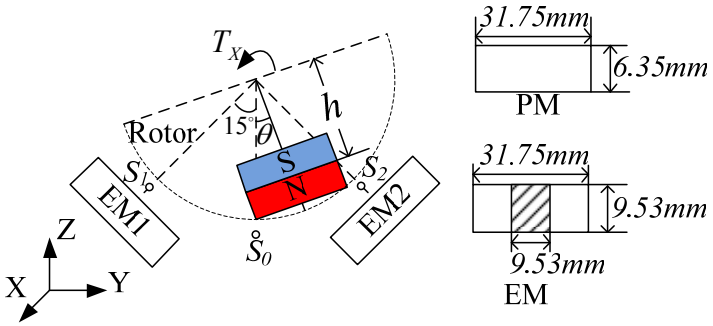

Figure 2.2 1-DOF model

A. Sensor configuration and MFD characteristics

As an illustration, we consider three magnetic sensors (S_0, S_1, S_2 in Figure 2.2) for measuring the MFDs of the rotor PM. Figure 2.3(a, b) show the MFD components at S_0 , S_1, S_2 against θ in normal (B_n, along the radius in YZ plane) and tangential (B_t, tangent to the radius in YZ plane) directions, where the MFDs are computed from the negative gradient of the analytical magnetic potential [43]

$$\mathbf{B}_{\mathrm{PM}} = \frac{\mu_0}{4\pi}\int_V \frac{-(\nabla \bullet \mathbf{M})(\mathbf{R}-\mathbf{R}')}{|\mathbf{R}-\mathbf{R}'|^3}dV + \frac{\mu_0}{4\pi}\int_S \frac{(\mathbf{M}\bullet\mathbf{n})(\mathbf{R}-\mathbf{R}')}{|\mathbf{R}-\mathbf{R}'|^3}dS \qquad (2.3)$$

where $\mathbf{n}$ is the unit surface normal, $\mathbf{R}'(x', y', z')$ and $\mathbf{R}(x, y\ z)$ are the interested and field point; $\mathbf{M}$ is the magnetization of the PM. Figure 2.3(c) shows the normal and tangential MFDs at S_0. As shown in Figure 2.3(c), the entire range can be divided into three domains (Γ_1, Γ_2, Γ_3) and in each domain B_t and θ are bijective (one-to-one and onto). The bijection can be analyzed by the derivative of B_t *w.r.t* θ. As shown in Figure 2.3d), $dB_t/d\theta$ is strictly positive (in Γ_2) or negative (in Γ_1, Γ_3), which implies the monotonic relationship between B_t and θ in each bijective domain.

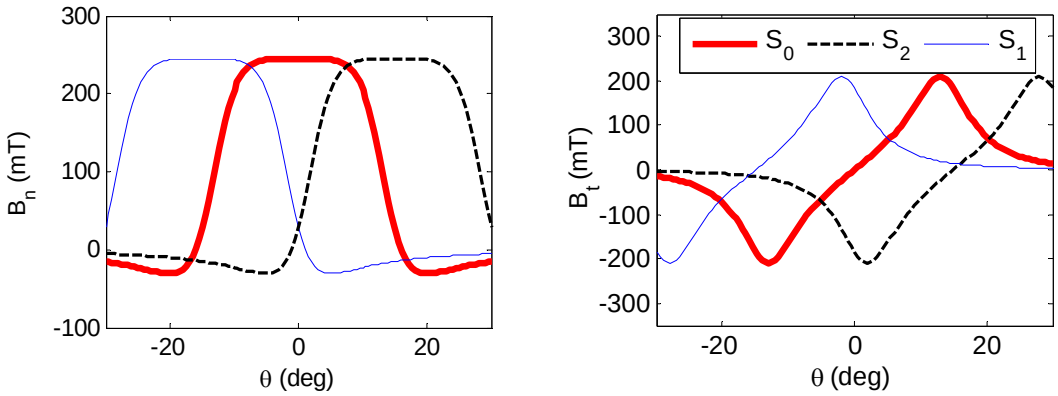

(a) Normal MFD (b) Tangential MFD

Figure 2.3 Illustration of MFD and bijective domains

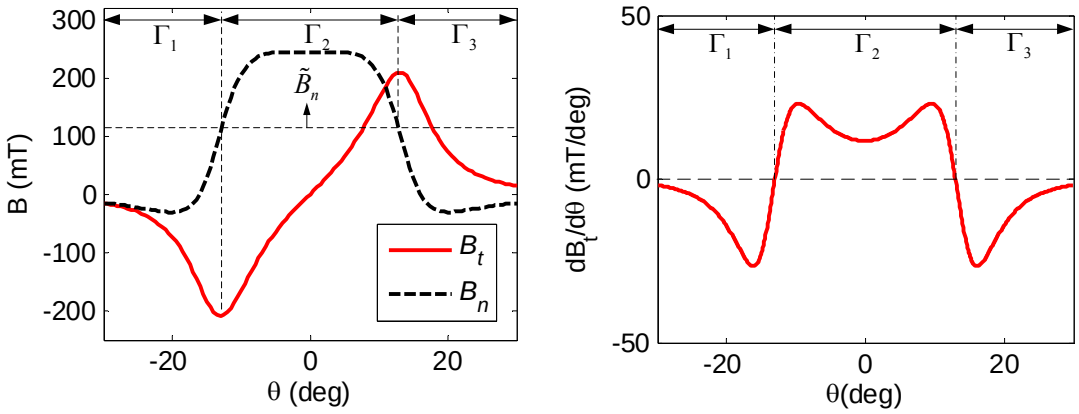

(c) Bijective domains (d) $dB_t/d\theta$

Figure 2.3 (Continued)

B. Control law of DFC

For a specified domain, control law with MFD feedback takes the form:

$$T_{Xd} = k_p e_B + k_d \dot{e}_B \tag{2.4a}$$

where

$$e_B = B_{td} - B_t \tag{2.4b}$$

where B_{td} and B_t are the desired and actual tangential MFDs corresponding to the desired rotational angle θ_d and actual rotational angle θ respectively. In Γ_i (i = 1, 2, 3), e_B is related to the error of the rotational angle e_θ as follows:

$$e_B = B_{td} - B_t = a_i(\theta_d - \theta) = a_i e_\theta \tag{2.5}$$

In (2.5), a_i is the slope of a line segment connecting points (θ, B_t) and (θ_d , B_{td}) on the B_t-curve as shown in Figure 2.3(c) in Γ_i . It can be seen that a_i is not constant and in each domain a_i has the same sign as $dB_t/d\theta$. Substituting (2.5) into (2.4a), the auxiliary control law in terms of e_θ can be obtained:

$$T_{Xd} = k'_p e_\theta + k'_d \dot{e}_\theta \text{ and} \tag{2.6a}$$

where

$$k'_p = a_i k_p \text{ and } k'_d = a_i k_d \tag{2.6b}$$

For the dynamic system (2.1), it can be seen that as long as k_p' and k_d' in the auxiliary control law (2.6) are positive, the system is stable. As the sign of a_i is known (same sign as $dB_t/d\theta$) for a specified domain, the gains in DFC control law (2.4) can be selected such that k_p' and are positive and thus the stability is ensured. As bijection is ensured in each bijective domain, when the controlled variable B_t converges to B_{td}, θ will also converge to θ_d. The signs of a_i are summarized in Table 2.1. Since θ is unavailable for the DFC system, the bijective domains are defined in terms of the MFDs, which are also summarized in Table 2.1.

Table 2.1 Domain characteristics ($\tilde{B}_n = 112mT$)

Γ_1	Γ_2	Γ_3
$a_1<0$	$a_2>0$	$a_3<0$
$B_n < \tilde{B}_n$, $B_t < 0$	$B_n > \tilde{B}_n$	$B_n < \tilde{B}_n$, $B_t > 0$

C. Estimation of TCVs

To realize the desired torque (T_{Xd}) determined by the control law (2.4), the TCVs in (2.2) must be computed for determining an optimal current input vector **u** that minimizes the total input energy:

$$\mathbf{u} = [u_1 \quad u_2]^{\mathrm{T}} = \frac{T_{Xd}}{k_{X1}^2 + k_{X1}^2}[k_{X1} \quad k_{X2}]^{\mathrm{T}} \tag{2.7}$$

The TCVs can be computed using (1.3) as functions of θ. Although there is no explicit model for computing TCVs directly from MFDs, the correspondence between B_t and TCVs can be used with θ as intermediate variable. For each θ, the corresponded TCVs and B_t are graphed in Figure 2.4 (a) and (b) in each bijective

domain (denoted by the solid lines). Note that the TCVs in Γ_3 are symmetric to those in Γ_1. A spline-fit function can be obtained which allows for the estimation of the TCVs directly from MFDs. The TCVs (estimated using the spline-fit function) are compared with numerical results in Figure 2.4(a, b) where the mean absolute error (MAE) for all the sampled points is 2.4×10^{-6} Nm.

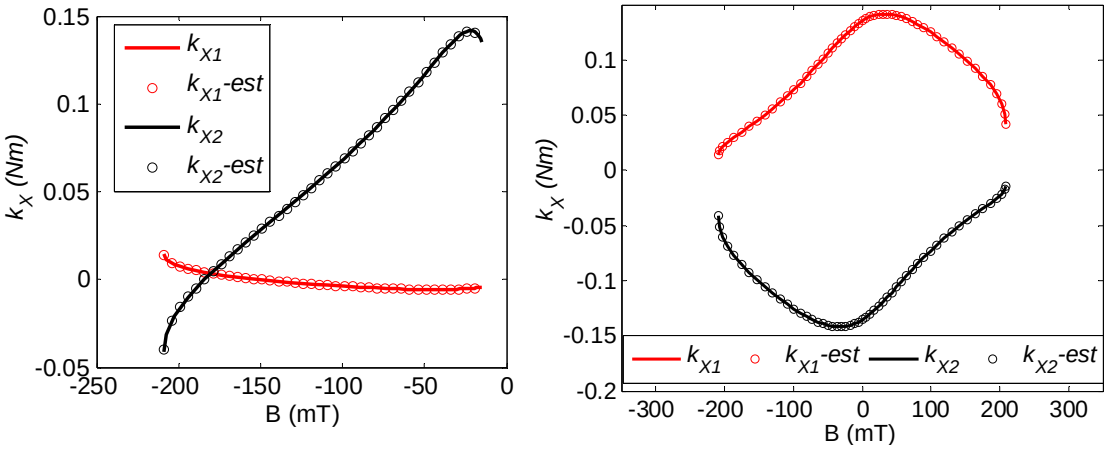

(a) Domain Γ_1 and Γ_3 (b) Domain Γ_2

Figure 2.4 Illustration of TCVs against MFDs

D. Closed-loop control simulation

The response of the DFC system (with parameters given in Table 2.2) was simulated where θ_d followed a trajectory given by:

$$\theta_d = \theta_0 \sin(\pi t / 2), \text{where } \theta_0 = 14^\circ \tag{2.8}$$

Figure 2.5 shows a portion of B_t from each sensor and each of which corresponds to a bijective domain (Γ_2 of each sensor). As the DFC method can be applied in any bijective domain, the system can operate in the entire rotational range by switching feedback B_t from different sensor readings. The switching criteria defined in terms of the normal MFDs are shown in Figure 2.5, where the selected bijective domains of all

sensors have overlaps to avoid singularity at the switching points. The signs of a_i of each sensor are the same as shown in Table 2.1. For each θ_d, the desired MFDs for a selected sensor can be obtained using curve-fit functions acquired from the analytical results as shown in Figure 2.3(b). Figure 2.6(a, b) show the MFD response along with the sensor switching sequence and the corresponding time response of θ. As *a's* are positive for all sensors, the PD gains of the DFC as shown in Table 2.2 are set to be positive so that the PD gains of the auxiliary control law (2.6) are positive assuring the stability of the system. It can be seen that as B_t follows B_{td}, the rotational angle θ also tracks the desired trajectory closely. In the simulation, the TCVs are estimated directly from the MFDs using the above-mentioned spline-fit function and the optimal current inputs computed using (2.7) are shown in Figure 2.6(c). Due to the discrepancies where the estimated and actual TCVs as well as the resultant current inputs computed based on the estimated TCVs, the desired torque determined by the control law (2.4) and the resultant torque applied on the rotor are different. The results are compared in Figure 2.6(d). As the differences in torque can be compensated in the closed-loop control system, it can be seen that the effects of discrepancies due to the TCV estimation error are almost trivial.

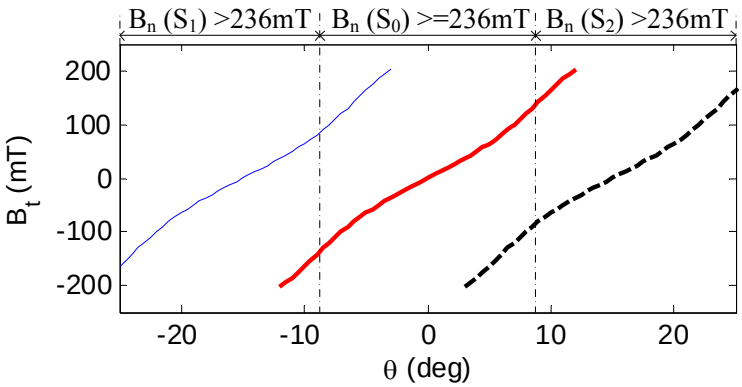

Figure 2.5 Sensor domain switching criteria

Table 2.2 Simulation parameters

J	b	$m*h$	k_p	k_d
$0.1\tau_0$	$0.1\tau_0$	$0.5\ \tau_0$	$3\ \tau_0$	$0.2\ \tau_0$

τ_0 is a non-dimensional constant, and $\tau_0 = 0.2$.

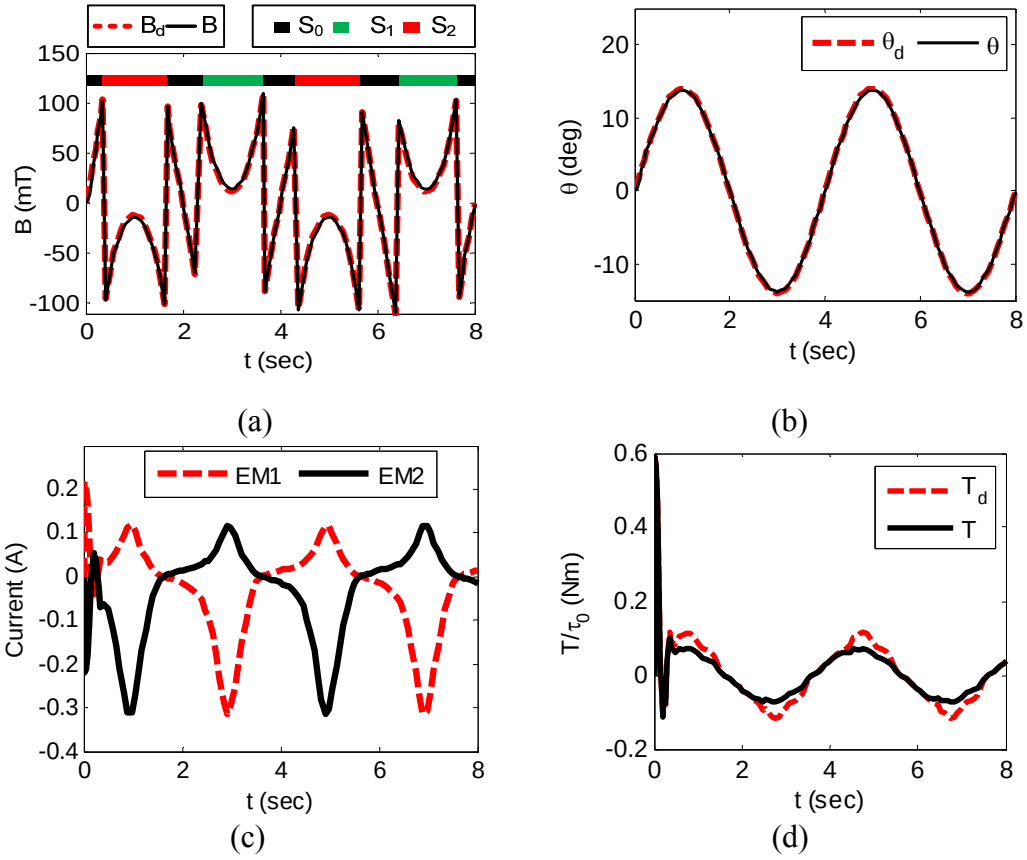

Figure 2.6 Simulation responses

2.3 DFC For Multi-DOF Orientation Control

Based on the above illustration, the key issues as well as the solutions in developing a DFC system for controlling the orientation of multi-DOF motion are presented.

2.3.1 Determination of Bijective Domain

As DFC system is to drive the error between $\mathbf{B_S}$ and $\mathbf{B_{S}}_d$ (as shown in Figure 2.1a) to zero, the bijective domains (in which the MFDs and orientations are bijective) must be found for feedback sensing. This will ensure that when the control system drives $\mathbf{B_S}$ to $\mathbf{B_{S}}_d$, the rotor will reach to the desired orientation $\mathbf{q}_d$ which uniquely corresponds to $\mathbf{B_{S}}_d$.

The bijection between the magnetic fields and the position/orientation of motions systems has been widely studied [37, 44]. Due to the complexities of magnetic fields and the fact that it is more important to uniquely determine the position/orientation from magnetic field measurements for many sensing applications, methods that can characterize the bijective domains analytically have not been found. Bijective relationship is usually reduced to subjective relationship in previous studies about position/orientation sensing applications. As the DFC can be only applied in bijective domains, there is a need for a method for finding the bijective domain analytically.

Without loss of generality, $\boldsymbol{f}$ is defined as a function that matches $\mathbf{q}$ to $\mathbf{B_S}$:

$$\mathbf{B_S} = \boldsymbol{f}(\mathbf{q}) \tag{2.9}$$

According to the implicit function theorem [45], for any $\mathbf{q}, \mathbf{B_S} \in \mathbb{R}^n$, $\boldsymbol{f}$ is bijective (and invertible) in a neighborhood around $\mathbf{q}_0$ if

$$J = \det([\mathbf{J}])\big|_{\mathbf{q}=\mathbf{q}_0} \neq 0 \tag{2.10}$$

In (2.10), the Jacobian matrix $\mathbf{J}$ has the form

$$\mathbf{J} = \left[\partial B_i \big/ \partial q_j \right], \text{ where } i, j = 1,2,\ldots,N \tag{2.11}$$

where B_i and q_j are the i^{th} and j^{th} components in $\mathbf{B_S}$ and $\mathbf{q}$ respectively; N equals to the dimension of $\mathbf{B_S}$ (or $\mathbf{q}$).

As explicit forms for $\boldsymbol{f}$ and $\mathbf{J}$ usually cannot be found for many circumstances, the bijective domain can be determined numerically. The bijective condition (2.10) requires that the Jacobian matrix is nonsingular. For numerical implementation, two alternative conditions which use the determinant and condition number to eliminate singular Jacobian matrix can be used in order to avoid the incorrect determination due to the errors of numerical approximations:

A: $$\Gamma = \{\mathbf{q} \mid |J| > \varepsilon\} \tag{2.12}$$

B: $$\Gamma = \{\mathbf{q} \mid \kappa(\mathbf{J}) < \chi\} \text{ , where } \kappa(\mathbf{J}) = \frac{\sigma_{\max}}{\sigma_{\min}} \tag{2. 13a, b}$$

In (2.12) and (2. 13), ε and χ are positive constants; $\kappa(\mathbf{J})$, $\sigma_{\max}$ and $\sigma_{\min}$ are the condition number, the maximum and minimum singular values of the Jacobian

Numerical Illustration

In order to illustrate the method for determining the bijective domain, the model presented in Figure 2.2 is extended into 2-DOF.

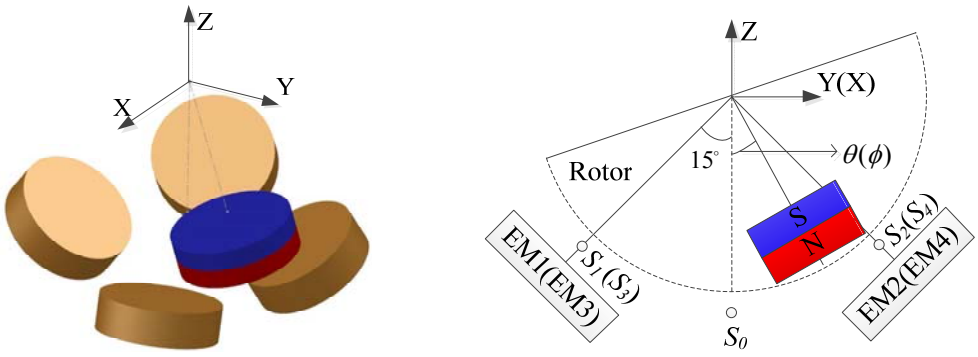

(a) Isometric view (b) Plane view

Figure 2.7 2-DOF model for numerical illustration

As shown in Figure 2.7, EMs 1 and 2 (3 and 4) are located in YZ (XZ) plane. At the center of each EM, a magnetic sensor for measuring the normal MFD (B_n) is mounted; and an additional sensor is placed in the middle. All sensors are at the same distance from the rotation center. For simplicity, the subscript in B_n is omitted in the following discussion. The rotor consisting of one PM can move in 2-DOF with θ, ϕ representing the rotation angles about X and Y axes respectively. The goal here is to find the bijective domains for the sensors.

The MFD readings of the sensors are simulated using (2.3) for each orientation in the range $-15^\circ \le (\theta, \phi) \le 15^\circ$. The radial components of the MFD from S_0, S_1 and S_3 are shown in Figure 2.8. Due to symmetry, the MFDs of S_2 and S_4 are similar and not graphed.

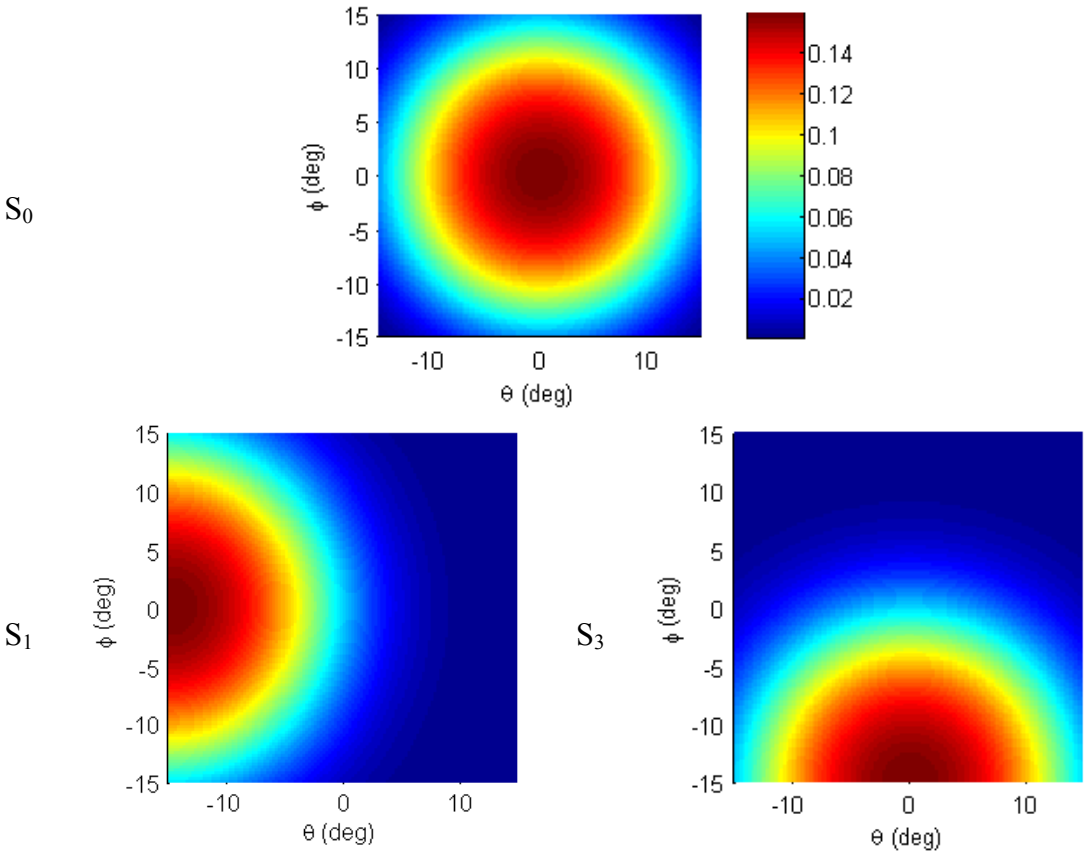

Figure 2.8 B_n from S_0, S_1, S_3 (unit: T)

Since the rotor has 2-DOF, two sensor measurements (from a total of five sensors) are required at any orientation to establish the bijection. In order to visualize the relationship between the MFD and the orientation, Figure 2.9 displays θ and ϕ (reversely) in terms of B_0 (B_n of S_0) and B_1 (B_n of S_1). It can be seen that the MFD vector (B_0, B_1) and (θ, ϕ) are not bijective in the entire range because there are more than one (θ, ϕ) corresponding to each (B_0, B_1).

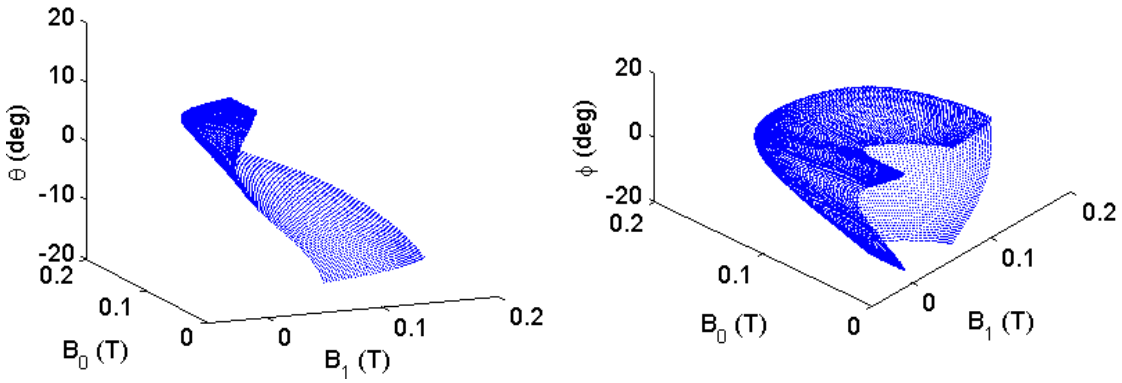

Figure 2.9 θ, ϕ *w.r.t* MFD

Here, the Jacobian matrix for any MFD vector (B_a, B_b) is

$$J_{a,b} = \begin{bmatrix} \partial B_a / \partial \theta & \partial B_a / \partial \phi \\ \partial B_b / \partial \theta & \partial B_b / \partial \phi \end{bmatrix} \tag{2.14}$$

Figure 2.10 shows the variations of the Jacobians of (B_0, B_1) and (B_3, B_4) *w.r.t* θ and ϕ, where the values are normalized with

$$\bar{J}_{a,b} = mean\left|J_{a,b}\right| \tag{2.15}$$

The dotted lines in Figure 2.10 represent the contours where $J_{a,b} = \overline{J}_{a,b}$, which implies that the regions enclosed by the contours are the bijective domains for (S_0, S_1) and (S_3, S_4) respectively according to (2.12), where $\varepsilon = \overline{J}_{a,b}$.

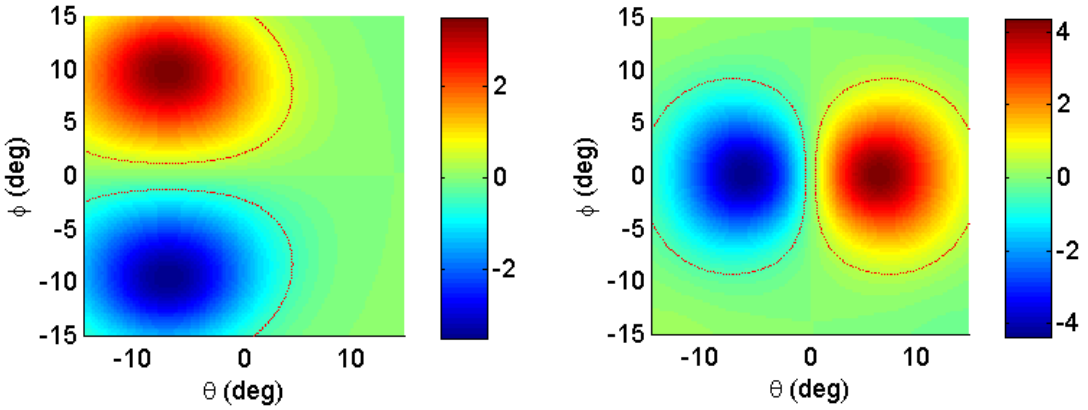

(a) $J_{0,1} / \overline{J}_{0,1}$ (b) $J_{3,4} / \overline{J}_{3,4}$

Figure 2.10 Jacobians of (S_0, S_1) and (S_3, S_4)

2.3.2 Control Law of DFC and Control Parameter Determination

The PD control law of the DFC with MFD feedback takes the form:

$$\mathbf{T}_d = \mathbf{K}_P \mathbf{e}_B + \mathbf{K}_D \dot{\mathbf{e}}_B \tag{2.16a}$$

where

$$\mathbf{e_B} = \mathbf{B}_{\mathbf{S}d} - \mathbf{B_S} \tag{2.16b}$$

In a bijective domain, the orientation error can be characterized in terms of the MFD error $\mathbf{e_q}$ which has the form:

$$\mathbf{e_B} = \mathbf{A}\mathbf{e_q} \tag{2.17a}$$

where

$$\mathbf{A} = \left[a_{ij} \right],\ i, j = 1,2,\ldots,n \tag{2.17b}$$

and

$$\mathbf{e_q} = \mathbf{q}_d - \mathbf{q} \tag{2.17c}$$

Although the elements of **A** are not constants, a_{ij} is bounded by $\partial B_i / \partial q_j$ in each bijective domain [46]. The auxiliary control law obtained by substituting (2.17a) into (2.16a) is

$$\mathbf{T}_d = \mathbf{K}'_P \mathbf{e}_\mathbf{q} + \mathbf{K}'_D \dot{\mathbf{e}}_\mathbf{q} \tag{2.18a}$$

where $$\mathbf{K}'_P = \mathbf{K}_P \mathbf{A},\ \mathbf{K}'_D = \mathbf{K}_D \mathbf{A} \tag{2.18b,c}$$

For the rotor dynamics as given in (1.1), the system is stable and the states will converge to the desired orientation as long as $\mathbf{K}'_P$ and $\mathbf{K}'_D$ in the auxiliary control law (2.18a) are positive definite (proof can be found in Appendix B). As the ranges of the values of *a*'s in **A** are known (bounded by $\partial B_i / \partial q_j$), the elements in $\mathbf{K}_P$ can be selected such that $\mathbf{K}'_P$ is positive-definite. Similarly, the $\mathbf{K}_D$ can be determined in the same way to assure the stability of the system.

Numerical Illustration

The 2-DOF as shown in Figure 2.7 is used for illustration. MFDs from (S_0, S_1) are used to illustrate the process of deriving the DFC control law in a bijective domain.

The errors and the **A** matrix in (2.16), (2.17) and (2.18) are:

$$\mathbf{e}_\mathbf{B} = \begin{bmatrix} e_{B_1} & e_{B_2} \end{bmatrix}^T,\ \mathbf{e}_\mathbf{q} = \begin{bmatrix} e_\theta & e_\phi \end{bmatrix}^T,\ \mathbf{A} = \begin{bmatrix} a_{01} & a_{02} \\ a_{11} & a_{12} \end{bmatrix} \tag{2.19a,b,c}$$

where a_{11}, a_{12}, a_{21}, a_{22} are bounded by $\partial B_0 / \partial \theta, \partial B_0 / \partial \phi, \partial B_1 / \partial \theta, \partial B_1 / \partial \phi$ respectively. Figure 2.11 shows the variations of the four partial derivatives and the maximum and minimum values within the bijective domain (with the contours representing the boundaries). Due to symmetry, the results are only shown for $0^\circ \le \phi \le 15^\circ$. The gain matrices of the auxiliary control law are:

$$\mathbf{K}'_P = \mathbf{K}_P\mathbf{A} = \begin{bmatrix} k_{p1}a_{01} & k_{p1}a_{02} \\ k_{p2}a_{11} & k_{p2}a_{12} \end{bmatrix} \tag{2.20a}$$

$$\mathbf{K}'_D = \mathbf{K}_D\mathbf{A} = \begin{bmatrix} k_{d1}a_{01} & k_{d1}a_{02} \\ k_{d2}a_{11} & k_{d2}a_{12} \end{bmatrix} \tag{2.20b}$$

where $$\mathbf{K}_P = \begin{bmatrix} k_{p1} & 0 \\ 0 & k_{p2} \end{bmatrix}, \mathbf{K}_D\mathbf{A} = \begin{bmatrix} k_{d1} & 0 \\ 0 & k_{d2} \end{bmatrix} \tag{2.20c,d}$$

For any $\mathbf{x} \neq 0$,

$$\mathbf{x}^T(\mathbf{K}_P\mathbf{A})\mathbf{x} = k_{p1}a_{01}\left[x_1 + \left(\frac{k_{p2}a_{11} + k_{p1}a_{02}}{2k_{p1}a_{01}}\right)x_2\right]^2 + \left[k_{p2}a_{12} - \frac{\left(k_{p2}a_{11} + k_{p1}a_{02}\right)^2}{4k_{p1}a_{01}}\right]x_2^2 > 0 \tag{2.21}$$

if

$$k_{p1}a_{01} > 0 \tag{2.22a}$$

$$\text{and } k_{p2}a_{12} - \frac{\left(k_{p2}a_{11} + k_{p1}a_{02}\right)^2}{4k_{p1}a_{01}} > 0 \tag{2.22b}$$

Therefore, $\mathbf{K}'_P$ is positive definite as long as (2.22) is satisfied. Similarly, the elements in $\mathbf{K}_D$ can be also selected so that $\mathbf{K}'_D$ is positive definite and the system stability can be assured.

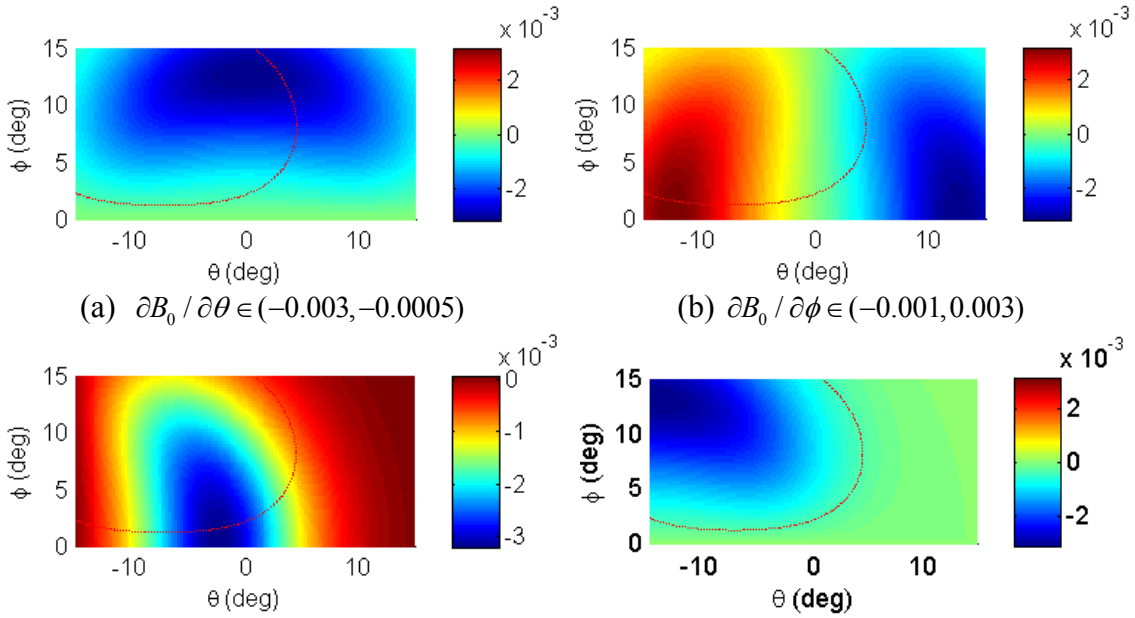

(a) $\partial B_0 / \partial\theta \in (-0.003, -0.0005)$ (b) $\partial B_0 / \partial\phi \in (-0.001, 0.003)$

(c) $\partial B_1 / \partial\theta \in (-0.0001, -0.003)$ (d) $\partial B_1 / \partial\phi \in (-0.003, -0.0005)$

Figure 2.11 Illustration of partial derivatives in bijective domain of (S_0, S_1)

2.3.3 Extension of DFC with Multi-sensor Approach

As the DFC method can be applied within any bijective domain, it can be extended to a larger region formed by connecting bijective domains of different sensor sets, where controlled MFD vector $\mathbf{B_S}$ switches measurements from different sensors. The neighboring bijective domains that form the connected domain must have overlapped regions so that there is no singularity when the switching happens.

Since the bijective domains found using (2.12) or (2. 13a, b) are in orientation space, the domain boundaries must be converted into MFD space since the orientation information is not available in real-time. This enables the control system to identify the bijective domains solely from measured MFDs. For circumstances where the boundaries of the bijective domains are difficult to define explicitly in MFD space, alternative domains (Ω's) satisfying the following conditions can be found:

- Ω must be completely enclosed by a bijective domain so that the bijective relationships still hold in Ω.
- The Ω boundaries can be defined explicitly in terms of MFDs and be used as switching criteria when $\mathbf{B_S}$ switches from different MFD measurements.

Numerical Illustration

In the 2-DOF model as shown in Figure 2.7, the bijective domains of all MFD vectors were found using (2.12) and Figure 2.12 depicts the bijective domains of four MFD vectors. It can be seen that the connected bijective domains completely cover the entire range of motion. Moreover, the overlaps of neighboring domains ensures that there are no singularities on the boundaries where $\mathbf{B_S}$ switches from different MFD vectors.

As it is difficult to find explicit forms for describing the boundaries of the bijective domains as shown in Figure 2.12, alternative MFD-defined domains can be found. Figure 2.13 shows the regions (colored areas) defined by MFDs where the contours (denoted by the dashed lines) represent the boundaries of the bijective domain of (S_0, S_1) and (S_3, S_4). Due to symmetry, the results are graphed in half of the range (for $0^\circ \le \phi \le 15^\circ$). It can be seen that each MFD-defined region is completely enclosed by one bijective domain. Therefore, DFC can be applied in these MFD-defined regions.

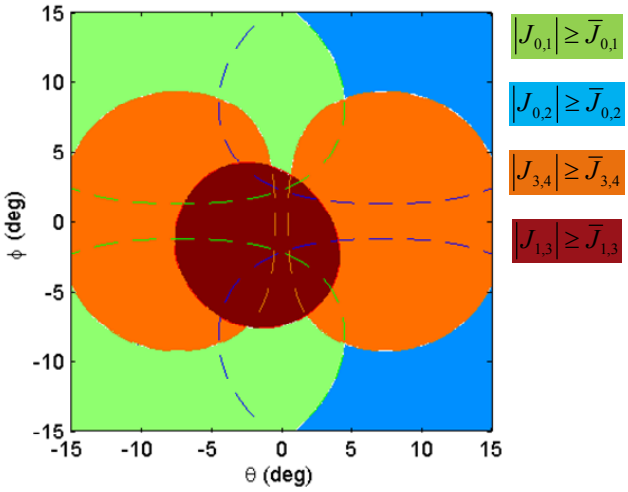

Figure 2.12 Bijective domains of sensor sets

($\bar{J}_{0,1} = 2.8\times10^{-6}, \bar{J}_{0,2} = 2.8\times10^{-6}, \bar{J}_{3,4} = 9.5\times10^{-7}, \bar{J}_{1,3} = 1.8\times10^{-6}$)

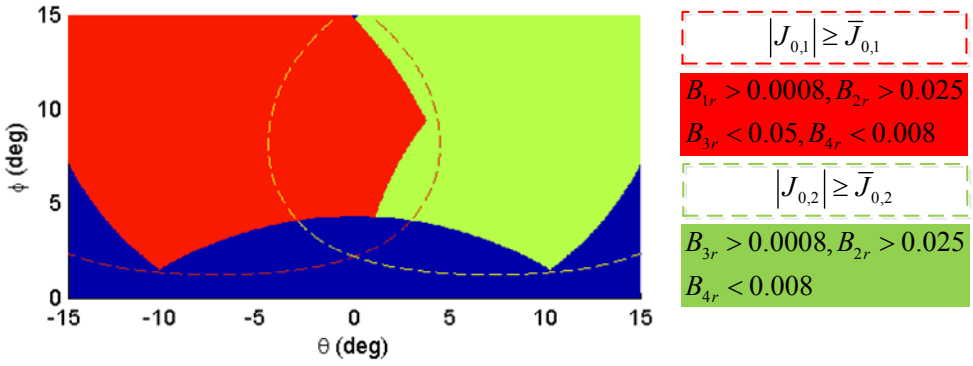

Figure 2.13 Domains defined in orientation and MFD spaces

2.3.4 Field-Based TCV Estimation

Once the desired torque is determined by the control law, a direct mapping that allows estimation of TCVs from the MFDs is derived using an artificial neural network (ANN) without the need of explicit orientation information in the DFC system. As shown in Figure 2.14, the network parameters can be obtained through the Levenberg-Marquardt supervised back propagation training algorithm.

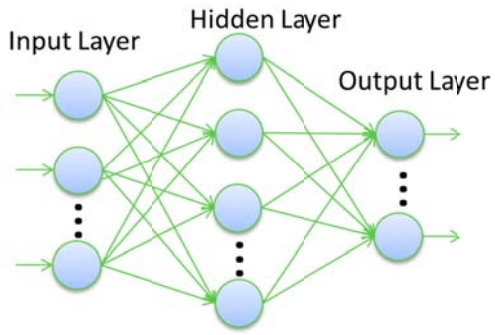

Figure 2.14 ANN structure

Numerical Illustration

In the 2-DOF model (Figure 2.7), the TCV of EM_1 ($\mathbf{K}_1 = [k_{1X}, k_{1Y}, k_{1Z}]$) computed using (1.3) are shown in Figure 2.15 (a-c) as functions of θ and ϕ. Meanwhile, the MFDs of the rotor PM for each orientation can be computed using (2.3) at each sensor, where MFDs from S_0, S_1, S_3 are shown in Figure 2.8. For each (θ, ϕ), the corresponding MFDs and TCV are paired and an ANN (with 1 hidden layer and 10 nodes) was trained with a total of 14641 sample pairs. The inputs, outputs as well as the ANN parameters are shown in Figure 2.16. The estimated results are compared

with the analytical results and the errors are shown in Figure 2.15(d-f) and the maximum errors for each component are less than 5%.

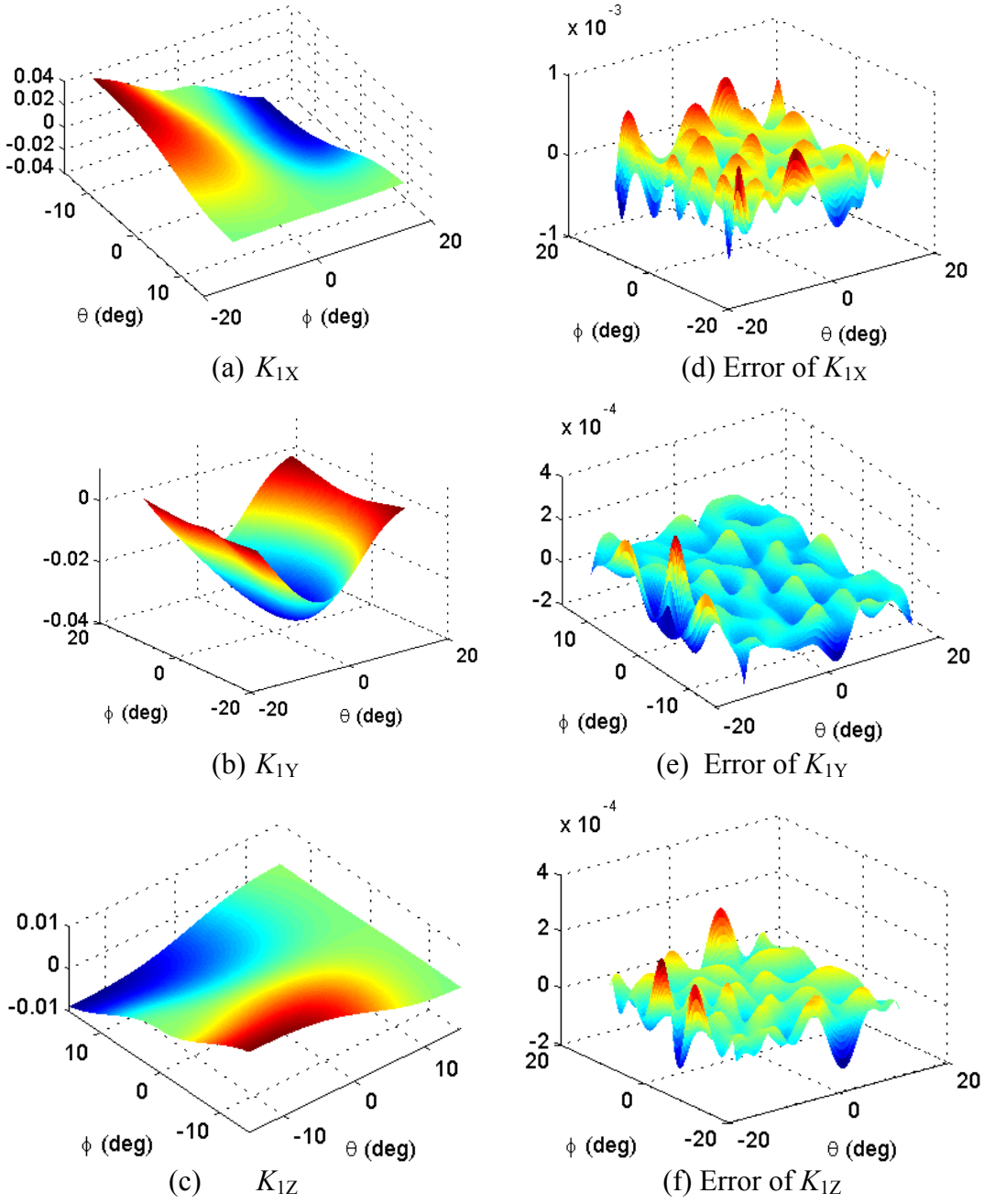

(a) K_{1X} (d) Error of K_{1X}

(b) K_{1Y} (e) Error of K_{1Y}

(c) K_{1Z} (f) Error of K_{1Z}

Figure 2.15 TCVs and estimation errors with ANN

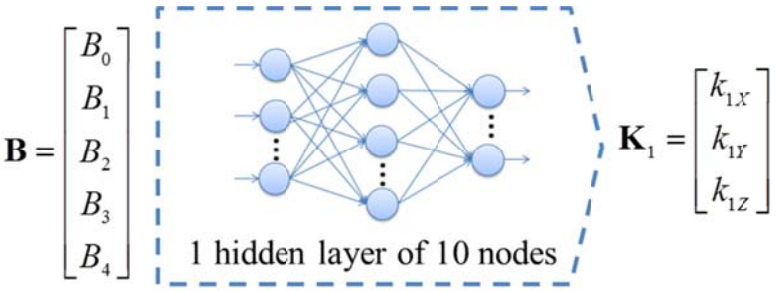

Figure 2.16 ANN simulation parameters

2.3.5 Transition of Control Law between Neighboring Bijective Domains

When the controlled MFD vector switches from different sensor measurements, the desired torque determined by the control law is subject to an abrupt change. It is important that the output of the control law to certain extent retains continuity when the switch happens. Without loss of generality, a PID control law takes the form:

$$\mathbf{T}_d = \mathbf{T}_P + \mathbf{T}_D + \mathbf{T}_I \tag{2.23a}$$

where $$\mathbf{T}_P = \mathbf{K}_P\mathbf{e},\ \mathbf{T}_D = \mathbf{K}_D\dot{\mathbf{e}},\ \mathbf{T}_I = \mathbf{K}_I\int \mathbf{e}dt \tag{2.23b,c,d}$$

where $\mathbf{K}_P$, $\mathbf{K}_D$ and $\mathbf{K}_I$ are the gain matrices; and $\mathbf{e}$ is the error of any physical states. While the first two terms in (2.23a) only depend on present states, the integral term depends on both the present states and the history of the past states. Therefore, if the integral term is necessary for the target dynamic system, the integral torque must be accumulated from the beginning. As the control parameters must be adapted when the controlled MFD vector switches from different sensor measurements, the integral term of (2.23a) for the DFC system can be updated using:

$$\mathbf{T}_I = \mathbf{K}_{(I,1)}\int_{t_0}^{t_1} \mathbf{e}_{\mathbf{B}_1} dt + \ldots + \mathbf{K}_{(I,i)}\int_{t_{i-1}}^{t_i} \mathbf{e}_{\mathbf{B}_i} dt + \ldots \tag{2.24}$$

where $\mathbf{e}_{\mathbf{B}_i}$ is the error of the i^{th} controlled MFD vector used in the switching history of the DFC; $\mathbf{K}_{(1,i)}$ is the corresponding integral gain matrix; and (t_{i-1}, t_i) is the time interval that the i^{th} controlled MFD vector is used as feedback in the DFC system.

2.4 Conclusion

We have presented a new control method which utilizes the magnetic field measurements for direct feedback. The major components of the DFC system for multi-DOF motion were presented and illustrated with numerical examples. This method eliminates the explicit orientation information in real-time control and allows for parallel processing of the major components in real-time control loop.

CHAPTER 3

MAGNETIC FIELD AND FORCE/TORQUE MODEL

3.1 Overview

The design and analysis of a PMSM as well as the development of its control and sensing systems requires large amount of computations on magnetic fields as well as forces/torques. Conventional methods for analyzing magnetic fields and forces/torques involve surface or volume integrals and thus it takes enormous computational time during design and analysis process. The interest to develop alternative techniques for magnetic field and force/torque analysis has led to the distributed multi-pole (DMP) method [22] that computes the 3D magnetic field of a PM in closed form. Using the DMP method, the effects of PM geometrical parameters on the torque performance of a spherical wheel motor (SWM) [47] were investigated. A practical method to further lower the time needed to compute the Lorentz force is to reduce the volume integral to a surface integral; for this, a method to derive an equivalent single layer (ESL) model to approximate the magnetic field of a multi-layer (ML) voice coil was proposed in [35]. While the ESL model is time-efficient for calculating Lorentz forces, the modeling error however increases with coil thickness, particularly within the core. For applications where compact coil designs play an important role to achieve high torque-to-volume ratios, a more accurate yet efficient analytical solution for predicting the magnetic field and force of an EM is desired.

We offer here an improved method to derive an equivalent permanent magnet (ePM) such that the magnetic field of the original multilayer EM can be characterized by a distributed set of multi-poles (DMP) model [48]. This ePM method complements the procedure discussed in [22] where focuses have been on the modeling of PMs to analyze their effects on the forward torque model.

3.2 Distributed Multi-Pole Model for EMs

The process of modeling a multilayer EM as an ePM involves finding an equivalent magnetization **M** in terms of the current density **J** and geometry of the EM. The magnetic flux density created at $\mathbf{R}'(x', y', z')$ to the field point $\mathbf{R}(x, y\ z)$ is given by the Biot-Savart law:

$$\mathbf{B}_{\mathrm{EM}} = \frac{\mu_0}{4\pi}\int_V \frac{\mathbf{J}\times(\mathbf{R}-\mathbf{R}')}{|\mathbf{R}-\mathbf{R}'|^3}dV \tag{3.1}$$

where μ_o is the free space permeability. For a PM, the magnetic flux density can be calculated from the negative gradient of the analytical magnetic potential [43]:

$$\mathbf{B}_{\mathrm{PM}} = \frac{\mu_0}{4\pi}\int_V \frac{-(\nabla\bullet\mathbf{M})(\mathbf{R}-\mathbf{R}')}{|\mathbf{R}-\mathbf{R}'|^3}dV + \frac{\mu_0}{4\pi}\int_S \frac{(\mathbf{M}\bullet\mathbf{n})(\mathbf{R}-\mathbf{R}')}{|\mathbf{R}-\mathbf{R}'|^3}dS \tag{3.2}$$

where **n** is the unit surface normal. Unlike (3.1), the calculation of $\mathbf{B}_{\mathrm{PM}}$ does not need the cross product of **J** and $\mathbf{R}-\mathbf{R}'$ vectors. Equations (3.1) and (3.2) provide the basis for deriving an ePM for the multilayer EM. The interest here is to seek the field solution outside the physical region of the electromagnet, particularly near its boundary along the magnetization axis. The procedure is best illustrated through an example.

3.2.1 Cylindrical EM

Cylindrical PMs and EMs are commonly used in motion systems. Some analytical

and experimental results are also available for model validation. They are used here for clarity to illustrate the DMP modeling procedure. Figure 3.1(a) and (b) show the geometry of the cylindrical EM and its corresponding ePM (with the same l and a_o). The current density of the EM is given by (3.3):

$$\mathbf{J} = J(r)\mathbf{e}_0 \text{ where } \begin{cases} J(r) = 0, 0 \le r < a_i \\ J(r) = J, a_i \le r < a_o \end{cases} \tag{3.3}$$

and a_i and a_o are the inner and outer EM radii.

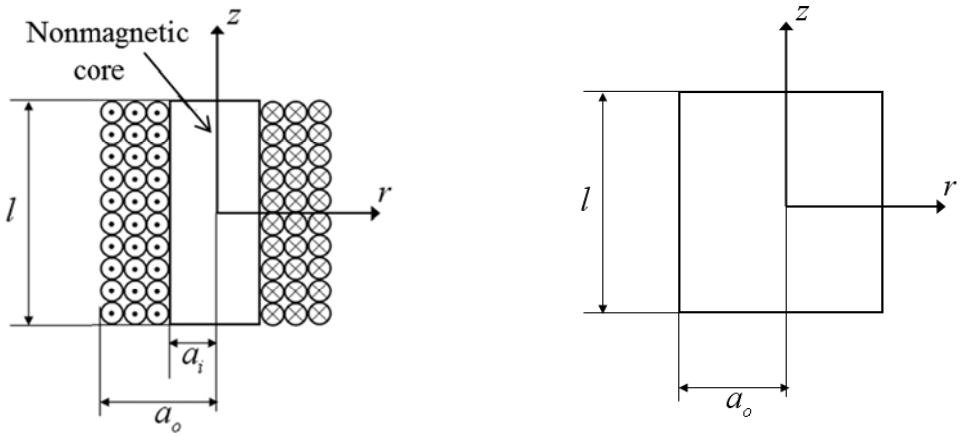

(a) Multilayer EM (b) ePM

Figure 3.1 Multilayer EM and Equivalent PM

From (3.1), the z-component of the EM flux density can be calculated:

$$\frac{B_{\mathrm{EMz}}(X,Y,Z)}{\mu_0 J(l/2)} = \frac{1}{4\pi}\int_{a_r}^{1}\int_{-1}^{1}\int_{0}^{2\pi} \frac{\rho(\rho - X\cos\theta - Y\sin\theta)\,d\theta\,dZ'\,d\rho}{\left[(X-\rho\cos\theta)^2 + (Y-\rho\sin\theta)^2 + L^2(Z-Z')^2\right]^{3/2}} \tag{3.4}$$

where $(X,Y,Z) = (x/a_o, y/a_o, 2z/l)$; $\rho = r/a_o$; $a_r = a_i/a_o$; and $L = l/(2a_o)$. A general closed-form solution to (3.4) is not available. To investigate the effect of the aspect ratios (a_r and L) on B_{EMz} for actuator design, we numerically integrate (3.4) at $z = l/2 + \varepsilon$ along the radial direction, where ε is a positive number. The results are

graphed in Figure 3.2. In Figure 3.2(a), the values are normalized to B_{EMz0}, or the value of B_{EMz} at (*0, 0, Z=1+2ε/l*), given in (3.5):

$$\frac{B_{\mathrm{EMz0}}}{\mu_0 J a_o} = L\ln\left(\frac{1+\rho_{o-}}{a_r+\rho_{i-}}\right) + L\left(\frac{\varepsilon}{l}\right)\ln\left[\frac{(1+\rho_{o-})(a_r+\rho_{i+})}{(1+\rho_{o+})(a_r+\rho_{i-})}\right] \tag{3.5}$$

where $\rho_{o+} = \sqrt{4L^2(\varepsilon/l)^2+1}$; $\rho_{o-} = \sqrt{4L^2(1+\varepsilon/l)^2+1}$; $\rho_{i+} = \sqrt{4L^2(\varepsilon/l)^2+a_r^2}$; and $\rho_{i-} = \sqrt{4L^2(1+\varepsilon/l)^2+a_r^2}$. When $\varepsilon/l \ll 1$ or near the physical boundary,

$$\left.\frac{B_{\mathrm{EMz0}}}{\mu_0 Jl/2}\right|_{(\varepsilon/l)\to 0} = \ln\left(\frac{1+\sqrt{1+4L^2}}{a_r+\sqrt{a_r^2+4L^2}}\right) \tag{3.6}$$

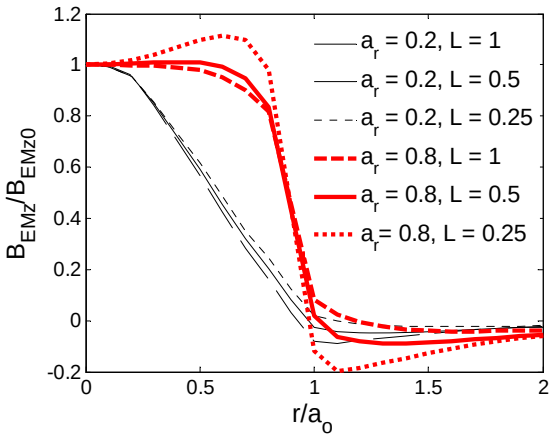

(a) Radial distribution of B_{EMz}

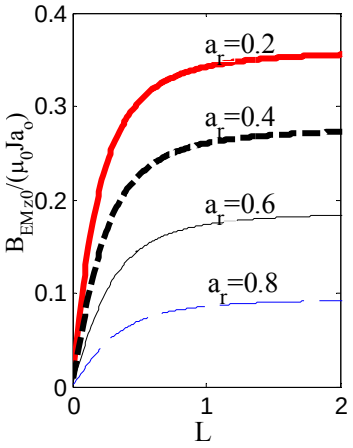

(c) Effect of L

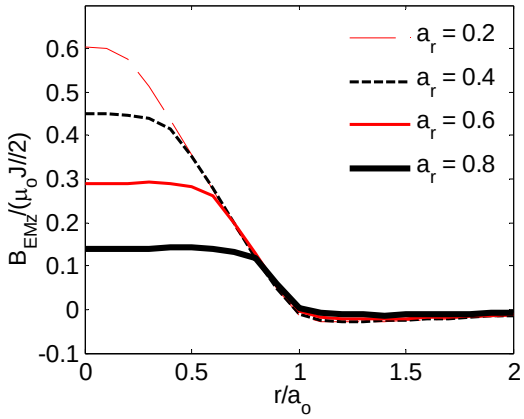

(b) Effect of a_r (L=0.5)

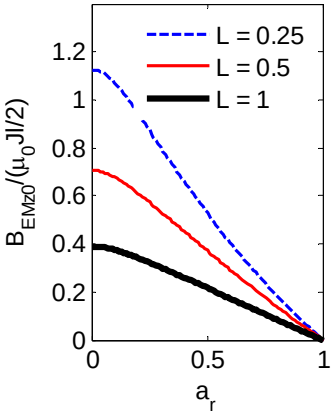

(d) Effect of a_r

Figure 3.2 Effect of a_r and L and on B_{EMz0} (ε/l=0.01)

Some observations can be made in Figure 3.2:

- As shown in Figure 3.2(a) and (b), B_{EMz} linearly decreases from a_i to a_o along the radial direction. When $0.25 \le L \le 1$, B_{EMz} is relatively uniform inside the air core. B_{EMz0} increases with coil thickness (or smaller a_r) for the same a_o and l implying that thicker coils have higher magnetic fluxes (proportional to the area under the curve).
- Figure 3.2(c) shows that the drop in B_{EMz0} is approximately linear with a_r. B_{EMz0}, however, increases exponentially with L and approaches a constant for a given a_r, Figure 3.2(d).

3.2.2 Equivalent Magnetization of the ePM

For a cylindrical PM, **M** is zero outside the physical boundary where $r \ge a_o$. This and the above observations suggest that the magnetization of the ePM takes the form

$$\mathbf{M} = M(r)\mathbf{e_z} \quad \text{where} \begin{cases} M(r) = M_o, & 0 \le r < a_i \\ M(r) = M_o - J(r - a_i), & a_i \le r \le a_o \end{cases} \tag{3.7}$$

where M_0 is an integral constant to be found by comparing (3.1) and (3.2). Since the cylindrical ePM has a maximum along its magnetization, we find M_0 from $B_{\mathrm{PMz}} = B_{\mathrm{EMz}}$ at $(0, 0, l/2 + \varepsilon)$. Substituting (3.7) into (3.1) and noting that $\nabla \bullet \mathbf{M} = 0$, the first term on the right side of (3.3) disappears, and the second term can be written as:

$$\frac{B_{\mathrm{PMz0}}}{\mu_0 Jl/2} = \frac{B_{\mathrm{EMz0}}}{\mu_0 Jl/2} + \frac{1}{Jl}\left[J\left(a_o - a_i\right) - M_0\right]\left(\frac{\varepsilon}{\rho_{o+} a_o} - \frac{l+\varepsilon}{\rho_{o-} a_o}\right) \tag{3.8}$$

M_0 can now be determined by equating the last term of (3.8) to zero such that B_{PMz0}=B_{EMz0}. As the factor involving the independent variable ε is not always zero,

$M(r) = J(a_o - a_i)$. Hence, the equivalent magnetization **M** graphically illustrated in Figure 3.3(a) is given by (3.9):

$$\mathbf{M} = M(r)\mathbf{e_z} \quad \text{where} \begin{cases} M(r) = J \cdot (a_o - a_i), & 0 \le r < a_i \\ M(r) = J \cdot (a_o - r), & a_i \le r \le a_o \end{cases} \tag{3.9}$$

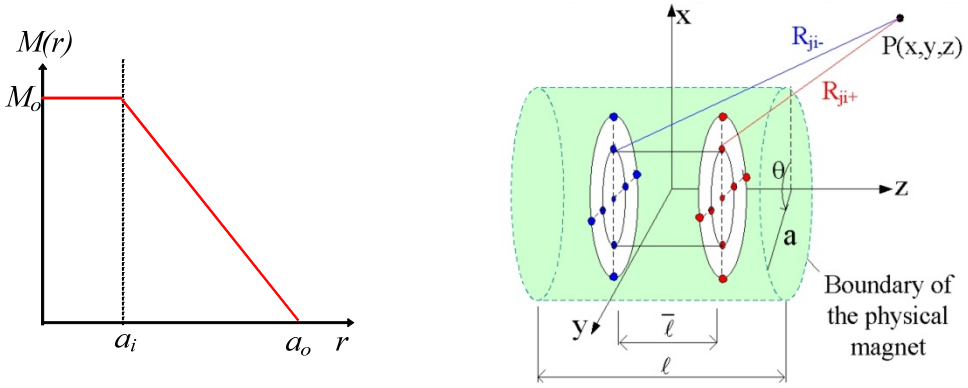

(a) Equivalent **M** (b) Dipole distribution [22]

Figure 3.3 DMP model of a Magnet

Since J is uniform throughout the entire volume of an EM, substituting (3.9) into (3.2) yields:

$$\mathbf{B}_{\text{ePM}} = \frac{J\mu_0}{4\pi}\int_V \frac{-(\nabla \bullet \hat{\mathbf{M}})(\mathbf{R}-\mathbf{R}')}{|\mathbf{R}-\mathbf{R}'|^3}dV + \frac{\mu_0}{4\pi}\int_S \frac{(\hat{\mathbf{M}} \bullet \mathbf{n})(\mathbf{R}-\mathbf{R}')}{|\mathbf{R}-\mathbf{R}'|^3}dS \tag{3.10a}$$

$$\text{where } \hat{\mathbf{M}} = \mathbf{M}/J \tag{3.10b}$$

Once the ePM is found with the equivalent magnetization (3.10b), the EM can be modeled using a distributed set of multi-poles (DMP). For a cylindrical PM, the DMP consists of k circular loops of n equally spaced dipoles parallel to the magnetization vector as shown in Fig. 3.3(b). The loops (each with radius $\bar{a}_j$) are uniformly spaced:

$$\bar{a}_j = a_o j / (k+1) \text{ at } z = \pm \bar{\ell} / 2, \text{ where } 0 \le j \le k \tag{3.11}$$

The flux density at point P(*x, y, z*) generated by a PM or an EM can be computed using:

$$\mathbf{B}_{PM} = \frac{\mu_0}{4\pi} \sum_{i=0}^{k} m_i \sum_{j=1}^{n} \left(\frac{\mathbf{R}_{ij+}}{\left|\mathbf{R}_{ij+}\right|^3} - \frac{\mathbf{R}_{ij-}}{\left|\mathbf{R}_{ij-}\right|^3} \right) \tag{3.12a}$$

$$\mathbf{B}_{EM} = \frac{J\mu_0}{4\pi} \sum_{i=0}^{k} m_i \sum_{j=1}^{n} \left(\frac{\mathbf{R}_{ij+}}{\left|\mathbf{R}_{ij+}\right|^3} - \frac{\mathbf{R}_{ij-}}{\left|\mathbf{R}_{ij-}\right|^3} \right) \tag{3.12b}$$

$$J = 2N_W \cdot I / \sigma \tag{3.12c}$$

where $\mathbf{R}_{ij+}$ and $\mathbf{R}_{ij-}$ are the vectors from the source and sink of the j^{th} dipole on the i^{th} loop to **P** respectively; I is the current flowing in the EM; N_W and σ are the number of turns and the cross-section area of the winding. The procedure of deriving the parameters (k, n, $\bar{l}$ and m_i) can be found in [22].

3.3 Dipole Force/Torque Model

Two methods commonly used in calculating the forces between stator EMs and rotor PMs of a spherical motor are the Lorentz force equation and the Maxwell stress tensor [43]. These methods require solving the magnetic field and computing a volume or surface integral to derive the force model. As general closed-form solutions are not available, the volume or surface integrals are often solved numerically.

An alternative method to compute the magnetic force is the Lorentz force law in analogy to that on an electric charge as illustrated in Figure 3.4, where we define a dipole (with strength m) as a pair of source and sink separated by a finite distance. The force **F** and torque **T** acting on the dipole can be written (in analogy to that on a

stationary electric charge by the Lorentz law) [49] as

$$\mathbf{F} = \mu_o m\left[\mathbf{H}_{R+} - \mathbf{H}_{R-}\right] \tag{3.13a}$$

$$\mathbf{T} = \mu_o m\left[\mathbf{R}_{+} \times \mathbf{H}_{R+} - \mathbf{R}_{-} \times \mathbf{H}_{R-}\right] \tag{3.13b}$$

where μ_0 is free space permeability; H_{R+} and H_{R-} are the magnetic field intensities acting on the magnetic source and sink of the dipole respectively; and the subscripts; and R_+ and R_- are the corresponding distances from a field point.

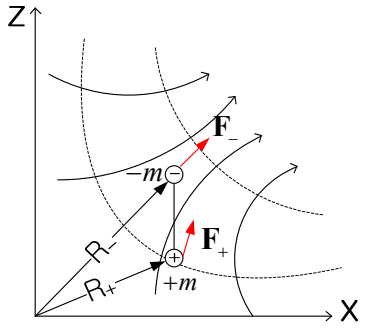

Figure 3.4 Force on dipoles

With both the PMs and EMs are modeled using DMP, the magnetic forces on the system can be calculated using the Maxwell stress tensor method or the dipole force equation. Unlike the commonly used Lorentz force equation and the Maxwell stress tensor method, the dipole force equation (replacing integrations with summations) dramatically reduces computation time. As will be shown, the closed form dipole model is an efficient way to compute the inverse torque model of an over-actuated system, especially for PMSMs [48] where a large number of stator EMs and PMs are involved.

3.4 Numerical Validation

We validate the DMP derived for a circular EM by comparing the magnetic field distribution and force computation against known solutions. The results are given in Sections *A* and *B* followed by discussions in Section *C*.

3.4.1 Validation of Magnetic Field Computation

As a basis for model validation, we numerically integrate the exact integral (3.4) for the flux density of a multilayer (ML) EM so that the DMP_{EM} model and the ESL approximation can be compared. Since the ESL model is singular at the surface, we plot B_z and B_r along the radial direction at $z=l/2+\varepsilon$ with $\varepsilon=0.5$mm, and B_z along the z axis for the thick EM in Figure 3.5. Table 3.1 lists the dimensions of the EM, and the values of the parameters defining the ESL and DMP_{EM} models.

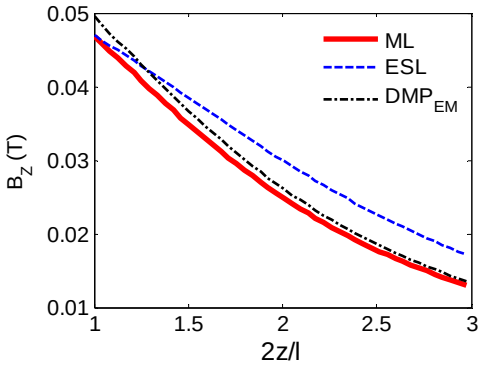

(a) B_z along the z axis

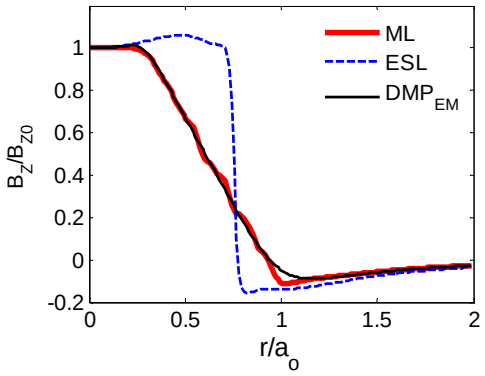

(b) B_z at $\varepsilon = 0.55$mm

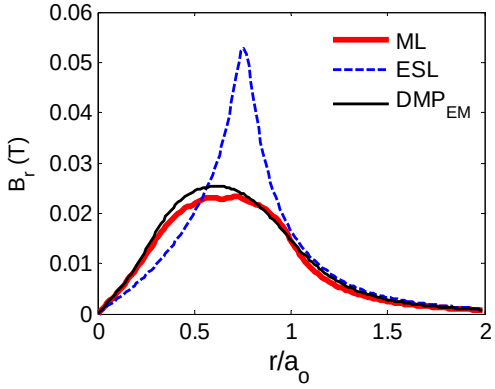

(c) B_r at $\varepsilon = 0.55$mm

Figure 3.5 B_{EMZ} in tesla

Table 3.1 Simulation parameters

	1000 turns, #28 wire, 1A Current
ML:	a_o =15.88mm, a_r=*0.3, L=0.3.*
ESL:	$J_e d_w$=120.1A/mm, a_e=12mm
DMP$_{EM}$:	n=16, k=6, $\bar{l}\,/\,l$ = 0.442
	m_i (μA/m): 1.476, 0.547, 1.618, 1.644, 1.654, 1.325, 0.592

3.4.2 Validation of Magnetic Force Computation

We compute the magnetic force between a PM and an EM for two test setups shown in Figure 3.6. Published experimental force data [50] (numerically validated with a mesh free method in [51]) are available for comparison. In the following computation, the PMs are modeled as DMP$_{PM}$ [22] with the parameters summarized in Table 3.2.

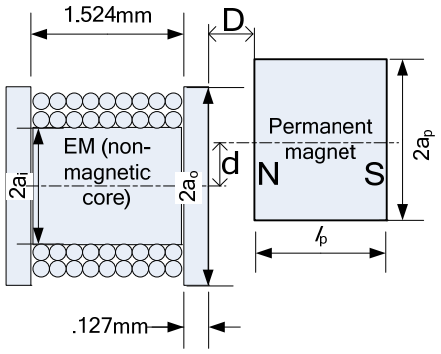

Size	**Large**	**Small**
a_o (mm)	1.981	0.767
a_r	0.7693	0.48
L	0.385	0.48
Coil res. (Ω)	57	32
Wire length (m)	3	1.68
Coil: 280 turns of #47 wire; Current=0.05A		
a_p (mm)	1.499	0.8
L_p	0.533	0.508
Samarium-Cobalt magnet; $\mu_0 M_0$=1.02 T		

Figure 3.6 Experimental setup [50] and parameters

Three different methods for modeling the magnetic fields and forces are compared:

Method I computes the force using Maxwell Stress Tensor.

$$\mathbf{F} = \oint_C \mathbf{T} dC \quad \text{where } \boldsymbol{\Gamma} = \frac{1}{\mu_0}\left(\mathbf{B}(\mathbf{B}\bullet\mathbf{n}) - \frac{1}{2}B^2\mathbf{n}\right) \tag{3.14}$$

and C is an arbitrary boundary enclosing the body of interest; and **n** is the normal of the boundary interface. (3.14) requires the total field **B** (contributed by both the PM and EM) to compute the force by the surface integration. As a basis for comparison, the **B**-field of the multilayer EM numerically computed using (3.1).

Method II calculates the Lorentz force exerted on the current carrying EM

$$\mathbf{F} = -\oint \mathbf{B} \times Id\mathbf{n} \quad \text{where } I = \iint JdS \tag{3.15}$$

where **n** is the unit current direction vector; and S is the cross section of wire. Since the current density vector **J** is directly used in the calculation, only the **B**-field of the PM is needed in the Lorenz force equation (3.15). The multilayer EM is replaced with the equivalent single layer (ESL) model [35] (with equivalent current density J_e, wire diameter d_w, and coil radius a_e), which reduces the volume integral to a surface integral.

Method III uses the dipole force equation in analogy to that on a stationary electric charge by the Lorentz law to compute the net force acting on the PM.

The net force is simply the summation of the individual forces on the dipoles that characterize the PM:

$$\mathbf{F} = \frac{J\mu_0}{4\pi} \sum_{i=1}^{n_r} m_{r_i} \sum_{j=1}^{n_s} m_{s_j} \left(\mathbf{R}_{s_{j+}r_{i+}} - \mathbf{R}_{s_{j+}r_{i-}} + \mathbf{R}_{s_{j-}r_{i-}} - \mathbf{R}_{s_{j-}r_{i+}} \right) \tag{3.16}$$

where $\mathbf{R}_{r_{i\pm}s_{j\pm}} = (\mathbf{R}_{r_{i\pm}} - \mathbf{R}_{s_{j\pm}}) / \left| \mathbf{R}_{r_{i\pm}} - \mathbf{R}_{s_{j\pm}} \right|^3$ where $\mathbf{R}_{r_{i\pm}}(\mathbf{R}_{s_{j\pm}})$ is the i^{th} (j^{th}) pole location of the rotor (EM_j); the signs, (+) and (–), stand for the source and the sink of the dipole; n_r and n_s are the number of dipoles of the PM and EM; and m_{ri} (m_{sj}) are the pole strength of the i^{th} (j^{th}) dipole pair in the rotor (EM_j). The EM is modeled as DMP_{EM}.

The parameters for the ESL model and the DMP_{EM} are summarized in Table 3.2. The magnetic fields of the large and small coils are given in the left and right columns in Figure 3.7, where B_z is plotted along the z axis; and B_z and B_r are plotted along the radial direction at $z=l/2+\varepsilon$ with $\varepsilon=0.5$mm. The computed forces F are compared against published experimental data F_{exp} in Figure 3.8. Table 3.3 compares the time required to compute 26 data points in Figure 3.8(a) using a computer with Quad Core 2.66GHz CPU and 8GB RAM.

Table 3.2 Simulation parameters

	Parameters	**Large**	**Small**
PM	**n, k,** $\bar{l}/l$	6, 2, 0.314	6, 2, 0.3122
DMP_{PM}	m_i (μA/m)	1.65, 0.02, 3.8	0.43, 0.02, 1.07
EM (ESL)	$J_e d_w$ (μA/mm)	22.75	38.98
	a_e (mm)	1.8168	1.456
EM	n, k, $\bar{l}/l$	12, 8, 0.7661	8, 3, 0.7441
(DMP_{EM})	m_i (nA/m)	0.236, 0.177, 0.366, 0.567, 0.751, 0.914,1.032, 1.28, 0.312	1.354, 1.758, 3.32, 1.661

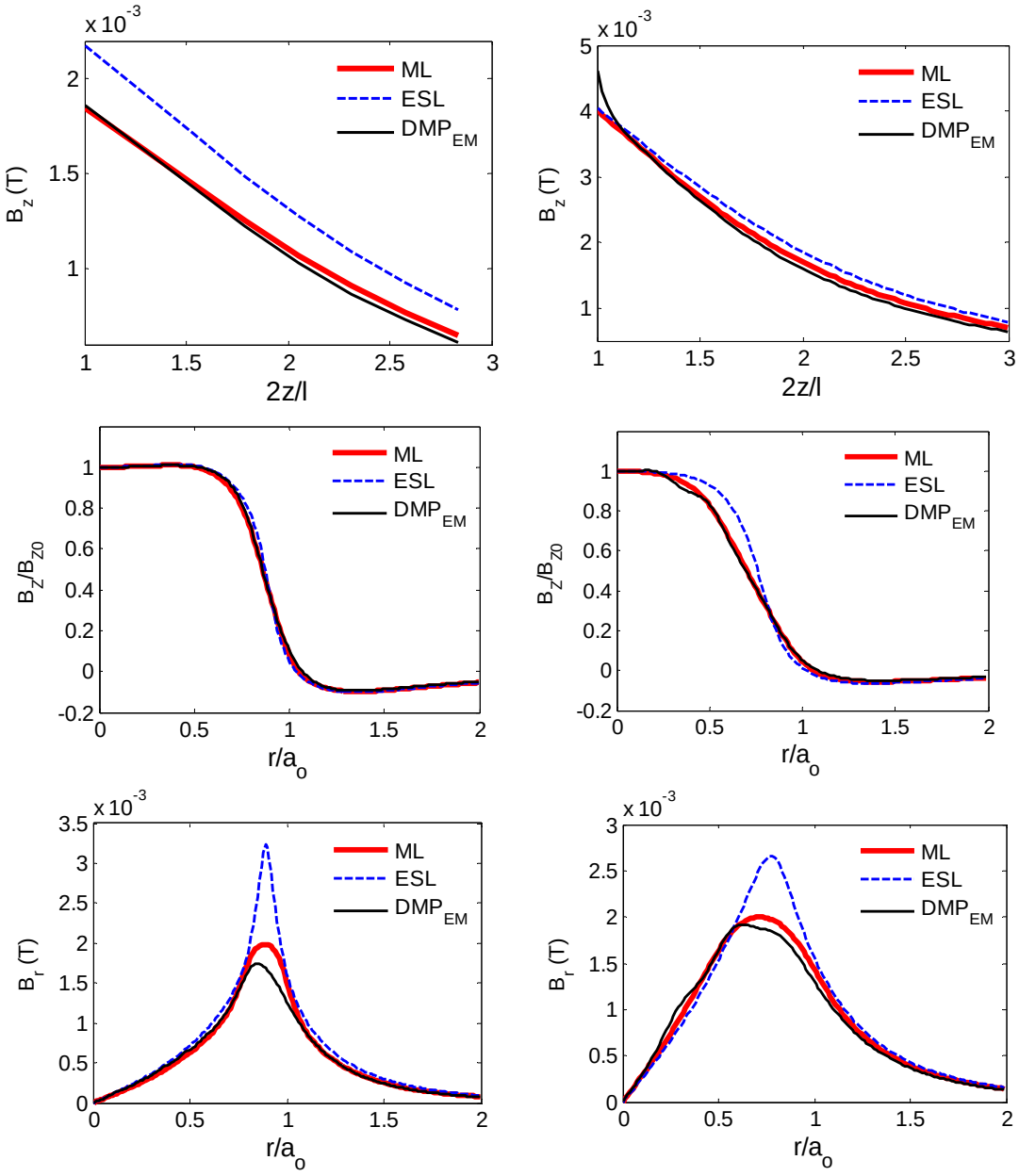

(a) Large (b) Small

Figure 3.7 Computed magnetic flux density

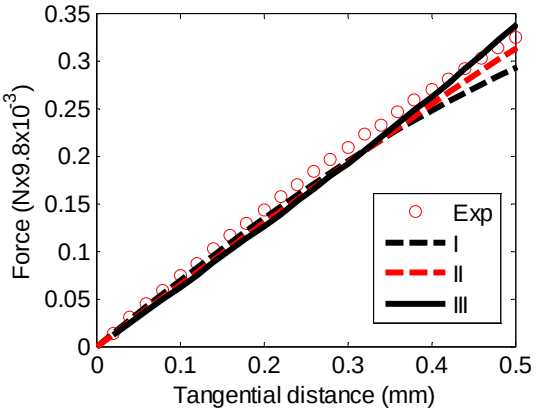

(a) Tangential force, large coil

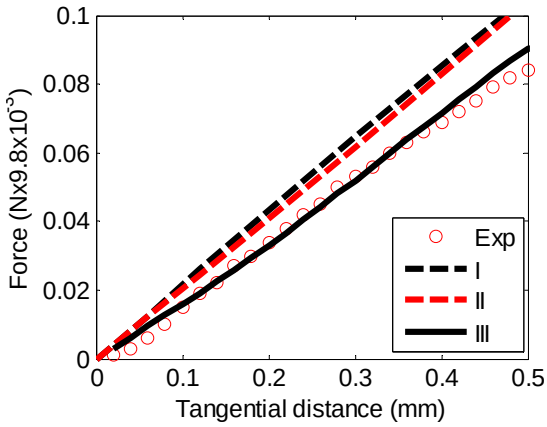

(b) Tangential force, small coil

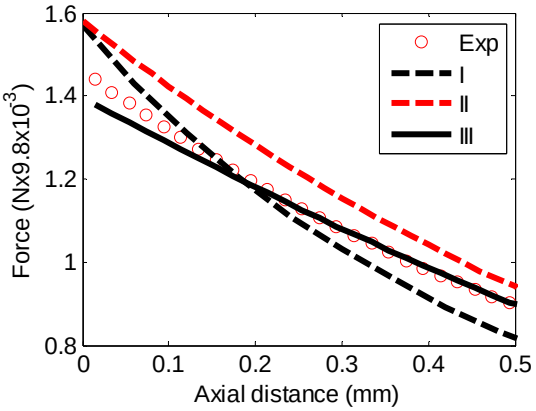

(c) Axial force, large coil

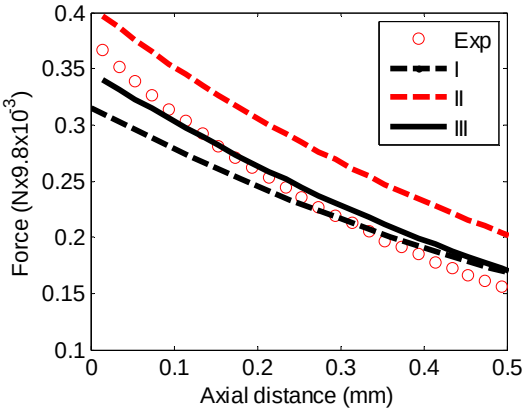

(d) Axial force, small coil

Figure 3.8 Computed forces and experimental data

Table 3.3 Comparison of computational times

Method	**I**	**II**	**III**
Computation Time (sec)	106.03	21.53	0.0625

3.4.3 Discussions of Results

Some observations on Figures 3.6, 3.8, 3.9 and Table 3.3 are discussed as follows:

- Unlike the ESL model where the equivalent current density J_e is determined from the 2D magnetic field, the equivalent magnetization **M** of the ePM is derived using the complete 3D integral. As shown in Figures. 3.6 and 3.8, the DMP_{EM}

modeled flux densities agree very well with the solutions to the exact integral (3.4) for both thin and thick coils. The ESL model provides a reasonable prediction of the z-component flux density, but discrepancies from the exact solutions increase with coil thickness (or smaller a_i / a_o).

- The Maxwell stress tensor in Method I can be computed using the DMP_{PM} and DMP_{EM}, which yields the same solution to the dipole force equation in Method III. However, unlike the Maxwell stress tensor method or the Lorentz force equation (with the ESL approximation) that require numerical computations of a surface integration, the dipole force equation (replacing integrations with summations) is in closed-form dramatically reducing computation to 0.0625sec as compared in Table 3.3.
- As shown in Figure 3.8, the Maxwell stress tensor and the dipole force equation (or Methods I and III respectively) agree very closely with published experimental data while the ESL model (that reduces the volume integral of the multi-layer EM to a surface integral of a single-layer coil) overestimates the computed forces as expected.

3.5 Illustrative Numerical Simulations

With EMs and PMs modeled as DMP, the dipole force model is an efficient way to compute the magnetic for the design of electromagnetic systems that involvs a large number of EMs and PMs.

Observations in Figure 3.2 suggest that both small a_r and L (for a given a_o) have a significant effect on the increase in the z-component magnetic fluxes, and hence on

the compact design of a spherical motor. The effect can be illustrated with the example in Figure 3.9 and Table 3.4, where two pole sizes of a PMSM are compared.

Similar to the force model (3.16), the magnetic torque between EMs and PMs can be computed using dipole force model with the DMP models of EMs and PMs, which has the form:

$$\mathbf{T} = \frac{J\mu_0}{4\pi}\sum_{i=1}^{n_r} m_{r_i} \sum_{j=1}^{n_s} m_{s_j} \left[\left(\mathbf{R}_{s_{j+}r_{i+}} - \mathbf{R}_{s_{j-}r_{i+}} \right) \times \mathbf{R}_{r_{i+}} - \left(\mathbf{R}_{s_{j+}r_{i-}} - \mathbf{R}_{s_{j-}r_{i-}} \right) \times \mathbf{R}_{r_{i-}} \right] \tag{3.17}$$

Design 1 (D1) simulates the torque between the rotor PM and stator EM of the SWM [47] where $L \geq l$ while Design 2 (D2) models that with the same outer radius R_o=76.2mm. In D2, both the PM and EM have a much smaller L of 0.2 and 0.3 respectively and as a result, the rotor PM (embedded in the "socket") has a 1.4 time larger rotational radius than that of D1. The EM in Table 3.1 is used for D2 and repeated here for ease of comparison.

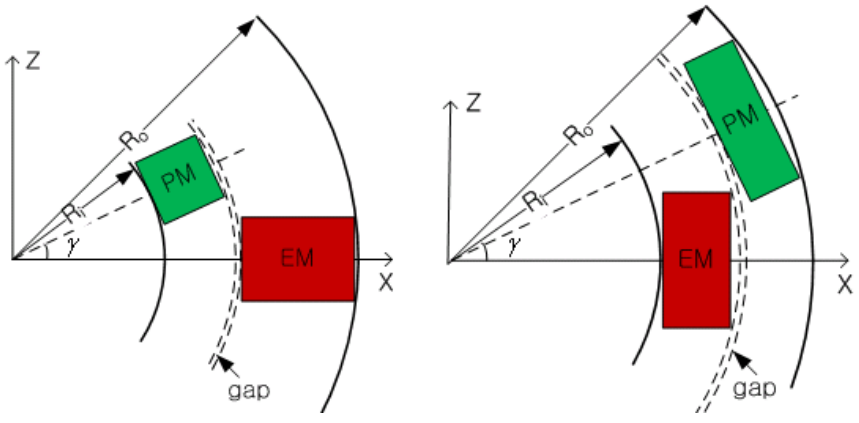

Design 1 (D1) [47] Design 2 (D2)

Figure 3.9 Comparison of design parameters (R_o=76.2mm)

Table 3.4 Parameters used for stator and rotor poles

	Design 1 (D1) [47] R_i = 37.5mm	**Design 2 (D2)** R_i = 52.75mm
PM:	a_o =6.35mm, L=1, $\mu_o M_o$=1.27T	a_o =15.875mm, L=0.2, $\mu_o M_o$=1.27T
DMP_{PM}:	$n=2,\ k=6,\ \bar{l}/l=0.7519$	$n=10,\ k=4,\ \bar{l}/l=0.3$
	m_i (μA/m): 10.64, 1.68, 37.7	m_i(μA/m): 33.5, 24.5, 57.6, 52.0, 276.1
EM:	a_o=9.53mm, a_r=0.5, L=1.33, # of turns =1050	a_o =15.88mm, a_r=0.3, L=0.3, # of turns =1050
DMP_{EM}:	$n=12,\ k=4,\ \bar{l}/l=0.807$	n=16, k=6, $\bar{l}/l$ = 0.442
	m_i (μA/m): -0.152, 0.448, 0.395, 0.515, 0.0563	m_i(μA/m): 1.476, 0.547, 1.618, 1.644, 1.654, 1.325, 0.592

Common parameters: 29AWG, I = 1A, gap = 0.5mm, R_o=76.2mm

The effects of the pole size on the magnetic torque are compared in Figure 3.10 that plots the torque as a function of γ (the separation angle btween the magnetzation axes of PM and EM). As compared to D1 in Figure 3.10, D2 offers 2.4 times higher maximum torque, and converts 3.6 times more mechanical energy (represented by the area under the torque –displacement curve).

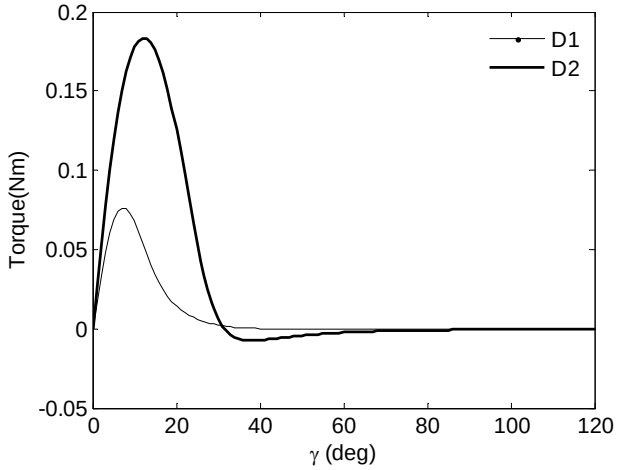

Figure 3.10 Effect of pole geometries on actuator torque

3.6 Conclusion

We have presented a new, time-efficient method for modeling a multilayer EM as an equivalent PM such that the magnetic field of the EM can be characterized using a distribution of multi poles (DMP). The advantage of modeling the PM and EM using DMP has been illustrated through a force computation. Unlike other commonly used methods that often require to calculate a time-consuming numerical (volume or surface) integral to derive the force, the dipole model replacing integrals by summations computes magnetic forces in closed form.

The dipole models have been validated by comparing results against exact field solutions and published experimental force data, which show excellent agreement. The simulation comparing the pole sizes suggests that thick coils (or small a_r) with small L play an effective role to achieve high torque-to-volume ratios, and thus are important in applications where compact coil designs.

Although the method has been discussed in the context of a cylindrical EM (where some analytical and experimental results are also available for model validation), it can be extended to EMs other customized shapes.

CHAPTER 4

NUMERICAL INESTIGATION OF A THREE-DOF PMSM

4.1 Overview

In this chapter, the performances of the static loading as well as DFC method are numerically investigated based on a CAD model of a 3-DOF PMSM [48] with the aid of the DMP model as well as the dipole force model for analyzing the magnetic field and force/torque.

4.2 System Description

Figure 4.1 shows a CAD model of a PMSM [48] developed at Georgia Tech, where the PMSM consists of a rotor (with embedded PMs) supported by a ball bearing on the stator that houses a set of electromagnets (EMs). Both PMs and EMs have their radial magnetization axes passing through the motor center. The EMs are air-cored and the entire structure (except for the PMs) is non-magnetic.

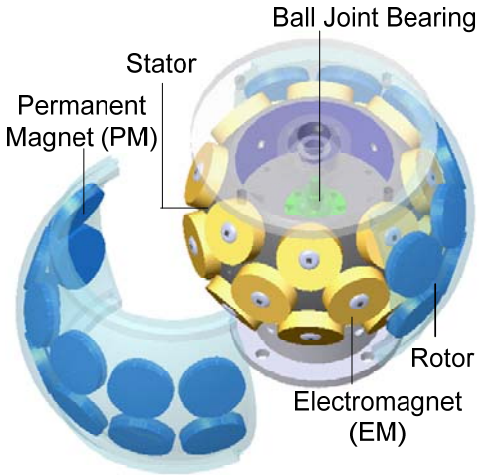

Figure 4.1 CAD model of a PMSM

The coordinate systems are defined in Figure 4.2(a), where XYZ is the stator frame (stationary); *xyz* is the rotor frame; the Euler angles (roll-pitch-yaw) (α,β,γ) describes the rotor orientation in as:

$$\mathbf{q}=[\alpha,\beta,\gamma]^T \tag{4.1}$$

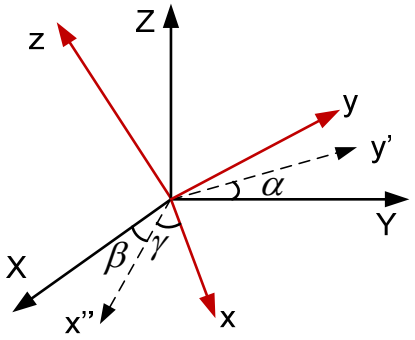

(a) Stator and rotor coordinates and orientation (y' and x'' are intermediate axes)

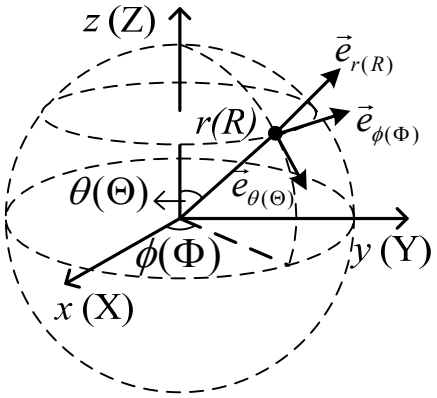

(b) Spherical coordinate in rotor (stator) frame

Figure 4.2 Coordinate systems of PMSM

The locations of the PMs and EMs as well as the magnetic sensors for measuring the MFD are defined with spherical coordinates. As shown in Figure 4.2(b), θ,ϕ,r (Θ,Φ,R) represent the spherical coordinates in xyz (XYZ) frame. The magnetization axes of the PMs or EMs can be characterized by a vector pointing from the origin to the center of each PM and EM. The centroids are defined in terms of spherical coordinates (as shown in Figure 4.1b) in rotor frame (for PMs) and stator frame (for EMs) respectively, which have the following forms:

$$\mathbf{C}_{PMi}=R_{PM}\left[\cos\phi_i\sin\theta_i \quad \sin\phi_i\sin\theta_i \quad \cos\theta_i\right]^{\mathrm{T}} \tag{4.2a}$$

$$\mathbf{C}_{EMj} = R_{EM}\left[\cos\Phi_j \sin\Theta_j \quad \sin\Phi_j \sin\Theta_j \quad \cos\Theta_j\right]^{\mathrm{T}} \tag{4.2b}$$

where *i* and *j* are the indices of the PMs and EMs. The parameters are given in Table 4.1. It is worth noting that the adjacent PMs have alternating magnetizations and the magnetization of each EM is dependent on the instantaneous current direction flowing in the EM. A magnetic sensor for measuring the MFD is fixed in the stator frame and the sensor is placed such that measuring axes are along the Θ, Φ, R directions. The location of a sensing point of and the unit vectors ($\vec{e}_{\Theta}, \vec{e}_{\Phi,} \vec{e}_R$) of the measuring axes are defined in stator frame:

$$\mathbf{C}_{Sp} = R_S\left[\cos\Phi_p \sin\Theta_p \quad \sin\Phi_p \sin\Theta_p \quad \cos\Theta_p\right]^{\mathrm{T}} \tag{4.3a}$$

$$\vec{e}_{\Theta p} = \left[\cos\Theta_p \cos\Phi_p \quad \cos\Theta_p \sin\Phi_p \quad -\sin\Theta_p\right]^T \tag{4.3b}$$

$$\vec{e}_{\Phi p} = \left[-\sin\Phi_p \quad \cos\Phi_p \quad 0\right]^T \tag{4.3c}$$

$$\vec{e}_{Rp} = \left[\sin\Theta_p \cos\Phi_p \quad \sin\Theta_p \sin\Phi_p \quad \cos\Theta_p\right]^T \tag{4.3d}$$

where *p* is the sensor index. The parameters describing the sensor locations are given in Table 4.1. For each sensor, the MFD measured by the p^{th} sensor is:

$$\mathbf{B}_p = (B_{p\Phi}, B_{p\Theta}, B_{pR}) \tag{4.4}$$

Due to the symmetric configuration of the rotor PMs, the magnetic sensors for measuring MFD of the rotor PMs are only placed in half of the sphere. Also, the 24 EMs are grouped in series into pairs leading to a total of 12 electrical inputs (Table 4.2), which are placed symmetrically about the motor center. The operating range of this design is:

$$-22.5^\circ \le \alpha, \beta \le 22.5^\circ \text{ and } -\infty \le \gamma < +\infty \tag{4.5}$$

Table 4.1 Locations of PMs, EMs and sensors

	PM (in *xyz*)		EM (in XYZ)			Sensor(in XYZ)		
Index	1 to 12	13 to 24	1 to 8	9 to16	17 to 24	1 to 8	9 to 16	17 to 24
$\theta(\Theta)$ (deg)	105	75	116	64	0	116	64	0
$\phi(\Phi)$ (deg)	$30(j-1)$	$30(j-13)$	$45(j-1)$	$45(j-9)$	$45(j-17)$ +22.5	$22.5(j-1)$	$22.5(j-9)$	$22.5(j-17)$

R_{PM} = *67.9*mm, R_{EM} = *56.8*mm, R_S= *56.4*mm

Table 4.2 Current input configuration of the EMs

$i_1=i_{13}=u_1$	$i_5=i_9=u_5$	$i_{17}=i_{21}=u_9$
$i_2=i_{14}=u_2$	$i_6=i_{10}=u_6$	$i_{18}=i_{22}=u_{10}$
$i_3=i_{15}=u_3$	$i_7=i_{11}=u_7$	$i_{19}=i_{23}=u_{11}$
$i_4=i_{16}=u_4$	$i_8=i_{12}=u_8$	$i_{20}=i_{24}=u_{12}$

4.3 Static Loading Investigation

When the table is loaded (such as a work piece), the rotor of the three-DOF orientation stage is subjected to an external torque T_{ext} (Figure 4.3), where the center of gravity coincides with the rotation center.

$$T_{ext} = r \times m_{load} g \tag{4.6}$$

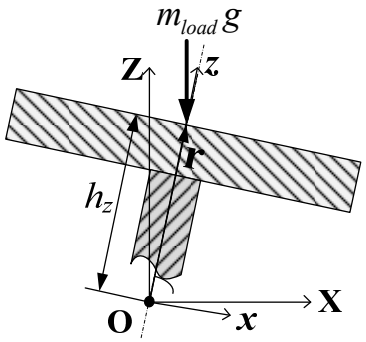

Figure 4.3 Schematic of the external loading

Statically, the torque acting on the rotor is equal to the external torque. The interest here is to simulate the maximum current inputs required meeting a specified torque over the entire operating range given in (4.5).

With the DMP models of the PMs and EMs, the magnetic torque of the PMSM can be computed with the dipole force model (3.13b); and the TCV can be derived from (1.3) and (3.13b),

$$\mathbf{K}_j = \frac{\mu_0}{4\pi} \sum_{i=1}^{N_P \times n_r} m_{r_i} \sum_{p=1}^{n_s} m_{s_p} [(\mathbf{R}_{r_{i+}s_{p+}} - \mathbf{R}_{r_{i+}s_{p-}}) \times \mathbf{R}_{r_{i+}} - (\mathbf{R}_{r_{i-}s_{p+}} + \mathbf{R}_{r_{i-}s_{p-}}) \times \mathbf{R}_{r_{i-}} \qquad (4.7)$$

where $\mathbf{R}_{r_{i\pm}s_{j\pm}} = (\mathbf{R}_{r_{i\pm}} - \mathbf{R}_{s_{j\pm}}) / \left|\mathbf{R}_{r_{i\pm}} - \mathbf{R}_{s_{j\pm}}\right|^3$ where $\mathbf{R}_{r_{i\pm}}(\mathbf{R}_{s_{j\pm}})$ is the i^{th} (j^{th}) pole location of the rotor (EM_j); the signs, (+) and (–), stand for the source and the sink of the dipole respectively; n_r and n_s are the number of dipoles of the PM and EM respectively; N_P is the total number of the PMs; and m_{ri} (m_{sj}) are the pole strength of the i^{th} (j^{th}) dipole pair in the rotor (EM_j). Since the EMs are paired (as shown in Table 4.2), the TCV matrix has the form:

$$\mathbf{K} = \left[\left(\mathbf{K}_1 + \mathbf{K}_{13}\right),\ \left(\mathbf{K}_2 + \mathbf{K}_{14}\right),\ \cdots,\ \left(\mathbf{K}_{20} + \mathbf{K}_{24}\right) \right] \qquad (4.8)$$

The required current inputs for a desired torque can be computed using inverse torque model (1.6). The parameters used in simulating the inverse torque model (1.6) with the component $\mathbf{K}_j$ given by (4.8) are given in Table 4.3 and D2 in and Figure 3.9 and Table 3.4. Figure 4.4 shows the current profiles of each of the current inputs required maintaining the external torque. Each point represents the maximum current magnitude for the orientation $(\alpha,\ \beta,\ 0 \le \gamma \le 360^\circ)$. Except near the boundary, most of the required currents are within 3A. The statistics of the EM required inputs are

summarized in Table 4.4 suggesting that the maximum current required is less 3.4A for the specified load (and rotor weight) of 10kg.

Table 4.3 Simulation parameters

$\mathbf{m_{load}}$ (kg)	$\mathbf{h_z}$ (mm)	**Rotor Mass** (kg)	**Moment of inertia** (kg-m^2)
8	64.8	2.03	$I_{zz}=7.97\times10^{-3}$, $I_{xx}=I_{yy}=5.89\times10^{-3}$

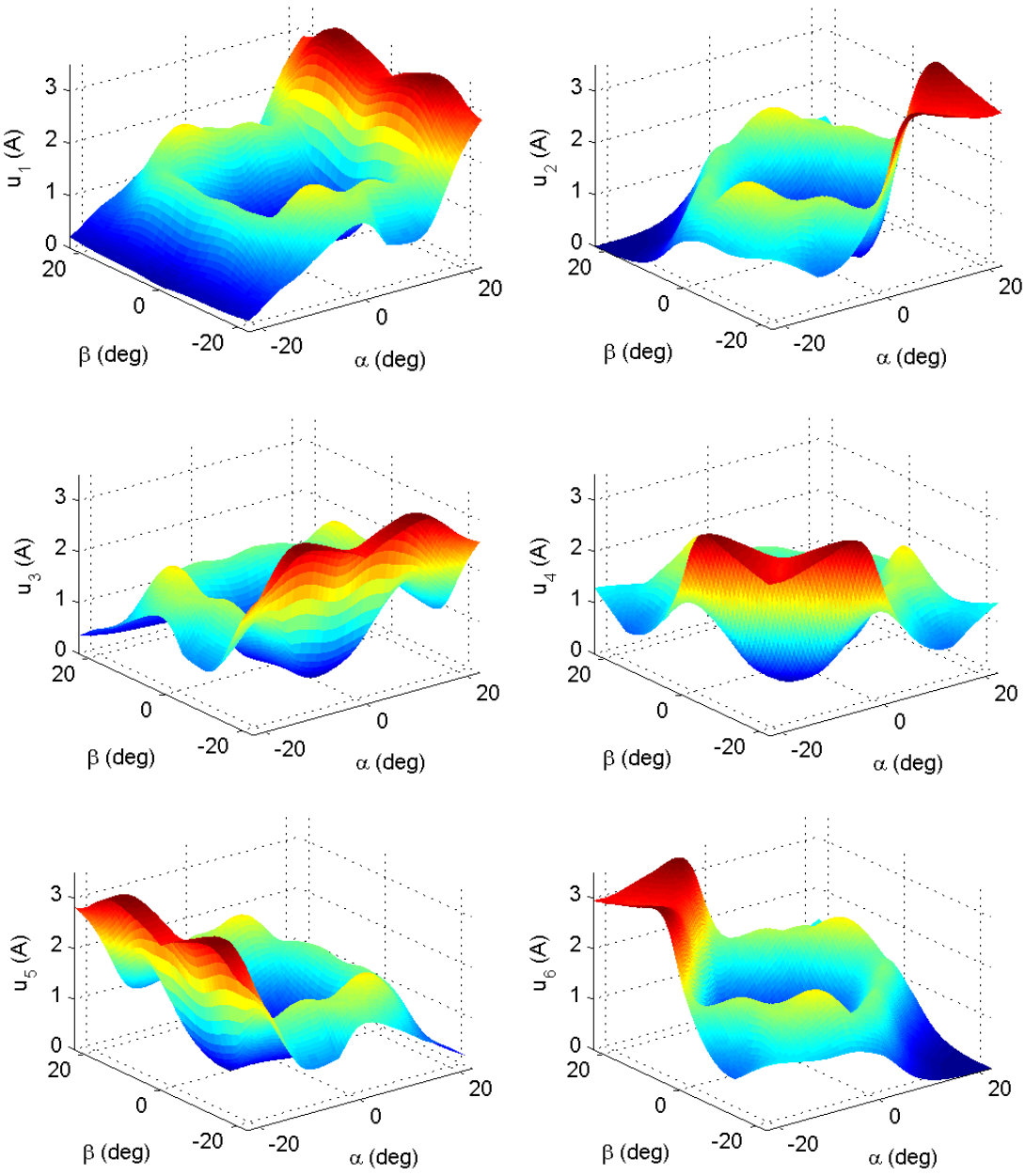

Figure 4.4 Current inputs in each stator EM

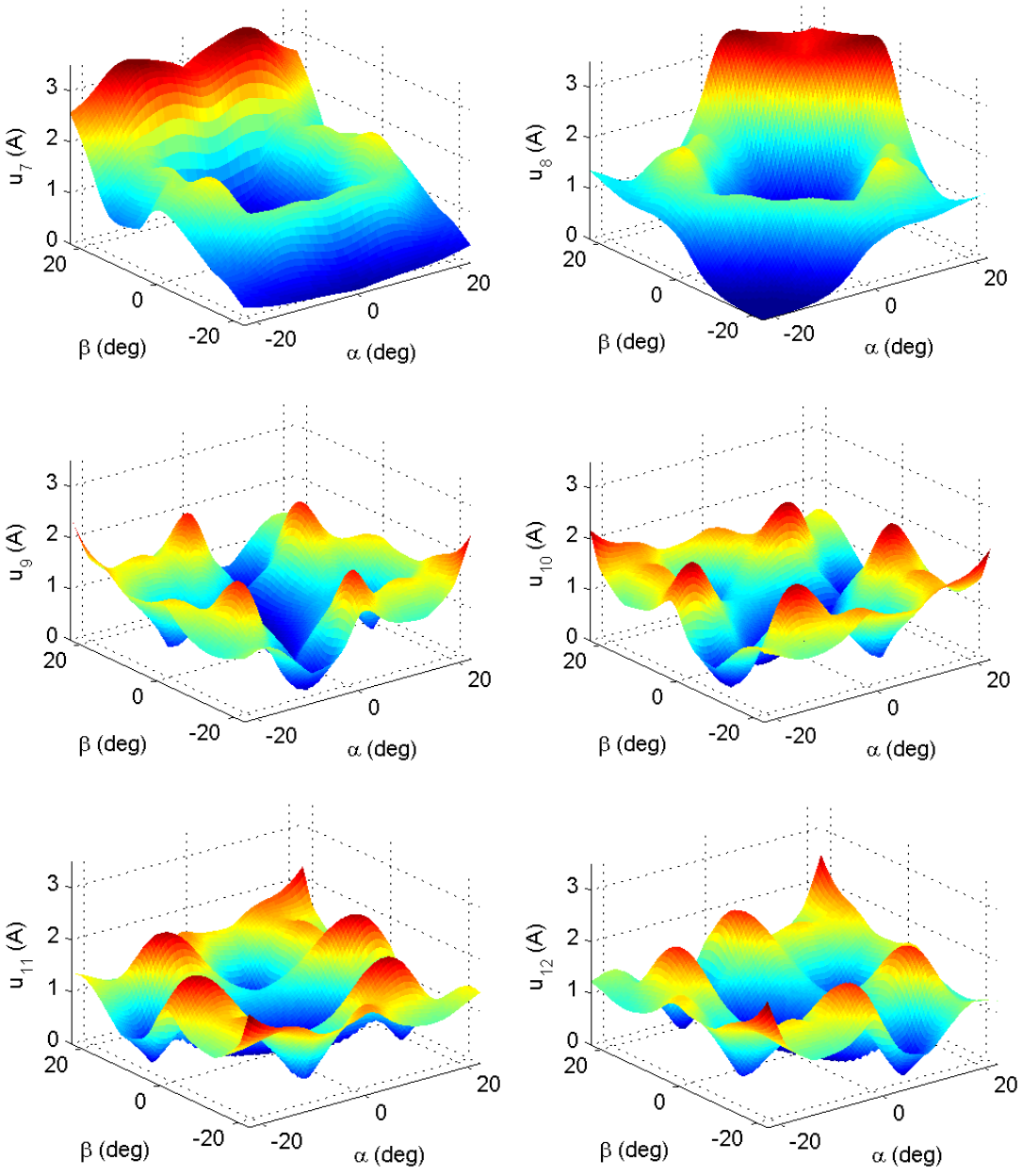

Figure 4.4 (Continued)

Table 4.4 Statistics of current magnitudes (unit: A)

u_i	1	2	3	4	5	6	7	8	9	10	11	12
Max	3.34	3.34	3.35	3.35	3.35	3.35	3.35	3.35	2.45	2.18	2.18	2.45
Mean	1.31	1.28	1.30	1.28	1.31	1.28	1.30	1.28	1.06	1.05	1.05	1.06

4.4 Numerical Investigation with DFC

Here, the DFC method is numerically investigated based on the PMSM (Figure 4.1) where the PM and EM parameters are given by D2 in Figure 3.9 and Table 3.4.

4.4.1 Bijective Domains

The MFD of the rotor PMs can be computed using the DMP model at the sensor measuring points and the bijective domains corresponding to certain sensor measurements can be determined using (2.12) where the Jacobian is derived numerically with respect to the orientation. Due to the periodicity of the rotor PM placement (Figure 4.5), the following discussion focuses on domain Λ with the following range within which the results are sought in the entire working space:

$$\Lambda : -22.5^\circ \le \alpha, \beta \le 22.5^\circ, -30^\circ \le \gamma \le 30^\circ \tag{4.9}$$

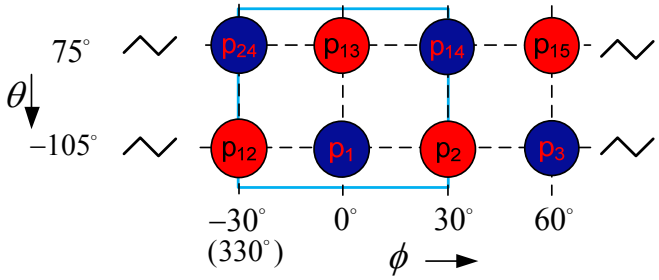

Figure 4.5 PM locations in rotor frame (spherical coordinate)

As an illustration, the MFDs for the following MFD vectors are simulated

$$\mathbf{B}_{\mathrm{SI}} = (B_{21R}, B_{9R}, B_{19R}) \tag{4.10a}$$

$$\mathbf{B}_{\mathrm{SII}} = (B_{13R}, B_{9R}, B_{11R}) \tag{4.10b}$$

where the sensor indices are given in Table 4.1. The Jacobians are computed for each MFD vector using (2.10) and (2.11). Figure 4.6(a) and (b) show the bijective domains

determined by (2.12) of $\mathbf{B}_{SI}$ and $\mathbf{B}_{SII}$ respectively. Here the critical value ε in (2.12) is set to be the mean absolute values (J_0) of the Jacobians over the entire range in each case, which are shown in Figure 4.6. The red and blue volumes in Figure 4.6 represent the bijective domains of $\mathbf{B}_{SI}$ and $\mathbf{B}_{SII}$ respectively. For visual illustration, the Jacobians for $\mathbf{B}_{SI}$ and $\mathbf{B}_{SII}$ are graphed at β=0 in Figure 4.7 (a, b), where the red and black dotted lines represent the boundaries of the bijective domains. It can be seen that the bijective domains of each MFD vectors are scattered and correspond to different ranges in Λ.

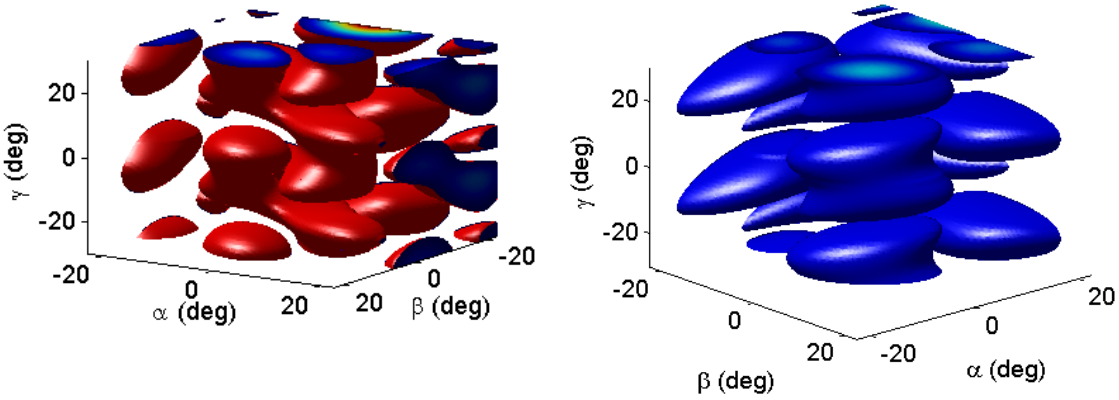

(a) $\mathbf{B}_{SI}$, $J_0 = 460\text{mT}^3/\text{deg}^3$ (b) $\mathbf{B}_{SII}$, $J_0 = 86\text{mT}^3/\text{deg}^3$

Figure 4.6 Bijective domains of different MFD vectors

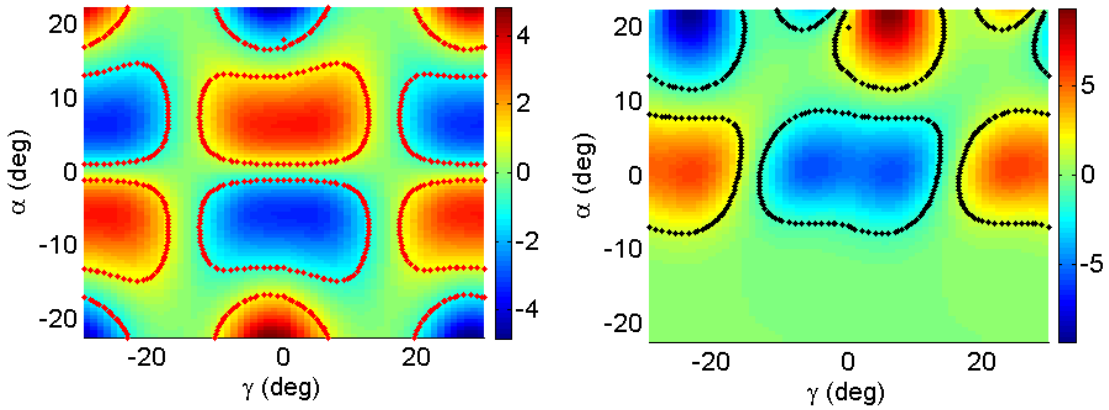

(a) $\mathbf{B}_{SI}$ (b) $\mathbf{B}_{SII}$

Figure 4.7 Jacobians and bijective domains of different MFD vectors at $\beta = 0$

The individual bijective domains in Figure 4.7(a, b) can be connected to form larger domains to enable the DFC to apply in a larger range. As the boundaries of the bijective domains are difficult to define explicitly with MFDs, domains with easy boundary conditions in terms of the MFDs and completely enclosed by the bijective domains can be found. Figure 4.8 (a, b) display the MFDs of B_{21R} and B_{13R} respectively with the boundaries of the bijective domains of $\mathbf{B}_{SI}$ and $\mathbf{B}_{SII}$ superimposed on the figures. For simplicity, the MFD and bijective domains were only graphed in the following range:

$$-15^{\circ} \le \alpha, \gamma \le 15^{\circ}, \beta = 0$$

Figure 4.9 depicts the boundaries of the bijective domains (Γ's) and the MFD-defined domains (Ω's) where the boundary conditions of the Ω's are shown on the right. Note that there are two isolated regions for Γ and Ω of $\mathbf{B}_{SI}$ and they are denoted by "+" (for α>0) and "-" (for α>0) respectively. It can be seen that each MFD-defined domain is enclosed by a bijective domain. These MFD-defined domains can also form a larger domain where bijections are ensured. Therefore, the DFC method can be applied in this connected domain by switching the controlled MFD vector from $\mathbf{B}_{SI}$ and $\mathbf{B}_{SII}$ while the switching criteria are the boundary conditions of the MFD-defined domains. The overlapped areas in the connected domain ensure that the system does not have singularities on the boundaries since the bijection is satisfied on either side.

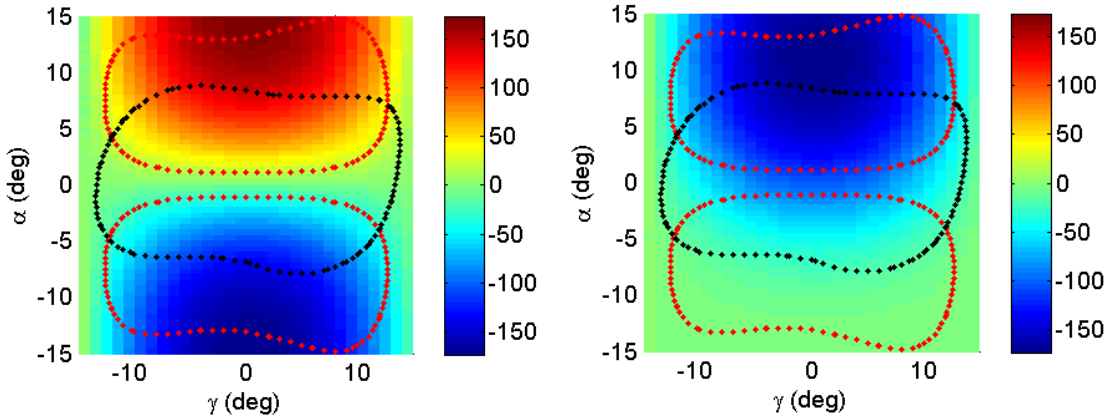

(a) B_{21R} (mT) and bijective domains (b) B_{13R} (mT) and bijective domains

Figure 4.8 MFDs superimposed with boundaries of bijective domains

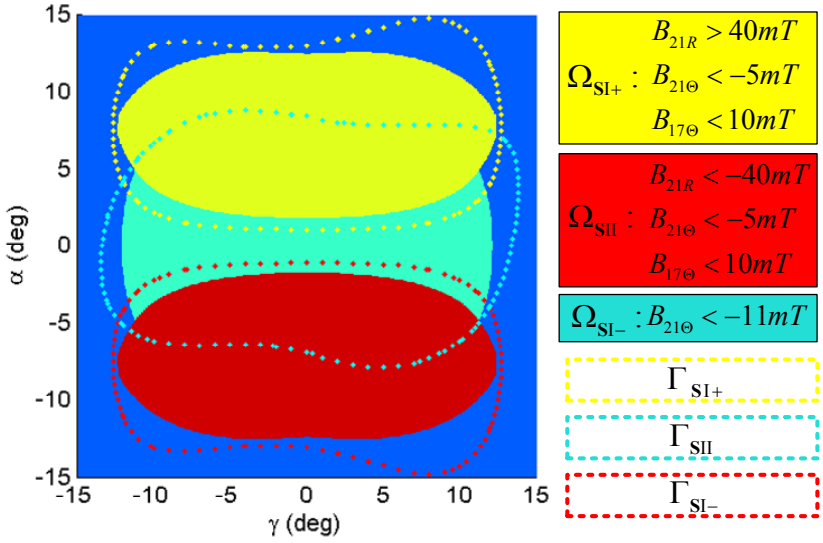

Figure 4.9 MFD-defined domains and bijective domains

Similarly, the bijective domains of other MFD vectors can be found. Figure 4.10 roughly summarizes the MFD vectors and their bijective domains covering Λ. Note that the squares are only for illustration and do not represent the exact boundaries of the bijective domains. The MFD vector coverage can be repeatedly extended to the entire work space of the PMSM as shown in Figure 4.10.

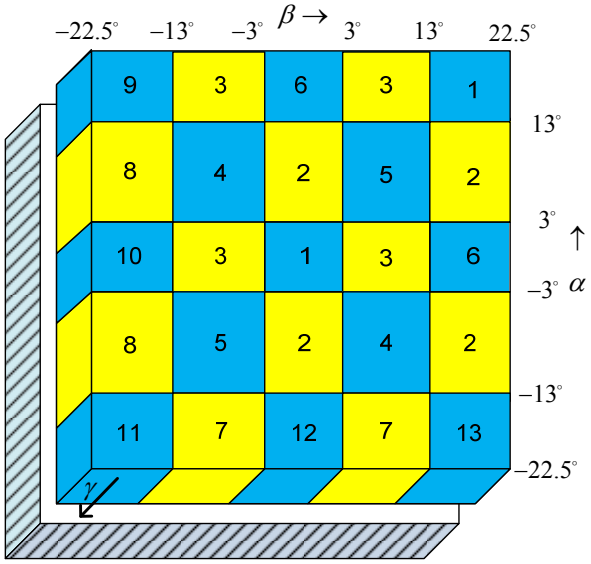

	$0^\circ \le \gamma < 15^\circ$ or $30^\circ \le \gamma < 45^\circ$	$15^\circ \le \gamma < 30^\circ$ or $45^\circ \le \gamma < 60^\circ$
1	$[B_{13R}, B_{9R}, B_{11R}]$	$[B_{14R}, B_{10R}, B_{12R}]$
2	$[B_{21R}, B_{9R}, B_{19R}]$	$[B_{22R}, B_{10R}, B_{20R}]$
3	$[B_{13R}, B_{17R}, B_{19R}]$	$[B_{14R}, B_{18R}, B_{20R}]$
4	$[B_{21R}, B_{17R}, B_{19R}]$	$[B_{22R}, B_{18R}, B_{20R}]$
5	$[B_{21R}, B_{17R}, B_{11R}]$	$[B_{22R}, B_{18R}, B_{12R}]$
6	$[B_{13R}, B_{9R}, B_{19R}]$	$[B_{14R}, B_{10R}, B_{20R}]$
7	$[B_{5R}, B_{17R}, B_{19R}]$	$[B_{6R}, B_{18R}, B_{20R}]$
8	$[B_{21R}, B_{1R}, B_{19R}]$	$[B_{22R}, B_{2R}, B_{20R}]$
9	$[B_{13R}, B_{1R}, B_{11R}]$	$[B_{14R}, B_{2R}, B_{12R}]$
10	$[B_{13R}, B_{1R}, B_{19R}]$	$[B_{14R}, B_{2R}, B_{20R}]$
11	$[B_{5R}, B_{9R}, B_{19R}]$	$[B_{6R}, B_{10R}, B_{20R}]$
12	$[B_{5R}, B_{9R}, B_{19R}]$	$[B_{6R}, B_{10R}, B_{20R}]$
13	$[B_{5R}, B_{9R}, B_{3R}]$	$[B_{6R}, B_{10R}, B_{4R}]$

Figure 4.10 MFD vector selection in the entire working space

4.4.2 Control Parameter Determination of the DFC System

Following the DFC control law given in (2.16), the PD control law of this 3-DOF system has the form:

$$\mathbf{T}_d = \mathbf{K}_P \mathbf{e}_B + \mathbf{K}_D \dot{\mathbf{e}}_B \tag{4.11a}$$

where

$$\mathbf{e_B} = \mathbf{B}_{\mathbf{S}d} - \mathbf{B_S} \tag{4.11b}$$

The gain matrices of the auxiliary control law (2.18a) are

$$\mathbf{K}'_P = \mathbf{K}_P \mathbf{A} = \begin{bmatrix} k_{p1}a_{11} & k_{p1}a_{12} & k_{p1}a_{13} \\ k_{p2}a_{21} & k_{p2}a_{22} & k_{p2}a_{23} \\ k_{p3}a_{31} & k_{p3}a_{32} & k_{p3}a_{33} \end{bmatrix} \tag{4.12a}$$

$$\mathbf{K}'_D = \mathbf{K}_D \mathbf{A} = \begin{bmatrix} k_{d1}a_{11} & k_{d1}a_{12} & k_{d1}a_{13} \\ k_{d2}a_{21} & k_{d2}a_{22} & k_{d2}a_{23} \\ k_{d3}a_{31} & k_{d3}a_{32} & k_{d3}a_{33} \end{bmatrix} \tag{4.12b}$$

where

$$\mathbf{K}_P = \begin{bmatrix} k_{p1} & 0 & 0 \\ 0 & k_{p2} & 0 \\ 0 & 0 & k_{p3} \end{bmatrix}, \mathbf{K}_D = \begin{bmatrix} k_{d1} & 0 & 0 \\ 0 & k_{d2} & 0 \\ 0 & 0 & k_{d3} \end{bmatrix} \tag{4.12c,d}$$

In (4.12a, b), a_{ij} is bounded by $\partial B_i / \partial q_j$. Table 4.5 summarizes the maximum and minimum values of the partial derivatives within the bijective domain (with the contours representing the boundaries). For any $\mathbf{x} \neq 0$,

$$\mathbf{x}^T(\mathbf{K}_P'\mathbf{A})\mathbf{x} = x_1^2 A + x_2^2 B + x_3^2 C + x_1 x_2 D + x_1 x_3 E + x_2 x_3 F \tag{4.13}$$

where $A = k_{p1}a_{11}$, $B = k_{p2}a_{22}$, $C = k_{p3}a_{33}$, $D = k_{p2}a_{21} + k_{p1}a_{12}$, $E = k_{p3}a_{31} + k_{p1}a_{13}$,

$F = k_{p3}a_{32} + k_{p2}a_{23}$.

For $$D \cdot E \cdot F > 0 \text{ and } D, E, F \neq 0 \tag{4.14a,b}$$

(4.13) can be rewritten in the form:

$$\begin{aligned}&\mathbf{x}^T(\mathbf{K}_P'\mathbf{A})\mathbf{x} \\ &= \left(\sqrt{\frac{DE}{2F}}x_1 + \sqrt{\frac{DF}{2E}}x_2 + \sqrt{\frac{EF}{2D}}x_3\right)^2 + \left(A - \frac{DE}{2F}\right)x_1^2 + \left(B - \frac{DF}{2E}\right)x_2^2 + \left(C - \frac{EF}{2D}\right)x_3^2\end{aligned} \tag{4.15a}$$

which is strictly positive if

$$A > \frac{DE}{2F}, B > \frac{DF}{2E}, C > \frac{EF}{2D} \tag{4.16 a,b,c}$$

Therefore, (4.14) and (4.16) together can be used to determine if the PID gain matrices of the DFC system will make the PID gain matrices of the auxiliary control law (4.12a,b) positive definite, which insures the system stability and convergence. Note that (4.14) and (4.16) are only sufficient conditions for gain matrices of the auxiliary control law being positive definite and analytical solutions for (4.14) and (4.16) cannot be found. However, one can still use (4.14) and (4.16) to check the stability and convergence for any specified values or values in a specified range for the gain matrices of the DFC system. The elements in $\mathbf{K}_D$ can be determined in the same way.

Table 4.5 Element value ranges of the Jacobian matrices for $\mathbf{B}_{SI}$ and $\mathbf{B}_{SII}$ in Γ

Jacobian matrices	Element value ranges (mT/deg)		
$\mathbf{J}(\Omega_{SI+})$	$1.1 \le \frac{\partial B_{21R}}{\partial \alpha} \le 10.9$	$-1.6 \le \frac{\partial B_{21R}}{\partial \beta} \le 1.6$	$-17.3 \le \frac{\partial B_{21R}}{\partial \gamma} \le 17.3$
	$-2.8 \le \frac{\partial B_{9R}}{\partial \alpha} \le 2.8$	$-6.1 \le \frac{\partial B_{9R}}{\partial \beta} \le -4.3$	$-10.9 \le \frac{\partial B_{9R}}{\partial \gamma} \le 10.9$
	$-5.8 \le \frac{\partial B_{19R}}{\partial \alpha} \le 5.8$	$-5.9 \le \frac{\partial B_{19R}}{\partial \beta} \le 5.9$	$4.0 \le \frac{\partial B_{19R}}{\partial \gamma} \le 15.9$
$\mathbf{J}(\Omega_{SI-})$	$1.1 \le \frac{\partial B_{21R}}{\partial \alpha} \le 10.9$	$-1.6 \le \frac{\partial B_{21R}}{\partial \beta} \le 1.6$	$-17.3 \le \frac{\partial B_{21R}}{\partial \gamma} \le 17.3$
	$-2.8 \le \frac{\partial B_{9R}}{\partial \alpha} \le 2.8$	$-6.1 \le \frac{\partial B_{9R}}{\partial \beta} \le -4.3$	$-10.9 \le \frac{\partial B_{9R}}{\partial \gamma} \le 10.9$
	$-5.8 \le \frac{\partial B_{19R}}{\partial \alpha} \le 5.8$	$-5.9 \le \frac{\partial B_{19R}}{\partial \beta} \le 5.9$	$-15.9 \le \frac{\partial B_{19R}}{\partial \gamma} \le -4.0$
$\mathbf{J}(\Omega_{SII})$	$-6.1 \le \frac{\partial B_{13R}}{\partial \alpha} \le -2.1$	$-3.5 \le \frac{\partial B_{13R}}{\partial \beta} \le 3.5$	$-21.6 \le \frac{\partial B_{13R}}{\partial \gamma} \le 21.6$
	$-2.7 \le \frac{\partial B_{9R}}{\partial \alpha} \le 2.7$	$-6.1 \le \frac{\partial B_{9R}}{\partial \beta} \le -2.1$	$-10.6 \le \frac{\partial B_{9R}}{\partial \gamma} \le 10.6$
	$-3.8 \le \frac{\partial B_{11R}}{\partial \alpha} \le 4.9$	$-3.9 \le \frac{\partial B_{11R}}{\partial \beta} \le 4.8$	$-17.7 \le \frac{\partial B_{11R}}{\partial \gamma} \le -3.9$

4.4.3 Simulation of TCV Estimation with ANN

As introduced in Chapter 2, the ANNs can be used to offer a direct mapping for estimating TCVs using MFD measurements. Since the TCV of an EM is dependent on the magnetic fields enclosing the EM, the inputs of an ANN for TCV estimation are selected be to be the MFD measurements from sensors that are close to the EM. As an illustration, the TCV of EM_{17} ($\mathbf{K}_{17}$) and the MFD at 7 sensor measurements are computed with (3.12a) and (4.7) in the entire working space. Figure 4.11 (a) depicts the relative positions of the EMs and the sensors surrounding EM_{17}. An ANN (with 1 hidden layer and 10 nodes) was trained with the computed data (16200 samples). The inputs, outputs as well as the ANN parameters are shown in Figure 4.11(b).

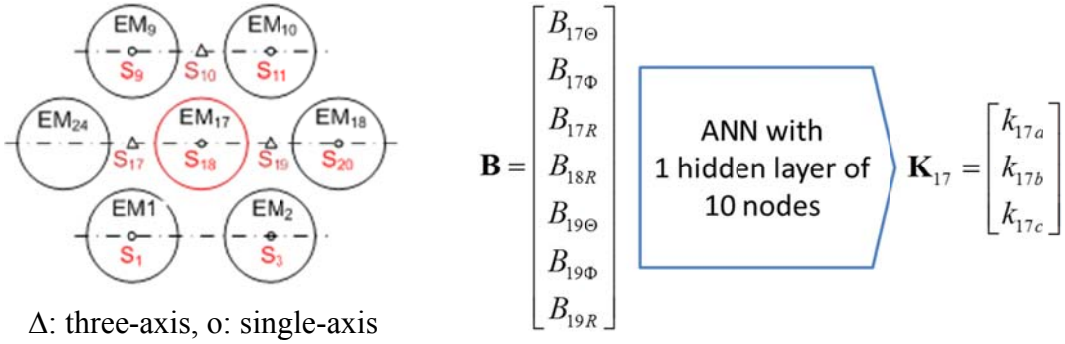

Figure 4.11 ANN parameters, EM and sensor configurations

As a comparison, the components of $\mathbf{K}_{17}$ are estimated with the trained ANN while the rotor follows a trajectory that is given by

$$\alpha = 10^\circ \sin t,\ \beta = 5^\circ \sin t,\ \gamma = 5^\circ,\ t \in [0, 2\pi] \tag{4.17}$$

The estimated results are compared against the analytical results computed using (4.7) in Figure 4.12. It can be seen that the results show excellent agreement. The inputs of the ANNs (with the same structure) for each EM are summarized in Table 4.6.

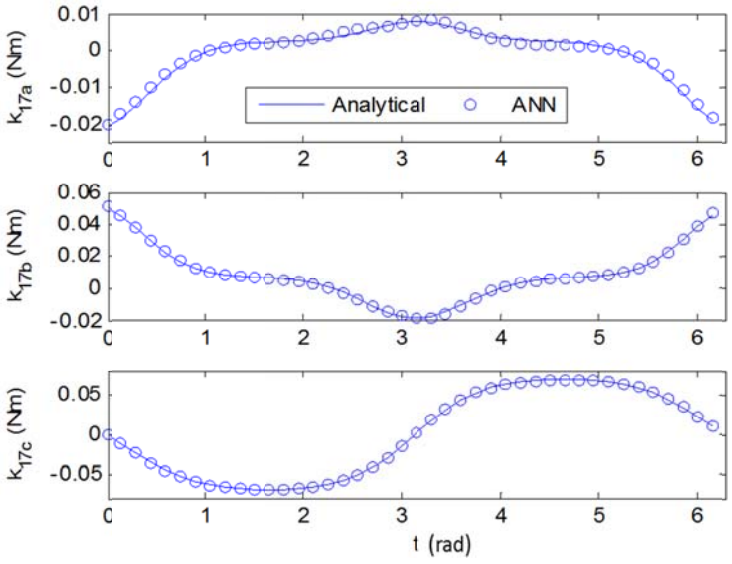

Figure 4.12 Analytical and ANN-estimated results

Table 4.6 ANN inputs for TCV estimation

EM indices	ANN inputs
1,13	B_{1R}, B_{9R}, B_{24R}, $B_{17\Theta}$, $B_{17\Phi}$, B_{17R}, B_{18R}
2,14	B_{3R}, B_{11R}, B_{18R}, $B_{19\Theta}$, $B_{19\Phi}$, B_{19R}, B_{20R}
3,15	B_{5R}, B_{13R}, B_{20R}, $B_{21\Theta}$, $B_{21\Phi}$, B_{21R}, B_{22R}
4,16	B_{7R}, B_{15R}, B_{22R}, $B_{23\Theta}$, $B_{23\Phi}$, B_{13R}, B_{24R}
5,9	B_{1R}, B_{9R}, B_{24R}, $B_{17\Theta}$, $B_{17\Phi}$, B_{17R}, B_{18R}
6,10	B_{3R}, B_{11R}, B_{18R}, $B_{19\Theta}$, $B_{19\Phi}$, B_{19R}, B_{20R}
7,11	B_{5R}, B_{13R}, B_{20R}, $B_{21\Theta}$, $B_{21\Phi}$, B_{21R}, B_{22R}
8,12	B_{7R}, B_{15R}, B_{22R}, $B_{23\Theta}$, $B_{23\Phi}$, B_{13R}, B_{24R}
17,21	$B_{17\Theta}$, $B_{17\Phi}$, B_{17R}, B_{18R}, $B_{19\Theta}$, $B_{19\Phi}$, B_{19R}
18,22	$B_{19\Theta}$, $B_{19\Phi}$, B_{19R}, B_{20R}, $B_{21\Theta}$, $B_{21\Phi}$, B_{21R}
19,23	$B_{21\Theta}$, $B_{21\Phi}$, B_{21R}, B_{22R}, $B_{23\Theta}$, $B_{23\Phi}$, B_{23R}
20,24	$B_{17\Theta}$, $B_{17\Phi}$, B_{17R}, B_{24R}, $B_{23\Theta}$, $B_{23\Phi}$, B_{23R}

4.4.4 DFC Closed-loop Control Simulation

The response was simulated with DFC method when α,β follows the trajectory given in (4.17) and γ changes from the initial state 0 to 5° at 0.1sec. In this simulation, the desired torque was determined by the DFC control law where the controlled MFD vector switched from $\mathbf{B}_{SI}$ and $\mathbf{B}_{SII}$ given in (4.10). The system states went through three different MFD-define domains and the switching criteria are shown in Figure 4.9. The PD gains in each MFD-define domain are:

Ω_{SI+} :
$$K_P = \begin{bmatrix} 40 & 0 & 0 \\ 0 & -48 & 0 \\ 0 & 0 & 16 \end{bmatrix}, K_D = \begin{bmatrix} 2 & 0 & 0 \\ 0 & -3 & 0 \\ 0 & 0 & 0.5 \end{bmatrix}$$

Ω_{SI-} :
$$K_P = \begin{bmatrix} 40 & 0 & 0 \\ 0 & -48 & 0 \\ 0 & 0 & -16 \end{bmatrix}, K_D = \begin{bmatrix} 2 & 0 & 0 \\ 0 & -3 & 0 \\ 0 & 0 & -0.5 \end{bmatrix}$$

Ω_{SII} :

$$K_P = \begin{bmatrix} -30 & 0 & 0 \\ 0 & -34 & 0 \\ 0 & 0 & -5 \end{bmatrix}, K_D = \begin{bmatrix} -1.5 & 0 & 0 \\ 0 & -2 & 0 \\ 0 & 0 & -0.5 \end{bmatrix}$$

Figure 4.13 exhibits the desired and controlled MFDs and the switching sequence of the controlled MFD vector in the domains Ω_{SI+}, Ω_{SI-} and Ω_{SII}. Figure 4.14 shows the simulated orientation and it can be seen that the rotor orientation follows the desired orientation closely. The TCVs were estimated with the trained ANNs and the optimal current inputs obtained from (1.5) are shown in Figure 4.15.

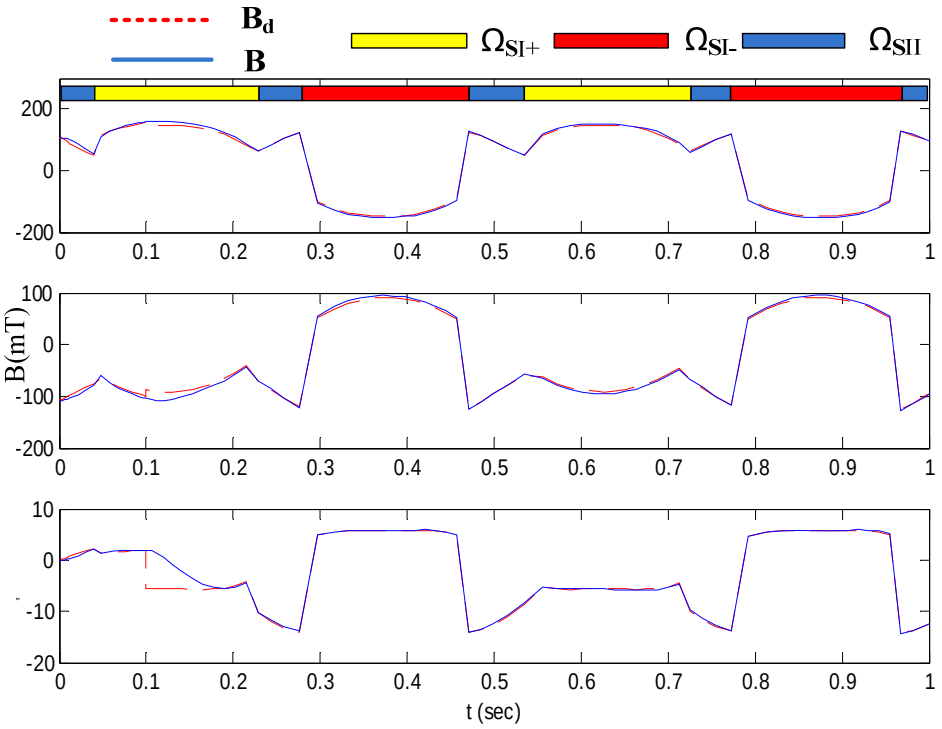

Figure 4.13 MFD response

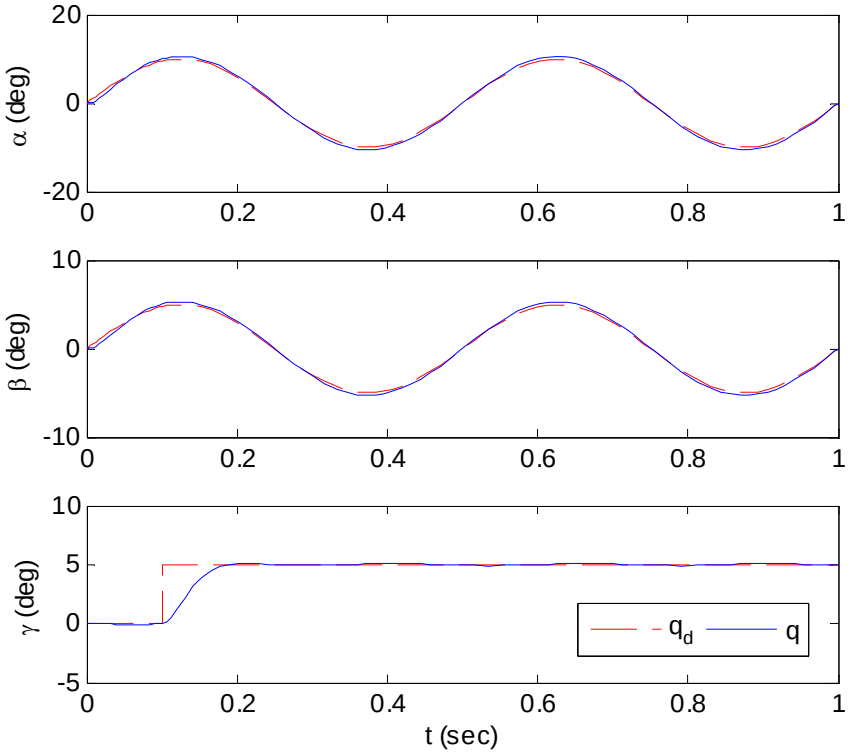

Figure 4.14 Orientation response

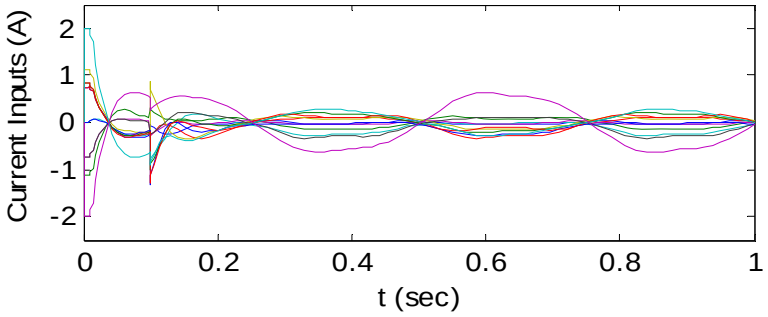

Figure 4.15 Current Inputs: u_1~u_{12}

4.5 Conclusion

In this chapter we have numerically investigated the static loading capacity as well as the DFC system on a PMSM based on the magnetic field and force/torque models presented in Chapter 2. The dipole force model was utilized in the static

loading simulation and the results showed that the PMSM can statically support a loading of 10kg with maximum current inputs at 3.4A. The of dipole force method characterized by its close-form solutions significantly improves the torque computation efficiency. This method, as well as the DMP methods for EMs and PMs, will greatly benefit the design and analysis of PMSMs.

Based on the CAD model of a PMSM, the major components in developing the DFC system were investigated. An in-depth study on the bijective domains shows that the bijection between the orientation and magnetic fields can be analytically characterized using the Jacobians. ANNs were trained and the simulation results show excellent match between the analytical results and ANN-estimated TCVs. The DFC method was simulated and the results show good control performances on the PMSM in 3-DOF motion.

CHAPTER 5

MAGNETIC FIELD CALIBRATION AND RECONSTRUCTION FOR MULTI-DOF PMSMS

5.1 Overview

In this Chapter, the model characterizing the relationship between the rotor orientation and MFDs is established through calibration, which provides a direct correspondence between the rotor orientation and MFDs. To avoid a large amount of measurements, calibration time, and error accumulation in the measurement setup (due to the long and uninterrupted operation) that may affect the calibration accuracy, a new method for reconstructing the 3-D rotor magnetic field from 2-D measurements is presented. This new method has greatly reduced the required measurements as well as the accumulated error. The reconstruction results acquired using the new method is compared with experimental data.

5.2 PMSM with Embedded Field Sensing System

Figure 5.1 shows a PMSM prototype which consists of a rotor (embedded with PMs) and a stator (housing EMs). The rotor consists of 12 PM assemblies with each piece including an aluminum angled plate as shown in Figure 5.1; and two PMs (with opposite poles) secured in the recessed wholes of the plate.

Figure 5.2 exhibits the stator with a hybrid field sensing system for measuring the magnetic fields. The field sensing system consists of two types of sensors: single-axis hall-effect sensors (Allegro, A1302, as shown in Figure 5.2b), and the modified three-

axis sensor as shown in Figure 5.2(c). The latter is constructed by attaching a single-axis sensor on a two-axis sensor (Melexis, MLX91204).

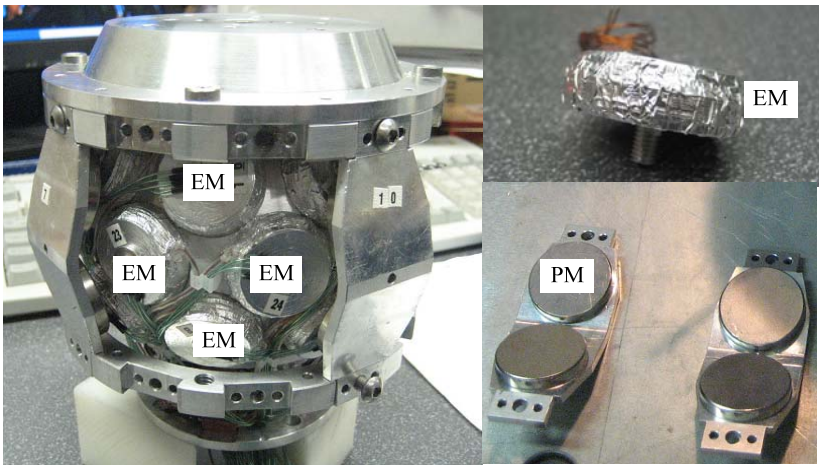

Figure 5.1 PMSM prototype

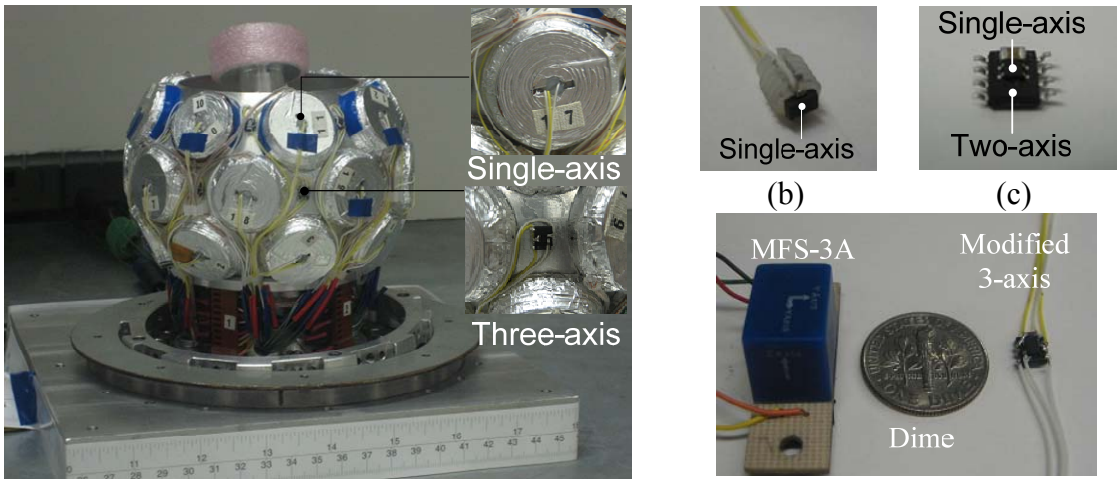

(a) (b) (c) (d)

Figure 5.2 Stator with embedded sensors

The single-axis sensors (that are smaller in size) are installed in the center holes of the EMs. As shown in Figure 5.2(b), a single-axis sensor is attached to a screw (that is secured to the center hole of an EM) so that its measuring axis aligns with the radius of the stator. Existing commercially available three-axis magnetic field

sensors, such as Ametes MFS-3A (Figure 5.2d), usually have bulky size or such as GMR and AMR sensors that have a very small sensing range. Figure 5.2(d) shows that the modified three-axis sensor is relatively compact in size. Also, the sensing range of each component can be adjusted by using different sensors in an assembly. The measuring points of both single-axis and three-axis sensors are at the centroids of the sensors. Figure 5.3 displays the sensor locations and configurations. The detailed sensor measuring points as well as numbering are the same as in Table 4.1. It is worth noting that all sensors are attached (and tangent) to a spherical surface of the stator, where all the centroids of the sensors located as given in Table 4.1.

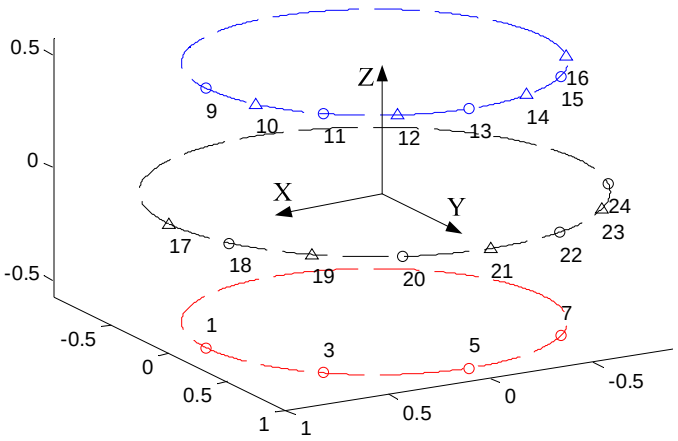

Figure 5.3 Sensor configuration (Δ: three-axis, o: single-axis)

5.3 Reconstruction of Rotor Magnetic Field

The 3-D reconstruction of the rotor MFD is accomplished by means of the installed sensors for a given orientation (α, β, γ). The reconstruction (Figure 5.4) which includes 2-D MFD measurement and real-time extension from the acquired 2-D data into 3-D, can be summarized in the following steps:

Step I: 2-D data acquisition.

The MFD is scanned along longitude and latitude directions (θ and ϕ directions as shown in Figure 4.2b) of the rotor surface. The 2-D MFD data is stored in terms of θ and ϕ with respect to the rotor frame:

$$\mathbf{B}_{rotor} = B_\theta(\theta,\phi)\vec{e}_\theta + B_\phi(\theta,\phi)\vec{e}_\phi + B_r(\theta,\phi)\vec{e}_r \tag{5.1}$$

In (5.1), $\vec{e}_\theta, \vec{e}_\phi, \vec{e}_r$ are the unit vectors at (θ, ϕ, r) in the rotor frame in spherical coordinates:

$$\vec{e}_\theta = \begin{bmatrix}\cos\theta\cos\phi & \cos\theta\sin\phi & -\sin\theta\end{bmatrix}^T \tag{5.2a}$$

$$\vec{e}_\phi = \begin{bmatrix}-\sin\phi & \cos\phi & 0\end{bmatrix}^T \tag{5.2b}$$

$$\vec{e}_r = \begin{bmatrix}\sin\theta\cos\phi & \sin\theta\sin\phi & \cos\theta\end{bmatrix}^T \tag{5.2c}$$

Step II: Coordinate transformation.

At any orientation (α, β, γ), the position of the p^{th} sensor (S_p) can be transformed into the rotor frame. The spherical coordinates of S_p in stator frame (Θ_p, Φ_p, R_p) and in rotor frame (θ_p, ϕ_p, r_p) can be characterized with a rotation between their Cartesian coordinates:

$$\begin{bmatrix}\cos\phi_p\sin\theta_p \\ \sin\phi_p\sin\theta_p \\ \cos\theta_p\end{bmatrix} = [\mathbf{R}]\begin{bmatrix}\cos\Phi_p\sin\Theta_p \\ \sin\Phi_p\sin\Theta_p \\ \cos\Theta_p\end{bmatrix} \tag{5.3a}$$

where $$[\mathbf{R}] = [Rot(\gamma)]\cdot[Rot(\beta)]\cdot[Rot(\alpha)] \tag{5.3b}$$

The spherical coordinates of S_p in rotor frame can be obtained by solving (5.3a). It is worth noting that the radius (distance from the measuring point to motor center) of remains constant during rotation and is not included in (5.3a). The directions of the measuring axes of S_p ($\vec{e}_{\Theta p}, \vec{e}_{\Phi p}, \vec{e}_{Rp}$) can be also transformed into the rotor frame:

$$\vec{e}_{\theta p} = [\mathbf{R}]\vec{e}_{\Theta p}, \vec{e}_{\phi p} = [\mathbf{R}]\vec{e}_{\Phi p}, \vec{e}_{rp} = [\mathbf{R}]\vec{e}_{Rp} \tag{5.4a,b,c}$$

Step III: Data interpolation

With the spherical coordinates of S_p in rotor frame obtained in Step II, the three components $(B_{\theta p}, B_{\phi p}, B_{rp})$ at S_p can be interpolated using the stored 2-D MFD data acquired in Step I; and the total MFD at S_p is:

$$\mathbf{B}_{Sp}(\alpha,\beta,\gamma) = B_\theta(\theta_p,\phi_p)\vec{e}_\theta + B_\phi(\theta_p,\phi_p)\vec{e}_\phi + B_r(\theta_p,\phi_p)\vec{e}_r \tag{5.5}$$

Step IV: 3-D reconstruction

For a specified orientation (α, β, γ), the MFD components along the measuring axes of S_p can be obtained from the dot products of the total MFD with the directions of measuring axes of S_p ($\vec{e}_{\Theta p}, \vec{e}_{\Phi p}, \vec{e}_{Rp}$ acquired in (5.4), which have the form:

$$\begin{bmatrix} B_{\Theta p}(\alpha,\beta,\gamma) \\ B_{\Phi p}(\alpha,\beta,\gamma) \\ B_{Rp}(\alpha,\beta,\gamma) \end{bmatrix} = \begin{bmatrix} \mathbf{B}_{Sp}\cdot\vec{e}_{\theta p} \\ \mathbf{B}_{Sp}\cdot\vec{e}_{\phi p} \\ \mathbf{B}_{Sp}\cdot\vec{e}_{rp} \end{bmatrix} \tag{5.6}$$

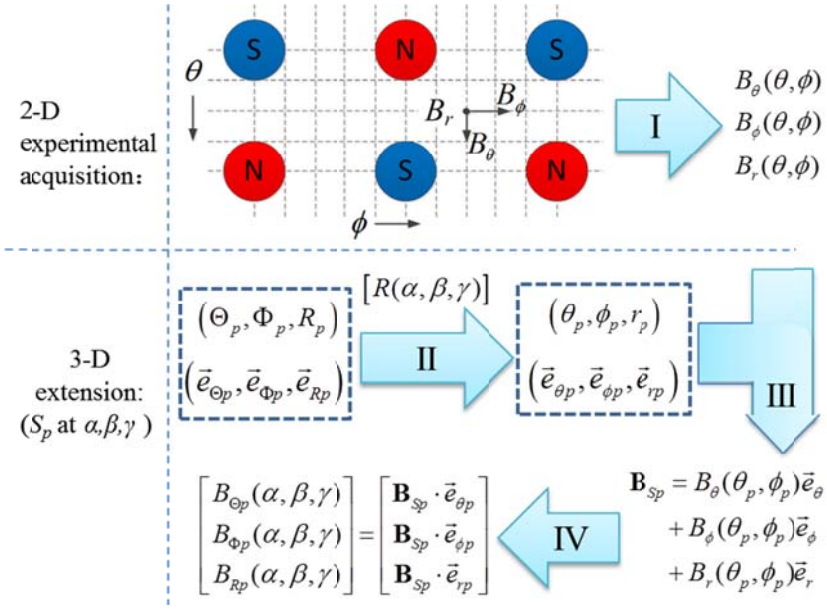

Figure 5.4 3-D reconstruction process for MFDs of S_p

The measurements of the 2-D rotor MFDs can be recorded by either scanning the rotor surface with a moving sensor or by incrementing the rotor motion with fixed sensors. This research focuses on the latter method because the acquired data can be used for both sensor calibration and rotor MFD reconstruction.

5.4 Sensor Calibration

The reconstruction of the rotor magnetic field requires precise information about the actual sensor locations (including the positions of the measuring point as well as the sensor orientation to compensate for the misalignments and inaccuracies during installation.

5.4.1 Sensor and PM Properties

Per the above descriptions about the sensor installation, the following assumptions can be made:

- The placement of of the rotor PMs is accurate and the positions as well as the orientations of each PM embedded in the rotor match the design specifications as given in Table 4.1.
- The magnetic field of each PM is axis-symmetric about its magnetization (center-axis). However, the magnetization strength of each PM may vary.
- The actual and designed locations of S_p can be characterized by Figure 5.5. The actual ($\mathbf{S}$) and designed ($\mathbf{S}'$) positions of the sensor differ by $\delta\Theta$ and $\delta\Phi$ in Θ and Φ directions (in stator frame), as shown in Figure 5.5.
- Sensor surfaces are tangent to the stator sphere so that the *R* axis of each sensor is along the radial direction of the PMSM. For the three-axis sensors, the difference between the actual and designed orientations of a sensor can be characterized by a twist angle τ_p about the *R* axis (as shown in Figure 5.5).

The relationship between the actual measuring axes ($\vec{e}_{\Theta p}$, $\vec{e}_{\Phi p}$ and $\vec{e}_{Rp}$) and the designed measuring axes ($\vec{e}'_{\Theta p}$, $\vec{e}'_{\Phi p}$ and $\vec{e}'_{Rp}$) of S_p can be described using (5.7a-g):

$$\vec{e}_{\Theta p} = \cos\tau_p \cdot \vec{e}'_{\Theta p} + \sin\tau_p \cdot \vec{e}'_{\Phi p} \tag{5.7a}$$

$$\vec{e}_{\Phi p} = \cos\tau_p \cdot \vec{e}'_{\Phi p} - \sin\tau_p \cdot \vec{e}'_{\Theta p} \tag{5.7b}$$

$$\vec{e}_{Rp} = \vec{e}'_{Rp} \tag{5.7c}$$

where
$$\vec{e}'_{\Theta p} = \begin{bmatrix} \cos\Theta_p \cos\Phi_p & \cos\Theta_p \sin\Phi_p & -\sin\Theta_p \end{bmatrix}^T \tag{5.7d}$$

$$\vec{e}'_{\Phi p} = \begin{bmatrix} -\sin\Phi_p & \cos\Phi_p & 0 \end{bmatrix}^T \tag{5.7e}$$

$$\vec{e}'_{Rp} = \begin{bmatrix} \sin\Theta_p \cos\Phi_p & \sin\Theta_p \sin\Phi_p & \cos\Theta_p \end{bmatrix}^T \tag{5.7f}$$

and
$$-90^\circ < \tau_p < 90^\circ \tag{5.7g}$$

It is worth noting that the designed measuring axes in (5.7d-f) depend on the actual positions of the measuring point and the twist angle can be found only after the actual sensor positions are determined in the sensor calibration process.

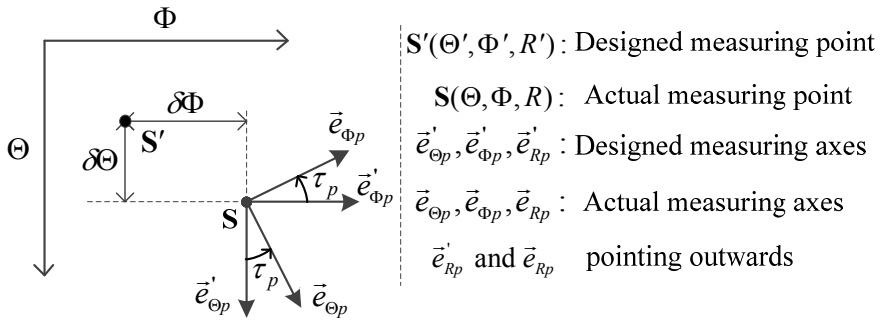

Figure 5.5 Illustration of the desired and actual sensor locations of S_p

In order to facilitate the calibration, some properties about the magnetic field of the rotor PMs are studied.

Figure 5.6(a) shows the results of the normal and tangential MFD of a rotor PM computed using (3.12a) where the PM parameters are given in Figure 3.9 (D2). The

measuring point (S) and measuring axes are illustrated in Figure 5.6(b), where λ is the separation angle between the sensor and the magnetization of the PM. As shown in Figure 5.6, for both the normal (B_n) and tangential (B_t) components, the MFDs vanish dramatically when $|\lambda|$ gets larger and the values are smaller than 2% of the maxima of B_{n} and B_{t} respectively when $|\lambda|$ is larger than 30° (denoted by the dashed lines).

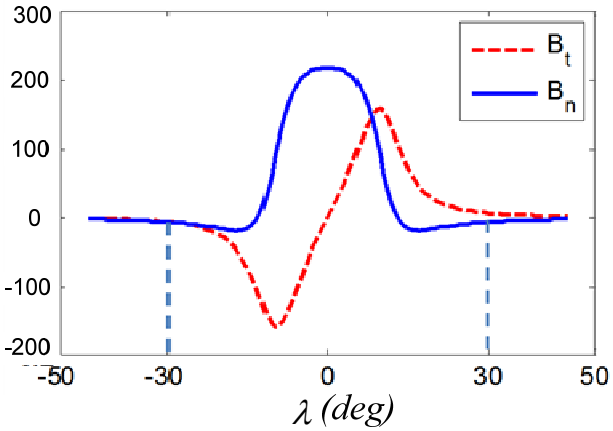

(b) Normal and tangential MFD (unit: T)

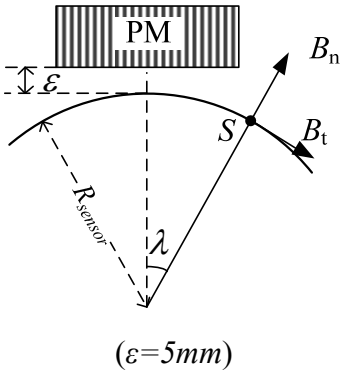

(a) Illustration of measuring point

Figure 5.6 MFDs of single PM

Figure 5.7 depicts the relative positions of rotor PMs, where the line segments and the numbers in between represent the separation angles between the magnetizations of neighboring PMs. Due to the alternating configuration of rotor PMs, only 6 PMs (of total number of 24) are shown. To facilitate visual illustration of the rotor MFDs, Figure 5.8 graphs the simulated rotor MFDs with respect to the rotor frame which are computed with (3.12a). In order to mimic the real situation, the simulation takes into account the variations of the magnetization strengths of the PMs and the parameters are given in Table 5.1.

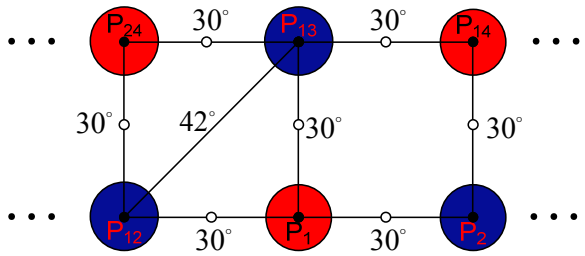

Figure 5.7 Relative positions of PMs

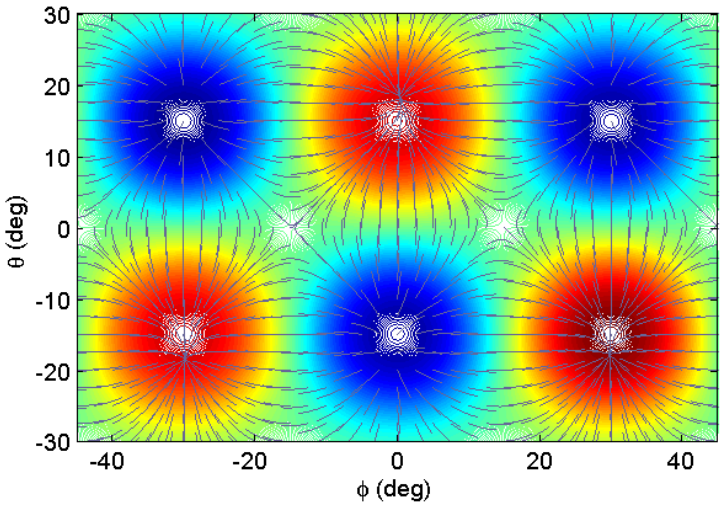

Figure 5.8 Simulated MFDs of rotor PMs (colors represent magnitudes of normal MFDs, streamlines represent directions of tangential MFDs)

Table 5.1 Simulation parameters of PM magnetization strengths ($\mu_0 M_0$ = 1.465T)

PM index	1	2	12	13	14	24
Magnetization strength	$1.1M_0$	$1.05M_0$	$1.2M_0$	$0.95\ M_0$	$1.15M_0$	$1.1M_0$

Based on the above-mentioned properties of the PM MFDs, observations from Figures 5.7 and 5.8 are discussed as follows:

- As seen in Figure 5.7, the separation angles between a PM and any of the neighboring PMs are greater or equal to 30°. Therefore, in the small region around

the center of one PM, the effects of other PMs can be neglected. As the maximum (or minimum for PM with opposite magnetization) of normal MFDs appears at the center of a PM (as shown in Figure 5.6), the local extremes of normal MFDs correspond to PM centers, as shown in Figure 5.8.

- Figures 5.6 and 5.7 show that the separation angles between any point (denoted by the dots in Figure 5.7) of a line segment connecting two PMs with opposite poles and the centers of the other PMs are larger than 30°. Therefore, the tangential MFDs on these line segments are strictly along these lines since the effects of the other PMs are negligible.

5.4.2 Calibration of Sensor Locations

The sensor locations can be calibrated using the acquired 2-D MFD measurements (with rotating rotor and fixed sensors) and the sensor calibration process for S_p can be summarized in the following steps based on the above-mentioned assumptions and observations.

A. Calibration of measuring point positions

Since the local extremes in the normal component of MFDs reveals the positions of PM centers, the local extremes of B_R (normal component) in measured 2-D MFD from S_p reveals that the measuring point of S_p aligns with one PM center after the rotation where the rotational angles correspond to the indices of local extremes of B_R in the 2-D data sets. For the local extremes in B_R that corresponds to the i^{th} PM (PM_i), we have:

$$[\mathbf{A}_i]\mathbf{X} = \mathbf{Y}_i \tag{5.8a}$$

where
$$[\mathbf{A}_i]=\begin{bmatrix} C_{\gamma i}C_{\beta i} & S_{\gamma i}C_{\alpha i}+C_{\gamma i}S_{\beta i}S_{\alpha i} & S_{\gamma i}S_{\alpha i}-C_{\gamma i}S_{\beta i}C_{\alpha i} \\ -S_{\gamma i}C_{\beta i} & C_{\gamma i}C_{\alpha i}-S_{\gamma i}S_{\beta i}S_{\alpha i} & C_{\gamma i}S_{\alpha i}+S_{\gamma i}S_{\beta i}C_{\alpha i} \\ S_{\beta i} & -C_{\beta i}S_{\alpha i} & C_{\beta i}C_{\alpha i} \end{bmatrix} \tag{5.8b}$$

$$\mathbf{X}=\begin{bmatrix}\cos\Phi_p \sin\Theta_p & \sin\Phi_p \sin\Theta_p & \cos\Theta_p\end{bmatrix}^T \tag{5.8c}$$

$$\mathbf{Y}_i=\begin{bmatrix}\cos\phi_i \sin\theta_i & \sin\phi_i \sin\theta_i & \cos\theta_i\end{bmatrix}^T \tag{5.8d}$$

In (5.8a), $[\mathbf{A}_i]$ is the rotation matrix with Euler angles of $(\alpha_i,\beta_i,\gamma_i)$ corresponding to the indices at the local maxima in DS_I or DS_{II}; θ_i,ϕ_i are the spherical coordinates of PM_i in rotor frame (given in Table 4.1); and C and S represent cosine and sine respectively. The $\mathbf{X}$ containing the actual positions of the S_p sensor can be solved with pseudo-inverse with all PM centers by locating the local extremes:

$$\mathbf{X}=(\mathbf{A}^T\mathbf{A})\mathbf{A}^T\mathbf{Y} \tag{5.9a}$$

where
$$\mathbf{A}=\begin{bmatrix}\mathbf{A}_1\\ \vdots \\ \mathbf{A}_i \\ \vdots\end{bmatrix} \text{ and } \mathbf{Y}=\begin{bmatrix}\mathbf{Y}_1\\ \vdots \\ \mathbf{Y}_i \\ \vdots\end{bmatrix} \tag{5.9b}$$

The position of S_p can be obtained using:

$$\begin{bmatrix}\Theta_p\\ \Phi_p\end{bmatrix}=\begin{bmatrix}a\cos(X_3)\\ a\tan(X_2/X_1)\end{bmatrix} \tag{5.10}$$

where X_1 X_2 X_3 are the first, second and third components of $\mathbf{X}$.

B. Calibration of sensor orientation

For sensor calibration, the mid points of each line segment (denoted by the circles in Figure 5.7) are selected. It can be inferred that the tangential MFDs at the mid points on the horizontal line segments (HLS's) are along the direction of $\vec{e}_\phi$; and the tangential MFDs at the mid points on the vertical line segments (HLS's) are along the

direction of $\vec{e}_\theta$. For the mid-point (denoted by Q_k in the following discussion) of the k^{th} line segments, the tangential MFD with respect to the stator frame is:

$$\mathbf{B}_{t,k} = \begin{cases} B_{t,k} \cdot \left(\left[\mathbf{R}_k \right]^T \vec{e}_{\phi k} \right), & \text{for points on HLS} \\ B_{t,k} \cdot \left(\left[\mathbf{R}_k \right]^T \vec{e}_{\theta k} \right), & \text{for points on VLS} \end{cases} \tag{5.11a}$$

where $$[\mathbf{R}_k] = [Rot(\gamma_k)] \cdot [Rot(\beta_k)] \cdot [Rot(\alpha_k)] \tag{5.11b}$$

In (5.11), θ_k and ϕ_k are the spherical coordinates of Q_k in the rotor frame, which can be obtained by taking average location of two neighboring PMs of Q_k. The PM locations are given in Table 4.1. $(\alpha_k, \beta_k, \gamma_k)$ are the Euler angles corresponding to the indices of the mid points. Meanwhile, the tangential MFD measured by S_p at Q_k is:

$$\mathbf{B}_{t,k} = B_{\Theta k} \vec{e}_{\Theta p} + B_{\Phi k} \vec{e}_{\Phi p} \tag{5.12}$$

where $B_{\Theta k}$ and $B_{\Phi k}$ are the measured MFD components at Q_k. Substituting $\vec{e}_{\Theta k}$ and $\vec{e}_{\Phi k}$ with (5.7), and comparing the right-hand-sides of (5.11a) and (5.12), yields:

$$\left[\mathbf{AA}_k \right] \mathbf{XX} = \mathbf{YY}_k \tag{5.13a}$$

where $$\mathbf{AA}_k = \left[B_{\Theta k} \vec{e}'_{\Theta p} + B_{\Phi k} \vec{e}'_{\Phi p} \quad B_{\Theta k} \vec{e}'_{\Phi p} - B_{\Phi k} \vec{e}'_{\Theta p} \right] \tag{5.13b}$$

and $$\mathbf{YY}_k = \begin{cases} B_{t,k} \cdot \left(\left[\mathbf{R}_k \right]^T \vec{e}_{\phi k} \right), & \text{for points on HLS} \\ B_{t,k} \cdot \left(\left[\mathbf{R}_k \right]^T \vec{e}_{\theta k} \right), & \text{for points on VLS} \end{cases}, \tag{5.13c}$$

$$\mathbf{XX} = \left[\cos\tau_p \quad \sin\tau_p \right]^T \tag{5.13d}$$

$$B_{t,k} = \sqrt{B_{\Theta k}^2 + B_{\Phi k}^2} \tag{5.13e}$$

With the captured mid points, the vector **XX** including the unknowns can be solved using pseudo-inverse in the form:

$$\mathbf{XX} = (\mathbf{AA}^T \mathbf{AA}) \mathbf{AA}^T \mathbf{YY} \tag{5.14a}$$

where $$\mathbf{AA} = \begin{bmatrix} \mathbf{AA}_1 \\ \vdots \\ \mathbf{AA}_k \\ \vdots \end{bmatrix} \text{ and } \mathbf{YY} = \begin{bmatrix} \mathbf{YY}_1 \\ \vdots \\ \mathbf{YY}_k \\ \vdots \end{bmatrix} \tag{5.14b}$$

τ_p can be found using (5.15):

$$\tau_p = \tan^{-1}(XX_1 / XX_2) \tag{5.15}$$

where XX_1 and XX_2 are the first and second components of **XX**.

5.5 Experiment and Result Discussions

The 2-D MFD measurements are experimentally acquired by leading 2-DOF rotations on the PMSM rotor. The 2-D MFD measurements are first utilized to calibrate the sensor locations. With the calibrated sensor information, the 3-D calibration is conducted by extending the 2-D MFD measurements. The results are experimentally validated.

5.5.1 Experimental Setup

Figure 5.9 shows the experimental setup for acquiring the rotor MFDs of the PMSM presented in Figure 5.1. As shown in Figure 5.9, a shaft is secured with the rotor and two rotary guides each driven by a stepper motor lead the shaft and the rotor to rotate about X and Y axes. A third stepper motor is secured to the other end of the rotor shaft and leads the rotor to spin about z axis. On all three axes, pulleys and timing-belts (with a gear ratio of 10:1) were employed to enlarge the resolutions. The resolutions of each axis are given in Table 5.2. While the Euler angles of the rotor increment on each axis, the MFDs are recorded by the magnetic sensors as shown in Figure 5.2.

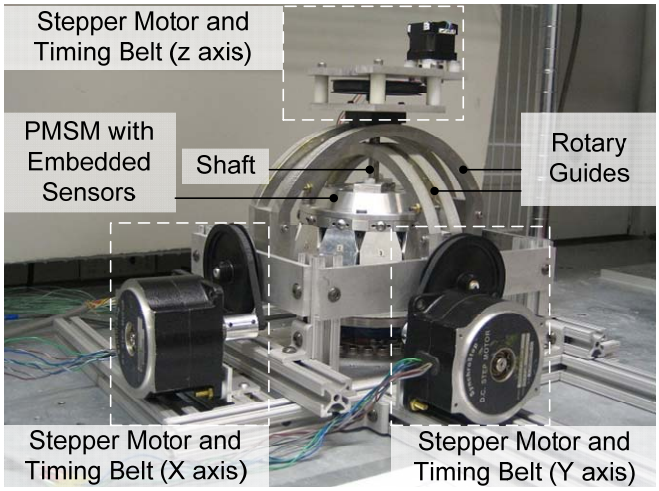

Figure 5.9 Setup for 3D Calibration

Table 5.2 Rotational resolutions

	X	Y	z
Resolution (deg/step)	0.54	0.54	0.18

5.5.2 Experimental Results and Discussion

Two sets of 2-DOF MFD data were acquired where the orientation in each case is characterized by:

Data Set I (DS_I): $\alpha = 0^\circ, -20.16^\circ \le \beta \le 20.16^\circ, 0^\circ \le \gamma \le 360^\circ$ (5.16a)

Data Set II (DS_{II}): $\beta = 0^\circ, -20.16^\circ \le \alpha \le 20.16^\circ, 0^\circ \le \gamma \le 360^\circ$ (5.16b)

Three MFD components are stored in terms of rotor orientation. For S_p, the MFDs are stored in the forms:

DS I: $B_{\Theta p} = B_{\Theta p}(\beta,\gamma), B_{\Phi p} = B_{\Phi p}(\beta,\gamma), B_{Rp} = B_{Rp}(\beta,\gamma)$ (5.17a)

DS II: $B_{\Theta p} = B_{\Theta p}(\alpha,\gamma), B_{\Phi p} = B_{\Phi p}(\alpha,\gamma), B_{Rp} = B_{Rp}(\alpha,\gamma)$ (5.17b)

As an illustration, Figure 5.10 shows the MFD components acquired by S_{17} in DS_I and the locations of S_{17} is calibrated below.

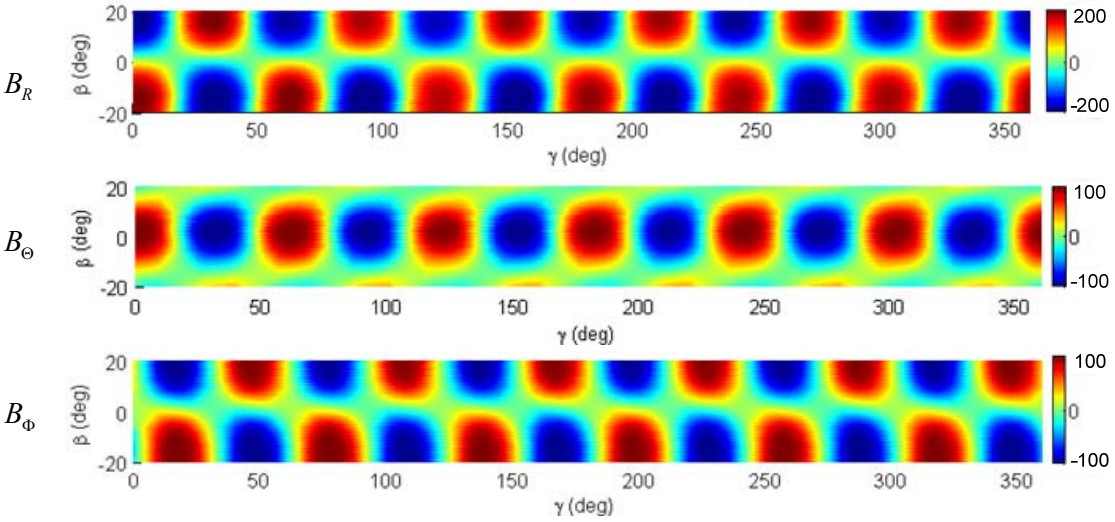

Figure 5.10 Acquired MFD of S_{17} (unit: mT)

A. Sensor Calibration

In order to find the actual position of S_{17}, the PM centers must be located based on the B_R component of the measurements. According to the observations from Figure 5.6, the PM centers can be found by locating the local extremes. However, in order to avoid the sensor noise and outliers in the acquired data, along with the fact that the B_R component of each PM dominate the neighboring area around its center, the contours are tracked in the small neighboring areas around each PM centers and the locations of the centers of the tracked contours are marked as the PM centers. Figure 5.11 shows the tracked contours in the measured B_R component of S_{17} (as shown in Figure 5.10). For clarification, a portion is zoomed.

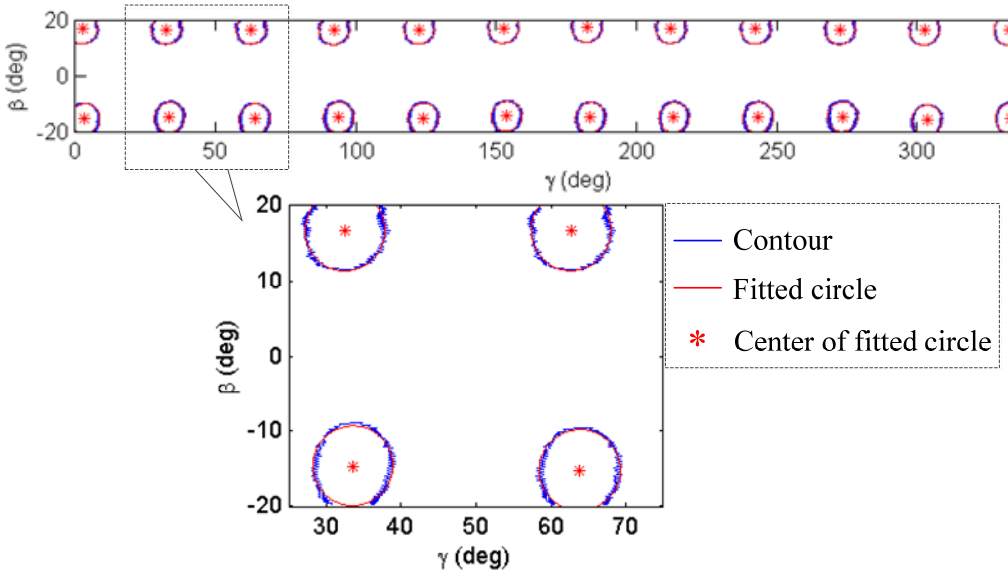

Figure 5.11 Located PM centers

As shown in Figure 5.11, the blue contours are composed of points with B_R equal to a threshold value. Due to the variation of the magnetization strength in each PM, the local extremes are not the same. Therefore, the threshold values are chosen to be 95% of the local extremes. Due to the fact the B_R component is axis-symmetric about each PM magnetization, each contour should form a circle. As shown in Figure 5.11, the red lines represent circles fitted with the points on each contour and the red points are the centers of the fitted circles. For each PM, the orientation (β,γ and $\alpha=0$ in this case) corresponding to the center approximated by locating the center of the fitted circle, as well as the spherical coordinate of this PM in the rotor frame (Figure 4.2) can be substituted into (5.8a) and the actual position of S_{17} can be solved using (5.9a) and (5.10).

When the orientations corresponding to each PM center are located, the orientations corresponding to the mid-point of two neighboring PM centers can be

also found (by averaging the index of neighboring PM centers). These values as well as the spherical coordinates of these center points in rotor frame (derived using the spherical coordinates of the PM centers given in Table 4.1) can be substituted into (5.13a) and the twist angle (τ_{17}) of S_{17} can then be solved with (5.14a) and (5.15). Similarly, the actual position and the twist angle of each sensor can be found with the same procedure and Table 5.3 summarizes the results. It is worth noting that it is only necessary to find the twist angles for three-axis sensors.

Table 5.3 Calibrated sensor information (unit: degrees)

Sensor Index	Measuring point position (desired ± discrepancy)						Twist angle
	Φ_p			Θ_p			τ_p
1	0	+	1.29	116	+	1.52	n/a
3	45	+	2.70	116	+	0.62	n/a
5	90	+	1.42	116	+	1.17	n/a
7	135	+	3.65	116	+	1.06	n/a
9	0	+	3.36	64	-	0.29	n/a
10	22.5	+	4.19	64	-	0.05	-4.19
11	45	+	3.73	64	+	1.21	n/a
12	67.5	+	0.21	64	-	1.51	-0.92
13	90	+	0.14	64	+	1.04	n/a
14	112.5	+	0.19	64	-	1.21	-3.99
15	135	+	2.21	64	-	0.17	n/a
16	157.5	+	1.79	64	-	3.13	2.90
17	0	+	2.93	90	+	0.99	-3.35
18	22.5	+	2.81	90	+	0.98	n/a
19	45	+	1.85	90	+	0.96	-5.18
20	67.5	+	1.33	90	+	1.23	n/a
21	90	+	1.08	90	+	1.23	2.11
22	112.5	+	0.02	90	+	1.16	n/a
23	135	+	2.91	90	-	0.37	-2.37
24	157.5	+	2.43	90	+	0.50	n/a

B. Conversion of acquired data into rotor frame

The acquired 2-D MFD measurements using the above setup are in terms of the Euler angles. However, the 3-D calibration (as shown in Figure 5.4) requires that the 2-D data is stored in terms of the spherical coordinates of the rotor frame (θ,ϕ). The transformation can be completed with the calibrated sensor information.

For any measured point in the acquired data sets, the spherical coordinates (θ,ϕ) of the rotor frame can be obtained by solving the equations:

$$\begin{bmatrix} \cos\phi\sin\theta \\ \sin\phi\sin\theta \\ \cos\theta \end{bmatrix} = [\mathbf{R}] \begin{bmatrix} \cos\Phi_p \sin\Theta_p \\ \sin\Phi_p \sin\Theta_p \\ \cos\Theta_p \end{bmatrix} \tag{5.18}$$

where the rotation matrix is defined in (5.3b) and the Euler angles correspond to the indices of the measured point. The normal and tangential components in terms of (θ,ϕ) can be obtained from the acquired measurements:

$$B_r(\theta,\phi) = B_{Rp}(\alpha,\beta,\gamma) \tag{5.19a}$$

$$\mathbf{B}_t(\theta,\phi) = B_{\Theta p}(\alpha,\beta,\gamma)\vec{e}_{\Theta p} + B_{\Phi p}(\alpha,\beta,\gamma)\vec{e}_{\Phi p} \tag{5.19b}$$

Since the tangential MFDs are with respect to the stator frame, the directional vectors of $\vec{e}_\theta$ and $\vec{e}_\phi$ can be transformed into the rotor frame and components along θ and ϕ directions can be obtained from dot products of the tangential MFD with the transformed directional vectors of $\vec{e}_\theta$ and $\vec{e}_\phi$ respectively:

$$B_\theta(\theta,\phi) = \mathbf{B}_t(\theta,\phi)\cdot\left([\mathbf{R}]\vec{e}_\theta\right) \tag{5.20a}$$

$$B_\phi(\theta,\phi) = \mathbf{B}_t(\theta,\phi)\cdot\left([\mathbf{R}]\vec{e}_\phi\right) \tag{5.20b}$$

Figure 5.12 graphs the MFDs with respect to the rotor frame transformed from the MFD measurements from S_{17} in DS_I.

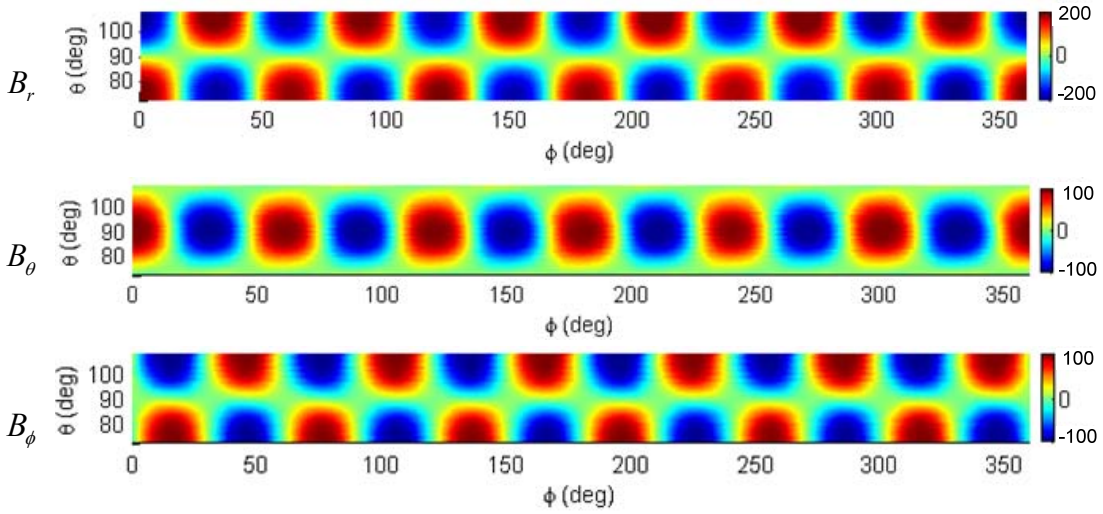

Figure 5.12 Rotor MFDs *w.r.t* rotor frame (unit: mT)

C. 3-D extension and simulation

Using the 3-D reconstruction method (Figure 5.4), the MFDs of S_{19} are computed as an illustration. The results are compared with experimental results where the rotor orientation follows the trajectory:

$$\alpha = 5.4^\circ, \beta = -5.4^\circ, 0^\circ \le \gamma \le 360^\circ \tag{5. 21}$$

Figure 5.13 compares the results obtained from the 3-D calibration and the experimental data. It can be seen that the results show excellent match in all components. The errors of MFD components are graphed in Figure 5.14. The percentage absolute mean errors (*PAME*s) of three components defined in the following are computed, which are 2.69%, 2.88%, 2.54% respectively.

$$PAME = \frac{mean(|Err|)}{\max(|X|)} \tag{5. 22}$$

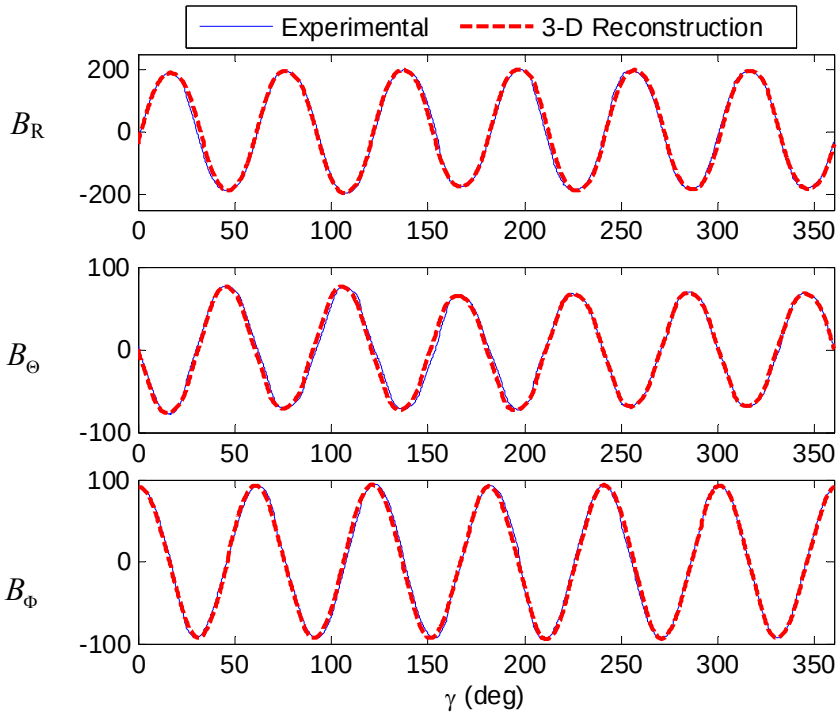

Figure 5.13 Experimental and calibration MFDs of S_{35} (unit: mT)

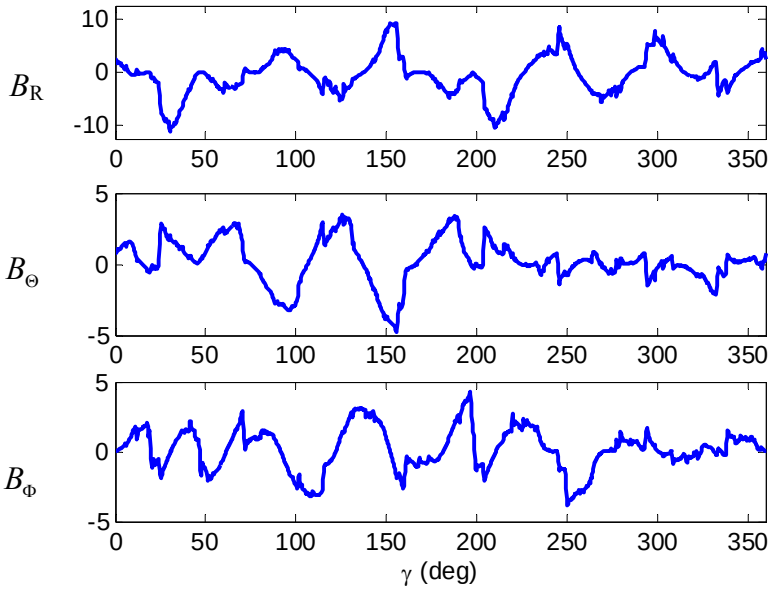

Figure 5.14 Error between experimental and calibration MFDs of S_{35} (unit: mT)

5.6 Conclusion

In this chapter, a new method for calibrating the 3-D rotor MFDs is presented. This method only requires 2-D measurement of the MFDs distributed on the rotor surface and 3-D rotor MFDs can be extended from the measured 2-D MFDs with calibrated sensor information. The sensor locations were also experimentally calibrated with the same 2-D MFD measurements. With the resolutions given in Table 5.2, each data set takes up a total of 225K samples while a 3-D data set acquired by rotations on all three axes at the same resolutions require 101M samples. This new method has greatly reduced the total number of sampling points required in a 3-D calibration and the calibration time as well as the accumulated error is dramatically reduced. The reconstructed 3-D MFDs were compared with experimental data and the results showed good match.

CHAPTER 6

EXPERIMENTAL RESULTS AND DISCUSSION

6.1 Overview

This chapter presents results of an experimental investigation based on a prototype DFC-based PMSM system. Two experiments were conducted; point-to-point response of the rotor orientation; and continuous motion of the rotor orientation to follow a trajectory. The control performances of the experiments are evaluated with a commercial gyroscope which operates independently of the control loop.

In order to isolate the MFDs of the rotor PMs, the MFDs generated by the energized EMs must be compensated. The relationship between the EM MFDs and the current inputs are studied and the parameters for compensating the EM MFDs in the DFD system as well as other un-modeled parameters are experimentally calibrated.

6.2 Experimental Setup and System Calibrations

This session begins with the description of control experiment setup along with its components, and is followed by the calibration of the parameters.

6.2.1 Experimental Setup

Figure 6.1 presents the experimental test-bed consisting of the PMSM, the embedded field-sensing system presented in Chapter 5, controller, current amplifiers and gyroscope (as a separate orientation sensing device for verification).

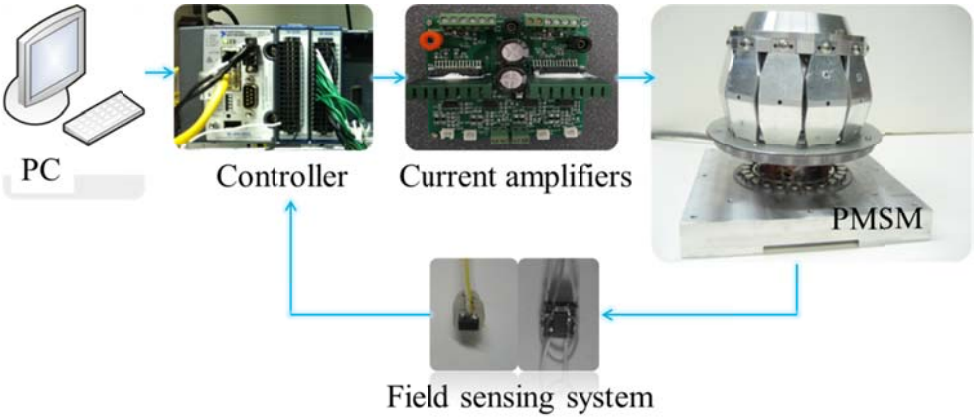

Figure 6.1 Experiment test-bed

A. PMSM with weight-compensating regulator

The rotor of the PMSM is essentially an inverted pendulum and becomes inherently unstable when no current input is supplied. A weight-compensating regulator (WCR) is incorporated in the PMSM as shown in Figure 6.2. The WCR consists of two circular PM rings (RI and RII as shown in Figure 6.2) arranged such that the rotor is supported angularly against gravity by distributed repulsive PM forces, which tend to maintain it at its equilibrium.

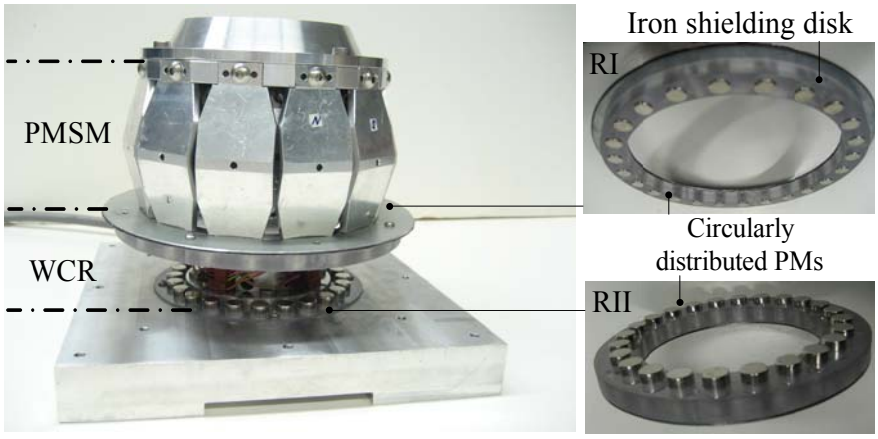

Figure 6.2 PMSM with WCR

B. Controller and I/O

The controller is featured with an NI-cRIO9025 (800MHz) processor, two NI-9205 A/D modules (32 channels, 16-bit resolution, $\pm 10V$ input range), and an NI-9264 D/A module (16 channels, 16-bit resolution, $\pm 10V$ output range). The control user interface was programmed using Labview FPGA, which allows communication between PC and the real-time processor.

C. Current amplifier

The current amplifiers transform voltage signals from the controller to currents as control inputs to the EMs of the PMSM. The linear current amplifiers (Figure 6.1) provide stable and smooth current amplification with ripple current less than 5mA; because of the low noise-to-signal ratio in the magnetic field readings, it has been chosen for this magnetic-field-based application. The on-board closed-loop circuit (PD control) allows fast and accurate current tracking. The voltage-to-current gain of each channel is 0.5A/V.

D. Orientation sensing device for verification

The DFC system does not require orientation feedback; for verification, a 3-axis gyroscope (ST LYPR540AH) is attached to the rotor for measuring the orientation. The gyroscope measures the angular velocity in terms of roll-pitch-yawl motion. The rotor orientation is obtained by integrating the angular velocity with a low-pass filter.

The specifications and parameters of the components are listed in Table 6.1.

Table 6.1 System parameters

PMSM	Rotor PMs: N52, D31.75mm x L6.35mm Stator EMs: D31.75mm x L9.525mm, core dia. 9.25mm, 775 turns Rotor mass: 1.99kg Rotor Inertia: $I_{xx} = I_{yy} = 6.26 \times 10^{-3} kg \cdot m^2, I_{zz} = 8.23 \times 10^{-3} kg \cdot m^2$		
WCR	PMs in RI: N42, D9.525mm x L9.525mm PMs in RII: N42, D9.525mm x L12.7mm		
Current amplifier	gain: 0.5A/V, maximum ripple current: 5mA, maximum current: 3A		
		Model #	Features
Controller	Processor A/D D/A	NI cRIO 9025 NI 9205 NI 9264	800MHz 32 channels, 16bits, $\pm 10V$ 16 channels, 16bits, $\pm 10V$
Sensor	Magnetic field sensor gyroscope	A1302 MLX91204 *ST LYPR540AH*	1-axis, sensitivity: 13V/T 3-axis, sensitivity: 25V/T 3-axis, sensitivity: 3.2mV/dps

6.2.2 Calibration of EM Magnetic Field

As the DFC system utilizes the MFDs of rotor PMs as feedback, the MFD of each EM must be subtracted off from the physically measured MFDs. Since the EMs and the sensors (installed on the stator) are stationary, the MFDs generated by an EM at the sensor locations are proportional to the supplied current. The PM MFDs at the p^{th} sensor (S_p) can be obtained by negating the EM MFDs from the total MFD measurements, which has the form:

$$B_p = B_{tol} - \sum_{j=1}^{N_E} c_{j,p} u_j \tag{6.1}$$

In (6.1), $c_{j,p}$ is a constant representing the ratio of MFD generated at S_p over the j^{th} current input. Note that the EMs are symmetrically placed about the motor center; each current input will energize two EMs which are connected in series. The correspondence of current input and the EM indices can be found in Table 4.2.

The constants *c*'s can be experimentally calibrated in the following process:

a) Record the MFDs of all sensors while incrementing the current input of an EM.

b) *c's* can be approximated by fitting the slopes of the current-MFD lines.

c) Repeat this process to each EM.

Figure 6.3(a) shows the MFDs measured by all sensors when the 9th current input (u_9 flowing into the 17th and 21th EMs) changes from -1A to 1A where the slopes (c's) are denoted in the figure. Figure 6.3 (b) is a plan view showing the positions of the EMs relative to the sensors (as well as the configurations) surrounding EM_{17}. It is worth noting that there are no sensors installed surrounding EM_{21}.

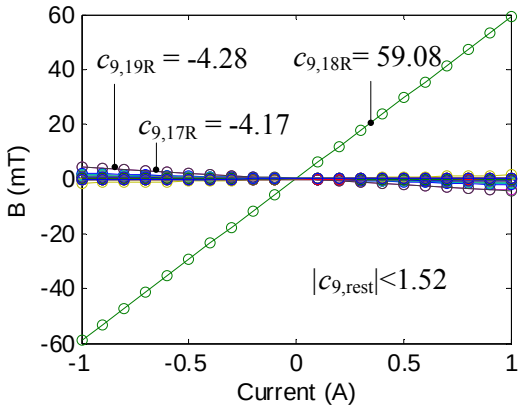

(a) Sensor measurements for u_9 from -1A to 1A (unit of the slopes: mT/A)

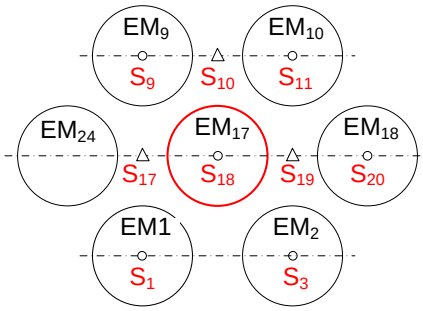

Δ: three-axis, o: single-axis

(b) Illustration of EM and sensor configurations

Figure 6.3 Effect of current in EM_1 on MFDs of all sensor points

Two observations can be summarized from Figure 6.3(a):

- The MFDs generated by the EMs only have effects on the sensors close to the energized EMs. When EM_{17} and EM_{21} are energized, the sensor measurements except for S_{17}, S_{18}, S_{19} (close to EM_{17}) have very small variations when the current input changes. The magnitudes of the other slopes are less than 3% of $c_{9,18R}$.

- The tangential MFDs (Θ and Φ components) generated by the EMs have very small effects on all sensor measurements when the current input changes. It can be seen from Figure 6.3(a) that $c_{9,18R}$ is much larger than the other slopes.

The calibration was conducted on each EM and Table 6.2 summarizes all calibrated c values. In the following control experiments, the constants c's with an absolute value smaller than 0.5 are neglected (treated as zeros) in order to reduce real-time computations.

Table 6.2 Calibrated values for constants c's (unit: mT/A)

Sensor	Current inputs (u_i)											
	1	2	3	4	5	6	7	8	9	10	11	12
1R	-56.46	-1.82	-0.41	-0.24	-0.10	-0.68	-0.54	-1.09	-1.40	-0.44	-0.59	-1.37
3R	1.42	59.29	1.01	0.22	0.39	0.90	0.52	0.34	-0.82	-0.80	0.50	0.21
5R	-0.24	-0.94	-56.30	-1.04	-0.33	-0.23	-0.14	-0.29	-0.39	-1.70	-1.25	-0.46
7R	0.17	0.31	1.37	55.54	-0.34	0.23	0.50	0.63	0.39	0.49	-0.75	1.66
9R	-0.05	-0.48	-0.45	0.30	-57.98	0.22	-0.79	-0.86	-1.57	-0.39	-0.24	-1.32
10Θ	0.12	-0.12	0.00	-0.04	0.11	-0.81	-0.07	-0.07	-1.19	-0.06	0.00	-0.08
10Φ	-0.04	-0.07	0.07	-0.12	-3.43	3.34	0.09	0.02	-0.22	-0.17	-0.06	0.13
10R	0.25	-0.09	0.10	0.19	6.46	5.95	0.27	0.04	-2.19	-0.27	0.07	-0.26
11R	-0.45	-0.97	-0.28	-0.21	0.36	-60.11	0.21	-0.33	-1.33	-1.25	-0.59	-0.38
12Θ	0.03	-0.11	0.09	-0.04	-0.03	0.31	0.12	-0.03	-0.08	-0.85	-0.06	-0.01
12Φ	-0.07	0.03	0.05	-0.06	-0.09	-3.11	3.46	0.12	0.15	-0.05	-0.16	0.06
12R	0.08	-0.06	0.20	0.01	0.24	5.92	6.34	0.25	-0.21	-1.65	-0.21	0.03
13R	-0.28	-0.40	-0.09	-0.31	-0.41	0.27	-57.40	-0.00	-0.57	-1.23	-1.22	-0.17
14Θ	0.02	-0.05	0.09	-0.10	-0.04	-0.03	0.25	-0.12	-0.01	-0.08	-0.87	0.06
14Φ	-0.09	0.06	-0.03	-0.05	-0.04	-0.08	-3.31	3.63	0.08	0.12	-0.05	0.14
14R	-0.13	0.04	0.23	-0.11	0.08	0.19	6.91	6.65	0.14	-0.23	-1.73	0.32
15R	-0.88	-0.39	-0.32	-0.52	-0.66	-0.30	-0.21	-57.79	-0.78	-0.40	-1.36	0.63
16Θ	-0.03	-0.02	0.04	-0.09	-0.10	-0.03	-0.01	0.19	0.07	0.00	-0.06	0.80
16Φ	-3.26	0.01	-0.09	0.01	-0.09	-0.10	-0.16	-2.86	0.08	0.02	0.06	0.02
16R	-6.50	0.10	0.05	-0.15	-0.14	-0.06	0.25	6.97	0.34	0.00	-0.32	1.88
17Θ	0.86	-0.06	0.02	-0.06	-0.78	-0.06	-0.03	-0.08	0.13	0.00	0.01	-0.05
17Φ	0.05	-0.12	0.05	-0.10	-0.07	0.09	0.03	0.07	-1.61	-0.07	-0.08	1.31
17R	2.19	-0.26	-0.04	0.21	2.20	0.22	-0.04	-0.34	-4.18	-0.13	0.08	-3.79
18R	1.32	-0.55	0.59	0.42	1.64	1.29	1.07	1.11	59.08	-0.08	0.36	-0.02
19Θ	0.86	-0.06	0.02	-0.06	-0.78	-0.06	-0.03	-0.08	0.13	0.00	0.01	-0.05
19Φ	0.05	-0.12	0.05	-0.10	-0.07	0.09	0.03	0.07	-1.61	-0.07	-0.08	1.31
19R	2.19	-0.26	-0.04	0.21	2.20	0.22	-0.04	-0.34	-4.18	-0.13	0.08	-3.79
20R	0.43	-0.43	2.24	0.61	0.45	1.22	1.56	0.57	-0.01	57.10	-0.07	0.74
21Θ	0.03	-0.08	0.96	-0.06	-0.02	-0.05	-0.89	-0.10	-0.01	-0.16	0.19	-0.01
21Φ	-0.06	0.09	0.11	-0.12	-0.05	-0.11	-0.05	0.11	0.08	1.43	-1.75	0.09
21R	-0.05	-0.32	2.18	-0.31	-0.02	0.17	2.29	0.26	-0.11	-3.88	-4.33	0.06
22R	0.53	0.74	1.39	-0.72	0.24	0.70	1.48	1.45	0.35	-0.11	57.99	0.77
23Θ	0.06	-0.03	0.06	-0.76	-0.10	-0.03	-0.09	-0.91	-0.01	-0.01	-0.12	0.24
23Φ	-0.08	0.08	-0.09	0.10	-0.09	-0.03	-0.10	-0.00	0.08	0.09	1.48	1.36
23R	-0.30	-0.03	0.27	-1.92	-0.27	-0.03	0.33	2.70	0.12	-0.10	-4.21	3.92
24R	-1.27	-0.28	-0.61	-1.47	-1.30	-0.39	-0.32	0.63	0.12	-0.53	-0.70	-57.52

6.2.3 Restoring Torque Calibration of the WCR

Figure 6.4(a) shows the experimental setup for calibrating the restoring torque of the WCR (generated by repulsive forces of the PMs), where a sliding block is placed on a beam attached to the rotor. An alignment pin passing through rotor diameter and the motor center enables that the rotor can only incline in the XZ plane.

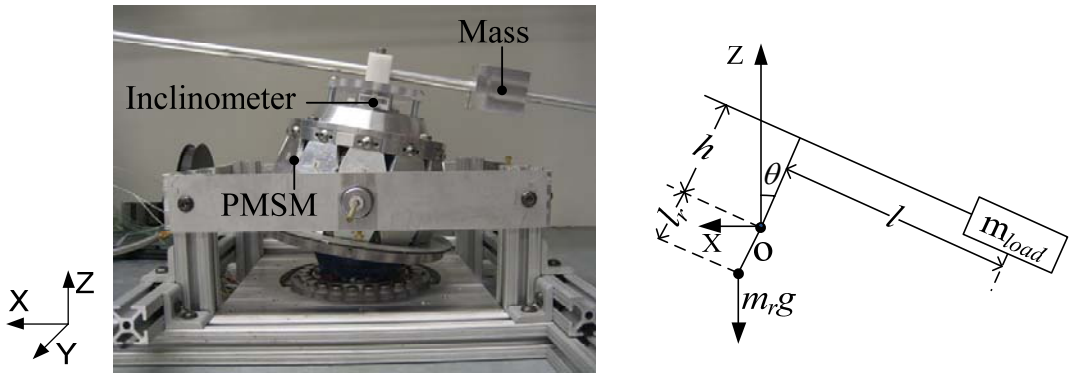

(a) Experimental setup (b) Schematic

Figure 6.4 Experimental setup for torque calibration of WCR

The schematic Figure 6.4(b) illustrates the calibration procedure, which neglects the bearing friction. The restoring torque equals to the gravitational torque of the sliding block at each equilibrium:

$$T(\theta) = m_r g l_r \cos\theta + m_{load} g (l\cos\theta + h\sin\theta) \tag{6.2}$$

In (6.2), m_r and m_{load} are the masses of the rotor and the sliding block respectively; l_r is the distance from the rotor mass-center to the motor center. The length l from the center of the sliding block to the center of the beam and the inclination angle θ measured by an inclinometer at each equilibrium are recorded. Computed using (6.2), Figure 6.5 presents the results of the restoring torque as a function of θ. The

parameters used in the experiment are summarized in Table 6.3. It can be seen that the restoring torque increases as the inclination angle increments and the restoring torque is zero at $\theta = 0$. As a result, the rotor tends to maintain at its equilibrium position ($\theta = 0$) when there is no external torque and all the EMs are not energized.

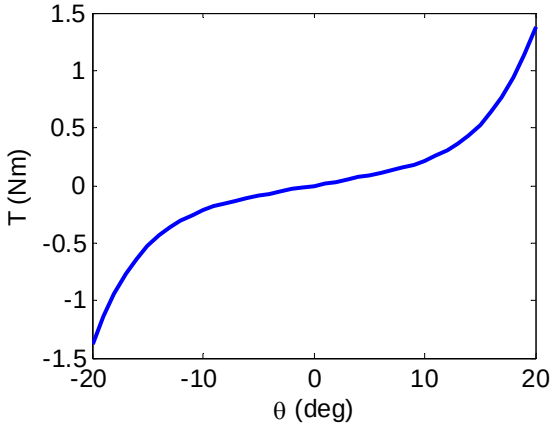

Figure 6.5 Restoring torque of the WCR

Table 6.3 Experiment parameters

m_r = 2.02kg, m_{load} = 158.8g, h = 107mm, l_r = 9.23mm

6.3 Experiment and Result Discussions

With the numerical analysis of the DFC system presented in Chapter 4, the DFC system is implemented on the PMSM test-bed. The control performance of the DFC system is evaluated for both step response and trajectory tracking of the rotor orientation. Since the initial and final states as well as the intermediate states are within one bijective domain in the step response, the controlled MFD vector is consistently composed of same measurements. For the trajectory tracking

experiment, the controlled MFD vector switches from two different MFD vectors and the states go through three different domains.

For both experiments, the rotor orientations are measured by the gyroscope for verification. The DFC system and acquisition system of the gyroscope operate independently; the sampling times are compared in Table 6.4. Note that the sampling time of gyroscope is purely used for orientation estimation while the sampling time of the DFC system corresponds to the time consumed for the closed loop.

Table 6.4 Comparison of sampling times

	DFC system	Gyroscope
Sampling time	4ms	12ms

6.3.1 Step Response

The PMSM is commanded from the initial orientation $(0^\circ, 0^\circ, 0^\circ)$ to the state $(-0.6^\circ, 0.5^\circ, -1^\circ)$. Since initial and final states are within same bijective domain, the controlled MFD vector is set to be:

$$\mathbf{B_S} = [B_{13R}, B_{9R}, B_{11R}] \tag{6.3}$$

The desired MFDs corresponding to the initial and final orientations are obtained through the 3-D calibration process presented in Chapter 5 and illustrated in Figure 5.4. The PID gain matrices used in this experiment are:

$$\mathbf{K}_p = \begin{bmatrix} -4 & 0 & 0 \\ 0 & -2.5 & 0 \\ 0 & 0 & -8 \end{bmatrix}, \ \mathbf{K}_I = 0.025\mathbf{K}_P, \ \mathbf{K}_D = 24\mathbf{K}_P \tag{6.4}$$

Figure 6.6 shows the MFD responses of the components of the controlled MFD vector when the command changes at 0.1s. It can be seen that the system is stable and the components of controlled MFD vector converge to the desired values in less than 1sec. Figure 6.7 shows the responses of Euler angles acquired by the gyroscope. It can be seen that as the components of the controlled MFD vector converges to the desired values, the Euler angles also converge to the desired orientation. The parameters characterizing the performances of the results graphed in Figure 6.7 are summarized in Table 6.5.

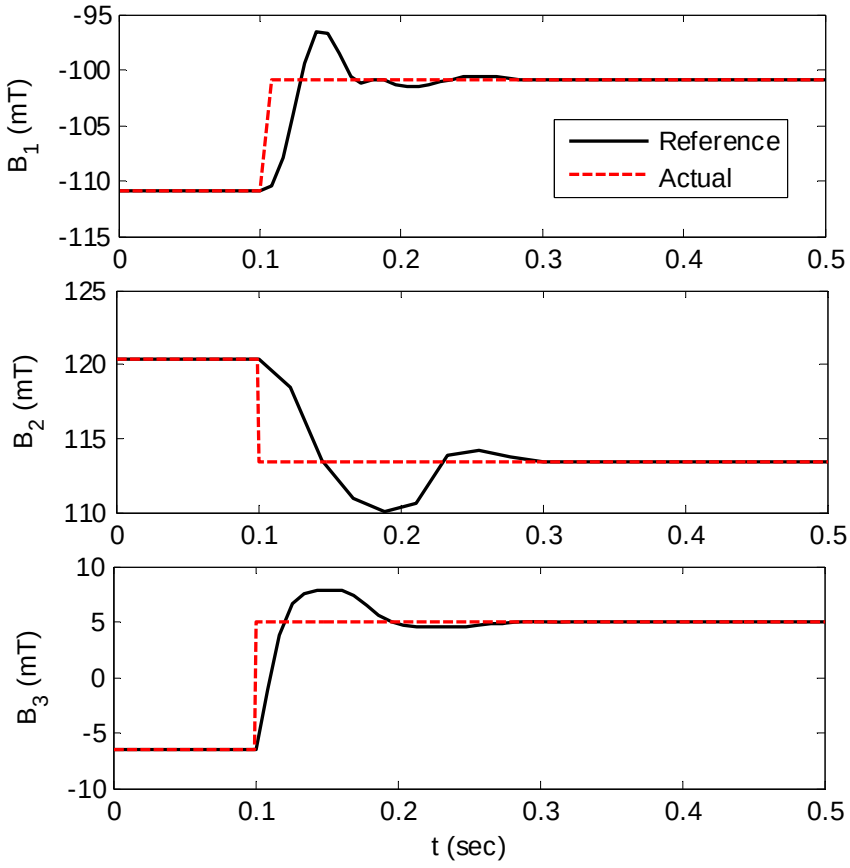

Figure 6.6 Step response of MFD ($\mathbf{B_S} = [B_{13R}, B_{9R}, B_{11R}]$)

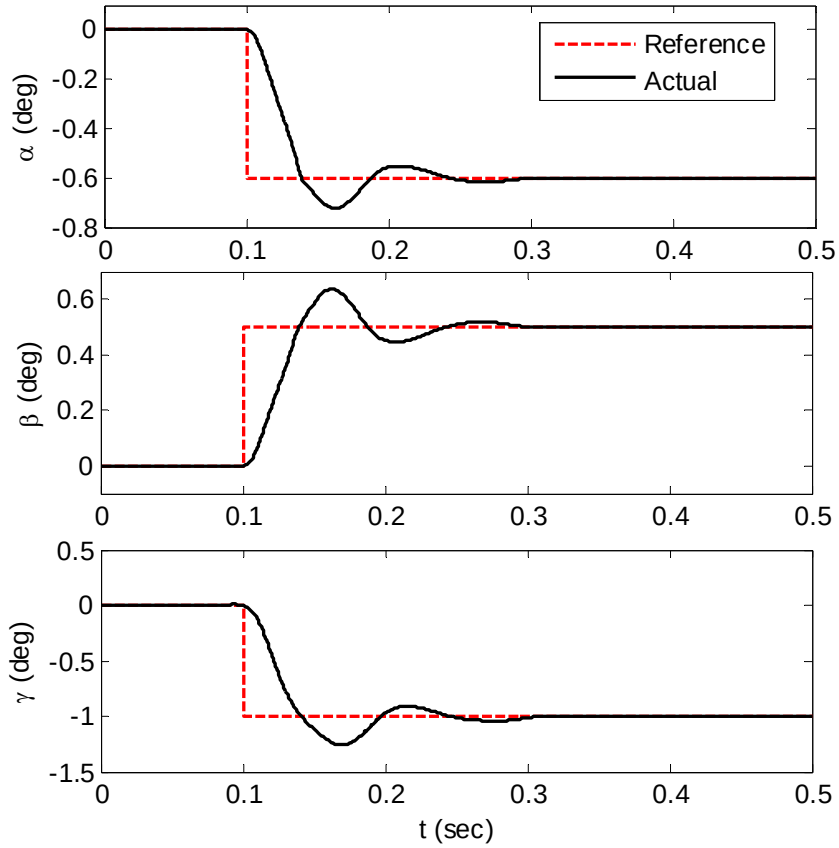

Figure 6.7 Step responses of Euler angles

Table 6.5 Step response parameters

Euler angle	Overshoot (deg)	Settling time (sec)	Static error (deg)
α	0.12	0.18	0.002
β	0.13	0.19	0.006
γ	0.26	0.18	0.009

6.3.2 Trajectory Tracking Application

In this experiment, the PMSM is commanded to continuously track a series of desired orientations which guides the end effector (laser pointer fixed to the rotor) to track a trajectory. As shown in Figure 6.8(a), the laser pointer is fixed to the rotor and where the gyroscope is also attached to record the orientation for verification. Figure

6.8(b) illustrates the schematic of the experimental setup, where the laser beam projects a point (**P**) on the planar screen. A camera is placed on the other side of the screen to capture the projection trajectory. The desired trajectory is a closed semi-circle (semi-circular arc and diameter) on the planar screen.

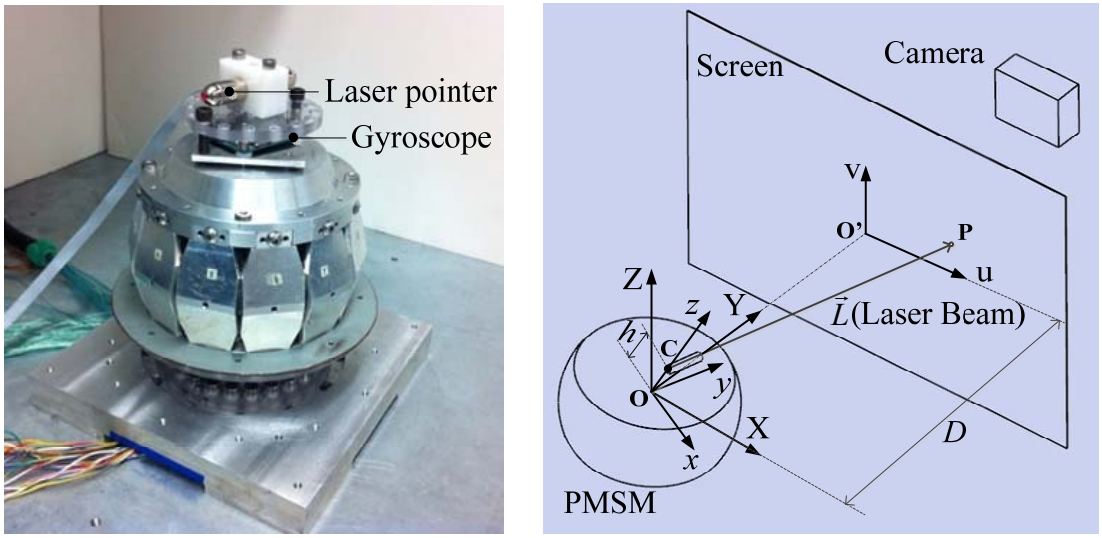

(a) PMSM with laser pointer and gyroscope

(b) Schematic of the experiment setup

Figure 6.8 Experiment setup

In Figure 6.8 (b), the XYZ and xyz denote the stator and rotor coordinate frames. uv is a 2D coordinate of the screen plane. The XZ plane, screen plane and the camera sensor plane are parallel; the line connecting the rotor center and the origin of the uv coordinate is perpendicular to all three planes; D is the distance between the screen and the XZ plane; the laser beam is parallel to the y axis of the rotor frame; and h is the distance from **O** to **C** (interception of the laser beam and z axis).

For any point (X,Y,Z) with respect to the stator frame, the line equation of the laser beam (which passes the **C** and is parallel to y axis) has the form:

$$\frac{X - hS_\beta}{-S_\gamma C_\beta} = \frac{Y + hC_\beta S_\alpha}{C_\gamma C_\alpha - S_\gamma S_\beta S_\alpha} = \frac{Z - hC_\beta C_\alpha}{C_\gamma S_\alpha + S_\gamma S_\beta S_\alpha} \tag{6.5}$$

where α,β,γ are the Euler angles and S and C represent sine and cosine respectively. The projection which is the interception of the laser beam and the screen can be found by substituting the equation of the screen ($Y = D$) to (6.5), which have the form:

$$\begin{cases} X = -\dfrac{(D + hC_\beta S_\alpha)S_\gamma C_\beta}{C_\gamma C_\alpha - S_\gamma S_\beta S_\alpha} + hS_\beta \\ Y = D \\ Z = \dfrac{(D + hC_\beta S_\alpha)(C_\gamma S_\alpha + S_\gamma S_\beta S_\alpha)}{C_\gamma C_\alpha - S_\gamma S_\beta S_\alpha} + hC_\beta C_\alpha \end{cases} \tag{6.6}$$

The coordinate of **P** can be transformed from the stator frame to the screen frame:

$$\begin{cases} u = X = -\dfrac{(D + hC_\beta S_\alpha)S_\gamma C_\beta}{C_\gamma C_\alpha - S_\gamma S_\beta S_\alpha} + hS_\beta \\ v = Z = \dfrac{(D + hC_\beta S_\alpha)(C_\gamma S_\alpha + S_\gamma S_\beta S_\alpha)}{C_\gamma C_\alpha - S_\gamma S_\beta S_\alpha} + hC_\beta C_\alpha \end{cases} \tag{6.7}$$

The objective is to lead the laser beam to track a closed semi-circle starting from the origin which is the projection of the laser beam on the screen when the rotor orientation is (0, 0, 0). The origin on the screen is located at

$$(u, v) = (0, h) \tag{6.8}$$

The desired trajectory illustrated in Figure 6.9 can be divided into three trajectory sections (TS I, TS II and TS III), which can be defined in parametric form as shown in Figure 6.9. Substituting the coordinates of trajectory obtained from Figure 6.9 into (6.7), the desired rotor orientations can be solved. As the rotor orientation has 3-DOF while the trajectory is defined with 2-DOF, the unique solutions can be obtained in this experiment with a constraint $\beta = 0$.

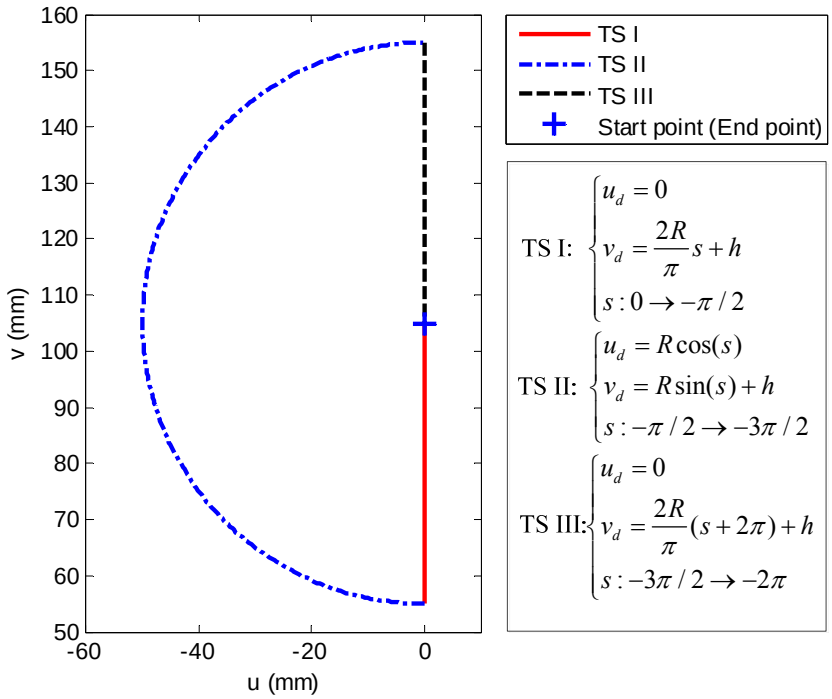

Figure 6.9 Illustration of desired trajectory (R=50mm, $s = \omega t$, ω is the speed)

The desired MFDs corresponding to the desired orientations can be acquired by following the steps shown in Figure 5.4. Throughout the entire trajectory, the controlled MFD vector switches from two MFD vectors as shown in (4.10) and three different MFD-defined domains. The MFD-defined domains as well as the switching criteria (or boundary conditions) are shown in Figure 4.9. The PID gain matrices in each MFD-defined domain are:

$$\Omega_{SI+}: \quad \mathbf{K}_P = \begin{bmatrix} 2 & 0 & 0 \\ 0 & -0.8 & 0 \\ 0 & 0 & 1.6 \end{bmatrix}, \ \mathbf{K}_I = \begin{bmatrix} 0.033 & 0 & 0 \\ 0 & -0.02 & 0 \\ 0 & 0 & 0.04 \end{bmatrix}, \ \mathbf{K}_D = \begin{bmatrix} 60 & 0 & 0 \\ 0 & -27 & 0 \\ 0 & 0 & 84 \end{bmatrix}$$

$$\Omega_{SI-}: \quad \mathbf{K}_P = \begin{bmatrix} 2 & 0 & 0 \\ 0 & -0.8 & 0 \\ 0 & 0 & -1.6 \end{bmatrix}, \ \mathbf{K}_I = \begin{bmatrix} 0.033 & 0 & 0 \\ 0 & -0.02 & 0 \\ 0 & 0 & -0.04 \end{bmatrix}, \ \mathbf{K}_D = \begin{bmatrix} 60 & 0 & 0 \\ 0 & -27 & 0 \\ 0 & 0 & -84 \end{bmatrix}$$

$$\Omega_{SII}: \quad \mathbf{K}_P = \begin{bmatrix} -2 & 0 & 0 \\ 0 & -1 & 0 \\ 0 & 0 & -2 \end{bmatrix}, \ \mathbf{K}_I = \begin{bmatrix} -0.006 & 0 & 0 \\ 0 & -0.03 & 0 \\ 0 & 0 & -0.05 \end{bmatrix}, \ \mathbf{K}_D = \begin{bmatrix} -66 & 0 & 0 \\ 0 & -22.5 & 0 \\ 0 & 0 & -54 \end{bmatrix}$$

The parameters used in this experiment are summarized in Table 6.6.

Figure 6.10 compares the components of the reference and the actual controlled MFD vector where the switching sequence is denoted by the color bars. It can be seen that the controlled variables track the reference MFD components closely. Figure 6.11 shows the transient response in the dashed box graphed in Figure 6.10. It can be seen that there is a time delay of about 12ms in the actual response.

Table 6.6 Experiment parameters

D = 537mm, h = 105mm, ω = 0.25rad/s

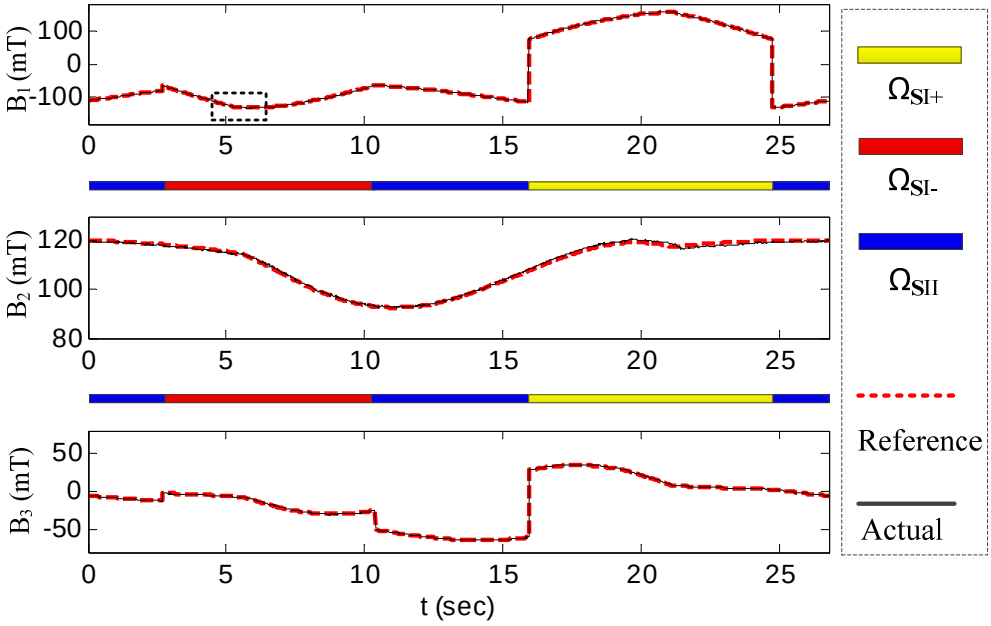

Figure 6.10 MFD response

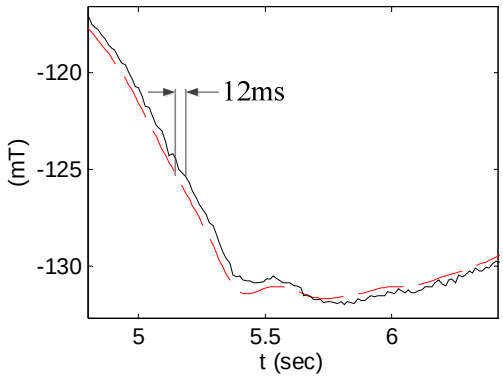

Figure 6.11 Time delay in MFD response

The desired Euler angles and the actual Euler angles (measured by the gyroscope) for the entire trajectory are compared in Figure 6.12. It can be seen that the rotor follows the desired orientations closely. The switching sequence (color bar) is superimposed in Figure 6.12 and it can be seen that there is no oscillation when the switching happens. The errors of the Euler angles are shown in Figure 6.13 and the maximum and mean absolute errors are summarized in Table 6.7. The current inputs are shown in Figure 6.14 and it can be seen that the maximum current is less than 0.5A.

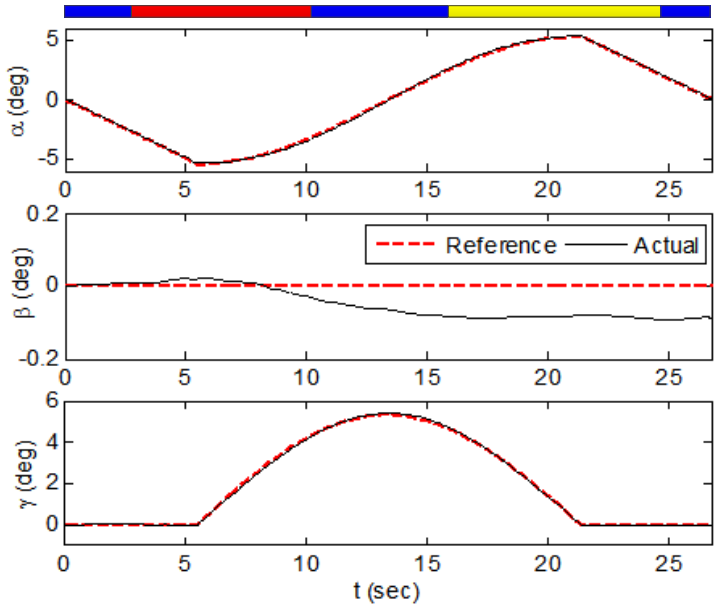

Figure 6.12 Orientation response

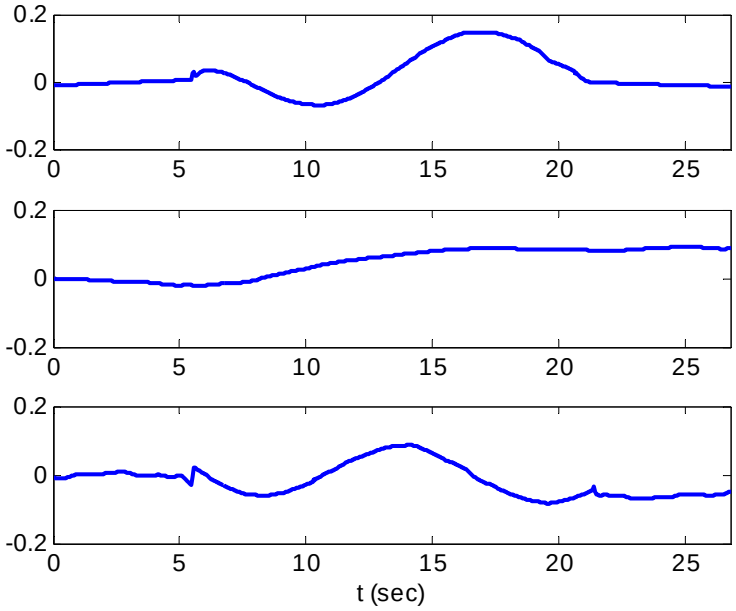

Figure 6.13 Orientation errors of α, β, γ (unit: deg)

Table 6.7 Tracking errors

	Maximum absolute error	Mean absolute error
α (deg)	0.1465	0.0412
β (deg)	0.0925	0.0529
γ (deg)	0.0877	0.0422
$Err_{projection}$ (mm)	0.88	0.32

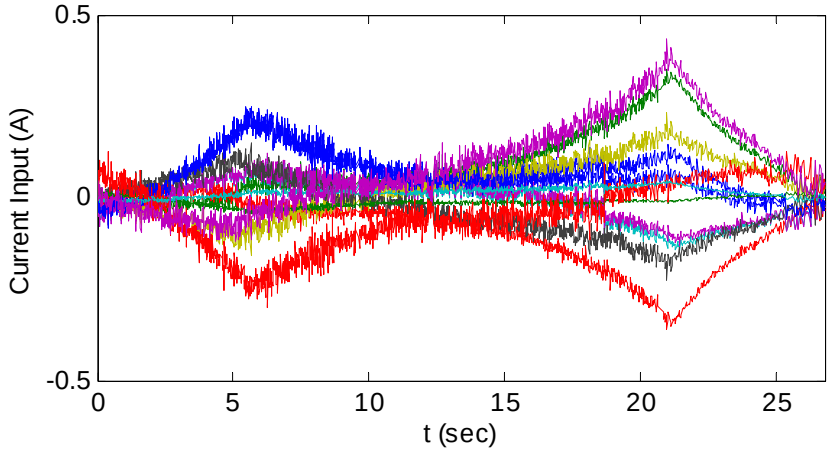

Figure 6.14 Current inputs

The projection of the laser beam on the screen was captured by the camera and the coordinates were approximated by locating the centroids of the bright spots in the binarized images of the captured frames. Figure 6.15 compares the desired trajectory and the trajectory of the captured projection on the screen. It can be seen that the trajectory formed by the projection of the laser beam match the desired trajectory very well. The maximum and mean absolute errors of the projection trajectory are also summarized in Table 6.7, where the error in each trajectory section is defined as:

$$Err_{projection} = \begin{cases} u_d - u, & TS\ I \\ R - \sqrt{u^2 + (v-h)^2}, & TS\ II \\ u_d - u, & TS\ III \end{cases} \tag{6.9}$$

where u_d can be found in Figure 6.9.

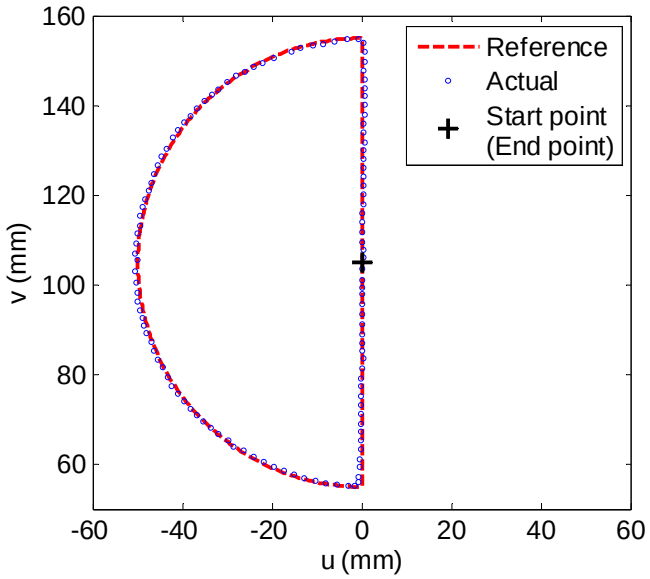

Figure 6.15 Desired trajectory and the actual projection on the screen

6.4 Conclusion

The control performances of the step response as well as the trajectory tracking of the DFC system were experimentally investigated on the PMSM test-bed. The DFC system enables rapid and accurate response of the rotor orientation of the PMSM. The multi-sensor network enables the DFC system to apply in regions larger than individual bijective domains. Also, results show that the DFC system can transit seamlessly in different domains. A comparison of the sampling times of the closed-loop DFC system and the gyroscope (for only orientation estimation) implies that the DFC system is superior in terms of the computational efficiency to traditional control systems that require orientation feedback.

CHAPTER 7

CONCLUSION AND FUTURE WORKS

7.1 Accomplishments and Contributions

While the immediate contribution of this thesis is a new method for closed-loop orientation control of multi-DOF PMSMs, the results and other new methods derived in this research have potential applications in many other electromagnetic motion systems. The specific contributions include the following:

A. More efficient control method

The DFC method eliminates the need of explicit orientation feedback. For a multi-DOF system, external orientation systems usually introduce unwanted friction and/or inertia, which lead to low sampling rate in conventional PMSM control systems. The magnetic field measurements are much less demanding for both hardware and software; and the direct feedback of magnetic field measurements in closed-loop control greatly improves the computational efficiency. By allowing parallel processing of the control law and TCV estimation, this new control method further reduces the system sampling rate and accumulated errors due to the serial computations in conventional control systems, which dramatically improves system stability and accuracy. This new method provides a novel perspective for control which allows complete independence between sensing and control, not only in the real-time operation but also during design process.

B. Analytical method for determining the bijective relationship between orientation and magnetic field

The bijection between orientation and magnetic field has been discussed. The Jacobian provides an analytical and straight-forward way for studies concerning the magnetic inverse problems [52, 53]. This method is of great importance in locating the bijective domains of certain sensor sets in design process of the DFC system. Potentially, it will also have profound effects for the development of field-based orientation sensing systems of PMSMs. As multiple positions/orientations share a common field measurement value in a non-bijective relationship, it is clear that without bijection, associating an arbitrary field measurement with a unique position is difficult. Previous studies about field-based orientation sensing methods usually utilize sensor redundancy to ensure bijection leading to excessive sensor installations, signal acquisition, and processing channels. By analyzing the bijective domains of sensors installed at different locations with Jacobian in the design process, the unnecessary sensor installations can be greatly avoided to a large extent.

C. Force/Torque related estimation based on magnetic field

This thesis also offers a direct TCV estimation method using magnetic field measurements. Analytically, the TCV of an EM can be computed by integrating functions of the magnetic fields enclosing the EM, which is however not practical for real-time system because large amount of computation is needed. Orientation-based estimation methods have been developed and applied in many PMSM studies but these methods require explicit orientation information in control. This thesis

introduced a new method which avoids the above difficulties in TCV estimation by building direct mappings from magnetic field measurements of scattered measuring points to the TCVs. The ANN provides a proficient and relatively accurate mapping method and an efficient algorithm for real-time computation. This method not only provides immediate means for parallel processing of control law and TCV estimation in a DFC system, but also shows the feasibility of field-based force/torque estimation as an alternative of force/torque sensors in a variety of motion systems, such as traditional sing-axis motors, or linear and spherical motors.

7.2 Future Works

The studies in this thesis has extended the research of PMSMs in the aspects of control and sensing. The outcomes are encouraging and the future research works are summarized as follows:

A. Further improvements of the control system in accuracy and sampling rate.

The DFC method on the orientation control of a PMSM has overcome several limitations of traditional control methods that depend on explicit orientation sensing and serial computation. The performances of the DFC system can be further enriched in terms of the accuracy and bandwidth in three aspects:

- Optimization of a multi-sensor network: As the bijective domains depend on the sensor locations, it is desired to have an optimal multi-sensor network with a smallest number of sensors (each with a bijective domain corresponding to the maximum range), which enables the DFC to work in the entire operational range.

This will reduce computational time and associated signal processing, and thus hardware cost.

- Model-based TCV estimation: Although ANN is an efficient mapping method for TCV estimation using measured magnetic fields, the accuracy is hard to predict due to the lack of certainties in the intermediate process of ANN. It is desired that the TCV of an EM can be modeled in close-form as a function of some distributed field measurements on the EM such that the accuracy can be predicted and controlled by changing the number of distributed field measurements.
- Distributed hardware implementation of parallel processing. The DFC system introduced in Chapter 6 was implemented on a high performance processing unit. Even though the components permitting parallel computing (such as control law and TCV estimation) runs concurrently, the interferences are still obvious. An alternative and more efficient way is to implement the computations on relatively low-cost distributed processing units; For example, the ANN for the TCV estimation of each EM can be implemented on a DSP processor. The sampling rate will be further lowered and the system stability as well as accuracy can be improved.

B. Torque (force) estimation and control

Modern manufacturing industries nowadays require motors with not only high precision, but also with intelligence and adaptively. Many applications (like chip-mounter in MEMS industry) require torque (force) sensing and control in addition to position sensing and control. Current method for torque (force) sensing requires

expensive force and torque sensors, which not only needs modifications of the end effector but also affects the transient performances of the motion systems. As the external torque (force) applied by objects can be estimated using the exerting torque (force) of the motors and current states, and the exerting torque (force) depends on the TCVs and current inputs, it is possible estimate external torque (force) directly from magnetic field measurements. Meanwhile, as the output of the control law of the DFC system is torque, it is easy to apply torque constraints or commands in the control algorithms. The force control can be applied in a similar way.

C. PMSM for haptic applications [54]

Haptic or tele-operational devices, which have the capabilities to provide realistic force/tactile feedback to human operators in a virtual environment, play an increasingly important role in training stages in many fields. PMSMs which provide smooth and continuous multi-DOF motion in one joint have significant potentials in haptic applications. The continuous multi-DOF orientation allows flexible manipulation by human operator and the motion command can be converted to control object in target space for up to 6-DOF with an orientation-to-translation reconfiguration. As currents flow through the EMs, a 3-DOF torque can be generated providing "haptic feel" to the human user.

Physically, the PMSM has three-DOF of rotational motion but can be configured to operate in two modes to achieve two independent sets of (rotational and translational) motion in the target space (as shown in Figure 7.1):

Rotational mode: The PMSM can be directly used as an integrated rotational motion-sensor and torque-actuator. The three-DOF rotational motions are defined as:

$$\begin{bmatrix} \alpha' & \beta' & \gamma' \end{bmatrix}^{\mathrm{T}} = \begin{bmatrix} \varsigma_1\alpha & \varsigma_2\beta & \varsigma_3\gamma \end{bmatrix}^{\mathrm{T}} \tag{7.1}$$

where the constants, ζ_1, ζ_2 and ζ_3, can be tuned to meet specific needs; and the prime denotes the coordinates in virtual environment (similarly hereinafter). Similarly, the PMSM can simulate physically the torque feedback from the virtual target by directly applying Lorenz torques on its rotor in real time enabling the user to have the haptic feel. The three torque components have the form (with constant η_1, η_2 and η_3):

$$\begin{bmatrix} T_\alpha & T_\beta & T_\gamma \end{bmatrix}^{\mathrm{T}} = \begin{bmatrix} \eta_1 T_{\alpha'} & \eta_2 T_{\beta'} & \eta_3 T_{\gamma'} \end{bmatrix}^{\mathrm{T}} \tag{7.2}$$

Translational mode: The PMSM can also be configured in translational domain such that the user's rotational motion on the rotor is interpreted into translational displacements. By the same token, the force feedback from the virtual target is actuated as torques on the rotor enabling the user to have an equivalent haptic experience:

$$\begin{bmatrix} X' & Y' & Z' \end{bmatrix}^{\mathrm{T}} = \begin{bmatrix} \hat{\varsigma}_1\alpha & \hat{\varsigma}_2\beta & \hat{\varsigma}_3\gamma \end{bmatrix}^{\mathrm{T}} \tag{7.3a}$$

$$\begin{bmatrix} T_\alpha & T_\beta & T_\gamma \end{bmatrix}^{\mathrm{T}} = \begin{bmatrix} \hat{\eta}_1 F_{Y'} & \hat{\eta}_2 F_{X'} & \hat{\eta}_3 F_{Z'} \end{bmatrix}^{\mathrm{T}} \tag{7.3b}$$

where $\hat{\varsigma}_1, \hat{\varsigma}_2, \hat{\varsigma}_3$ and $\hat{\eta}_1, \hat{\eta}_2, \hat{\eta}_3$ are constants.

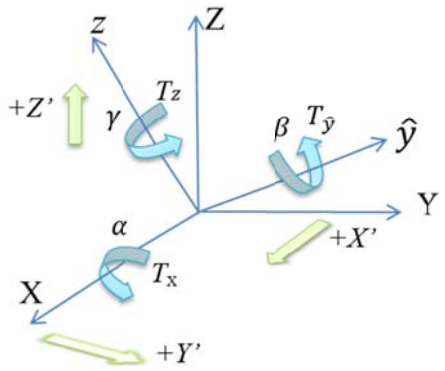

Figure 7.1 Illustration of position and torque commands for a two-mode configuration

By switching between these two modes, the PMSM is capable of two independent sets of three-DOF motions in the target space providing sensible force/torque feedback to the user in real time.

A two-mode PMSM haptic device will be able to cooperate with both virtual simulation environment (for training and design) and remote manipulation of real objects (tele-operation). The performances of the PMSM for both circumstances will be investigated.

APPENDIX A: DYNAMIC MODEL OF A PMSM

The dynamic model of a PMSM can be derived using Lagrange formulation.

For any orientation represented with *xyz* Euler angles (*α, β, γ*), the rotation matrix from XYZ to *xyz* (stator and rotor frames respectively as shown in Figure 4.2a) can be obtained as:

$$[\mathbf{R}] = [\mathbf{R}_\gamma][\mathbf{R}_\beta][\mathbf{R}_\alpha] = \begin{bmatrix} C_\gamma C_\beta & S_\gamma C_\alpha + C_\gamma S_\beta S_\alpha & S_\gamma S_\alpha - C_\gamma S_\beta C_\alpha \\ -S_\gamma C_\beta & C_\gamma C_\alpha - S_\gamma S_\beta S_\alpha & C_\gamma S_\alpha + S_\gamma S_\beta C_\alpha \\ S_\beta & -C_\beta S_\alpha & C_\beta C_\alpha \end{bmatrix} \tag{A.1a}$$

where $$[\mathbf{R}_\alpha] = \begin{bmatrix} 1 & 0 & 0 \\ 0 & C_\alpha & S_\alpha \\ 0 & -S_\alpha & C_\alpha \end{bmatrix}, [\mathbf{R}_\beta] = \begin{bmatrix} C_\beta & 0 & -S_\beta \\ 0 & 1 & 0 \\ S_\beta & 0 & C_\beta \end{bmatrix}, R_\gamma = \begin{bmatrix} C_\gamma & S_\gamma & 0 \\ -S_\gamma & C_\gamma & 0 \\ 0 & 0 & 1 \end{bmatrix} \tag{A.1b,c,d}$$

In (A.1), *S* and *C* represent sine and cosine respectively. The angular velocity of the rotor is

$$\vec{\omega} = \dot{\alpha}\vec{I} + \dot{\beta}\vec{J}' + \dot{\gamma}\vec{k} = \left(\dot{\alpha}C_\gamma C_\beta + \dot{\beta}S_\gamma\right)\vec{i} + \left(-\dot{\alpha}S_\gamma C_\beta + \dot{\beta}C_\gamma\right)\vec{j} + \left(\dot{\alpha}S_\beta + \dot{\gamma}\right)\vec{k} \tag{A.2}$$

where $(\vec{i}, \vec{j}, \vec{k})$, $(\vec{i}', \vec{j}', \vec{k}')$ and $(\vec{I}, \vec{J}, \vec{K})$ represent the unit vectors of the orthogonal axes of *xyz*, *x'y'z'* and XYZ frames (as shown in Figure 4.2a) respectively. The kinetic energy can be obtained as:

$$T_{KE} = \left(\frac{1}{2}\vec{\omega}^T I \vec{\omega}\right) = \frac{1}{2}\left(I_t\dot{\alpha}^2 C_\beta^2 + I_t\dot{\beta}^2 + I_a\dot{\alpha}^2 S_\beta^2 + I_a\dot{\gamma}^2 + 2I_a\dot{\alpha}\dot{\gamma}S_\beta\right) \tag{A.3}$$

where the inertia matrix

$$I = \begin{bmatrix} I_t & 0 & 0 \\ 0 & I_t & 0 \\ 0 & 0 & I_a \end{bmatrix} \tag{A.4(A.3)}$$

In (A.3), $I_a = I_{zz}$, $I_t = I_{xx}=I_{yy}$. The virtual displacement vector can be represented using:

$$\delta\vec{r} = \delta\alpha\vec{I} + \delta\beta\vec{j}' + \delta\gamma\vec{k} = \left(\delta\alpha C_\gamma C_\beta + \delta\beta S_\gamma\right)\vec{i} + \left(\delta\beta C_\gamma - \delta\alpha S_\gamma C_\beta\right)\vec{j} + \left(\delta\alpha S_\beta + \delta\gamma\right)\vec{k} \qquad \text{(A.5)}$$

Thus the generalized force can be derived using

$$\mathbf{Q} = \mathbf{T}\cdot\delta\vec{r} = \left(T_x C_\gamma C_\beta - T_y S_\gamma C_\beta + T_z S_\beta\right)\delta\alpha + \left(TS_\gamma + T_y C_\gamma\right)\delta\beta + T_z\delta\gamma \qquad \text{(A.6)}$$

where T_x, T_y, T_z are the components of the total torque applied by the EMs *w.r.t* the rotor frame.

Neglecting the frictional torque of the bearing, the Lagrange formulation has the form:

$$\frac{d}{dt}\left(\frac{\partial T}{\partial \dot{q}_i}\right) - \frac{\partial T}{\partial q_i} + \frac{\partial V}{\partial q_i} = Q_i \qquad \text{(A.7)}$$

In (A.7), the potential energy V=0 because the center of mass coincides with the rotation center; i = (1, 2, 3); (q_1, q_2, q_3) = (α, β, γ); and Q_1, Q_2, Q_3 are the coefficient terms of $\delta\alpha$, $\delta\beta$, $\delta\gamma$ in (A.6) respectively. Therefore, the equations of motion derived using (A.7) have the form:

$$[\mathbf{M}]\ddot{\mathbf{q}} + \mathbf{C}(\mathbf{q},\dot{\mathbf{q}})\dot{\mathbf{q}} + \mathbf{g}(\mathbf{q}) = \mathbf{T} \qquad \text{(A.8a)}$$

where

$$[\mathbf{M}] = \begin{bmatrix} I_t C_\beta^2 + I_a S_\beta^2 & 0 & I_a S_\beta \\ 0 & I_t & 0 \\ I_a S_\beta & 0 & I_a \end{bmatrix}, \qquad \text{(A.8b)}$$

$$\mathbf{C}(\mathbf{q},\dot{\mathbf{q}})\dot{\mathbf{q}} = \begin{bmatrix} 2I_a\dot{\alpha}\dot{\beta}S_\beta C_\beta + I_a\dot{\beta}\dot{\gamma}C_\beta - 2I_t\dot{\alpha}\dot{\beta}C_\beta S_\beta \\ I_t\dot{\alpha}^2 C_\beta S_\beta - I_a\dot{\alpha}^2 C_\beta S_\beta - I_a\dot{\alpha}\dot{\gamma}C_\beta \\ I_a\dot{\alpha}\dot{\beta}C_\beta \end{bmatrix} \qquad \text{(A.8c)}$$

and $$\mathbf{T} = \begin{bmatrix} C_\gamma C_\beta & -S_\gamma C_\beta & S_\beta \\ S_\gamma & C_\gamma & 0 \\ 0 & 0 & 1 \end{bmatrix} \begin{bmatrix} T_x \\ T_y \\ T_z \end{bmatrix} \quad \text{(A.8d)}$$

In (A.8a), $\mathbf{g}(\mathbf{q}) = 0$ (since center of mass coincides with the rotation center).

APPENDIX B: STABILITY ANALYSIS

For the rotor dynamic (A.8) and the PD control law, same as (2.18a),

$$\mathbf{T} = \mathbf{K}'_P \mathbf{e}_\mathbf{q} + \mathbf{K}'_D \dot{\mathbf{e}}_\mathbf{q} \tag{B.1}$$

let the Lyapunov function be the virtual mechanical energy having the form:

$$V = \frac{1}{2}\left(\mathbf{q}^T[\mathbf{M}]\dot{\mathbf{q}} + \mathbf{e}_\mathbf{q}^T[\mathbf{K}'_P]\mathbf{e}_\mathbf{q}\right) \tag{B.2}$$

Meanwhile, the conservation of energy can be written as

$$\frac{1}{2}\frac{d}{dt}\left(\dot{\mathbf{q}}^T[\mathbf{M}]\dot{\mathbf{q}}\right) = \dot{\mathbf{q}}^T \cdot \mathbf{T} \tag{B.3}$$

where the left hand side is the derivative of the kinetic energy; and the right hand side represents the power input of the motor. Since the inertia matrix [**M**] in (A.8) is symmetric positive definite, the time derivative of the Lyapunov function can be obtained, along with (B.3) and that, as:

$$\dot{V} = \frac{1}{2}\frac{d}{dt}\left(\dot{\mathbf{q}}^T[\mathbf{M}]\dot{\mathbf{q}}\right) + \frac{1}{2}\frac{d}{dt}\left(\mathbf{e}_\mathbf{q}^T[\mathbf{K}'_P]\mathbf{e}_\mathbf{q}\right) \tag{B.4}$$

Since $\dot{\mathbf{q}}_d = 0$ at the equilibrium state, substituting (B.1) and (B.3) into (B.4), yields:

$$\dot{V} = -\dot{\mathbf{q}}^T[\mathbf{K}'_D]\dot{\mathbf{q}} \tag{B.5}$$

Therefore, as long as the control matrices $\mathbf{K}'_P$ and $\mathbf{K}'_D$ in (B.1) are positive definite, $V > 0$, and $\dot{V} \le 0$. Meanwhile, since $\dot{V} = 0$ implies that $\dot{\mathbf{q}} = 0$; along with (A.8a), (B.1) and (B.3), $\dot{V}$ is identically 0 only if $\mathbf{e}_\mathbf{q} = 0$. Therefore, the system is stable and converges to the desired state.

REFERENCES

[1] J. K. Park, "Development of next generation microfactory systems," in *2nd International workshop on Microfactory Technology*, 2006, pp. 6-7.

[2] K.-M. Lee, H. Son, and K. Bai, "Design Concept and Analysis of a magnetically Levitated Multi-DOF Tiltable Stage for Micro Machining," in *International Conference on Micro-manufacturing*, 2007.

[3] K.-M. Lee, "Design criteria for developing an automated live-bird transfer system," *IEEE Trans. on Robotics and Automation,* vol. 17, pp. 483-490, 2001.

[4] M. Grebenstein, A. Albu-Sch¨affer, T. Bahls*, et al.*, "The DLR hand arm system," in *IEEE International Conference on Robotics and Automation (ICRA)*, 2011, pp. 3175-3182.

[5] K.-M. Lee and S. Arjunan, "A three-DOF micro-motion in-parallel actuated manipulator," *IEEE Trans. on Robotics and Automation,* vol. 7, pp. 634-641, 1991.

[6] J. Yoon and J. Ryu, "Design, fabrication and evaluation of a new haptic device using a parallel mechanism," *IEEE/ASME Trans. on Mechatronics,* vol. 6, pp. 211-233, 2001.

[7] B. Shchokin and F. Janabi-Sharifi, "Design and kinematic analysis of a rotary positioner," *Robotica,* vol. 25, pp. 75-84, 2005.

[8] F. C. Williams, E. R. Laithwaite, and J. F. Eastham, "Development and design of spherical induction motors," in *Proceedings of the IEE - Part A: Power Engineering*, 1959, pp. 471-484.

[9] K. Davey, G. Vachtsevanos, and R. Powers, "The analysis of fields and torques in spherical induction motors," *Magnetics, IEEE Transactions on,* vol. 23, pp. 273-282, 1987.

[10] G. Vachtsevanos, K. Davey, and K.-M. Lee, "Development of a novel intelligent robotic manipulator," *Control Systems Magazine, IEEE,* vol. 7, pp. 9-15, 1987.

[11] A. Foggia, E. Olivier, F. Chappuis*, et al.*, "A new three degrees of freedom electromagnetic actuator," in *Industry Applications Society Annual Meeting, 1988., Conference Record of the 1988 IEEE*, 1988, pp. 137-141 vol.1.

[12] R. L. Hollis, S. E. Salcudean, and A. P. Allan, "A six-degree-of-freedom magnetically levitated variable compliance fine motion wrist: Design, modeling and control," *IEEE Trans. on Robotics and Automation,* vol. 7, pp. 320-332, 1991.

[13] K. Kaneko, I. Yamada, and K. Itao, "A Spherical DC Servo Motor with Three Degrees of Freedom," *ASME, Dyn. Sys. And Control Div.,* pp. 398-402, 1988.

[14] K.-M. Lee, G. Vachtsevanos, and C. Kwan, "Development of a spherical stepper wrist motor," in *Robotics and Automation, 1988. Proceedings., 1988 IEEE International Conference on*, 1988, pp. 267-272 vol.1.

[15] K.-M. Lee and C. Kwan, "Design Concept Development of a Spherical Stepper for Robotic Applications," *IEEE Trans. on Robotics and Automation,* vol. 7, pp. 175-181, Feb 1991.

[16] Z. Zhou and K.-M. Lee, "Real-time motion control of a multi-degree-of-freedom variable reluctance spherical motor," in *Robotics and Automation, Proceedings., 1996 IEEE International Conference on*, 1996, pp. 2859 - 2864.

[17] K.-M. Lee, R. Sosseh, and Z. Wei, "Effects of the torque model on the control of a VR spherical motor," *Control Engineering Practice,* vol. 12, pp. 1437-1449, Nov 2004.

[18] T. Shigeki, G. Zhang, and M. Osamu, "Development of New Generation Spherical Ultrasonic Motor," in *1996 IEEE International Conf. on Robotics and Automation*, 1996, pp. 2871-2876.

[19] T. Amano, T. Ishii, K. Nakamura*, et al.*, "Ultrasonic actuator with multidegree of freedom using bending and longitudinal vibrations of a single stator," in *Proc. of the IEEE Ultrasonics Symposium*, 1998, pp. 667-670.

[20] G. S. Chirikjian and D. Stein, "Kinematic design and commutation of a spherical stepper motor," *IEEE/ASME Trans on Mechatronics,* vol. 4, pp. 342-353, 1999.

[21] K.-M. Lee, J. Pei, and R. Roth, "Kinematic Analysis of a Three Degree-of-Freedom Spherical Wrist Actuator," *Mechatronics,* vol. 4, pp. 581-605, Sep 1994.

[22] K.-M. Lee and H. Son, "Distributed multipole model for design of permanent-magnet-based actuators," *IEEE Transactions on Magnetics,* vol. 43, pp. 3904-3913, Oct 2007.

[23] H. Son and K.-M. Lee, "Open-loop Controller Design and Dynamic Characteristics of a Spherical Wheel Motor," *IEEE Trans. on Industrial Electronics,* vol. 57, pp. 3475-3482, 2010.

[24] J. Wang, G. W. Jewell, and D. Howe, "A novel spherical actuator: design and control," *Magnetics, IEEE Transactions on,* vol. 33, pp. 4209-4211, 1997.

[25] E. h. M. Week, T. Reinartza, G. Hennebergerb*, et al.*, "Design of a Spherical Motor with Three Degrees of Freedom," *CIRP Annals - Manufacturing Technology,* vol. 49, pp. 289-294, 2000.

[26] Y. Liang, I. M. Chen, L. Chee Kian*, et al.*, "Design and analysis of a permanent magnet spherical actuator," in *Intelligent Robots and Systems, 2005. (IROS 2005). 2005 IEEE/RSJ International Conference on*, 2005, pp. 691-696.

[27] C. Xia, P. Song, H. Li*, et al.*, "Research on Torque Calculation Method of Permanent-Magnet Spherical Motor Based on the Finite-Element Method," *Magnetics, IEEE Transactions on,* vol. 45, pp. 2015-2022, 2009.

[28] Z. Qian, Q. Wang, L. Ju*, et al.*, "Torque modeling and control algorithm of a permanent magnetic spherical motor," in *Electrical Machines and Systems, International Conference on* 2009, pp. 1-6.

[29] K.-M. Lee, R. Roth, and Z. Zhou, "Dynamic modeling and control of a ball-joint-like variable-reluctance spherical motor," *Journal of Dynamic Systems Measurement and Control,* vol. 118, pp. 29-40, Mar 1996.

[30] A. Cadena, "Design and construction of an Autonomous Underwater Vehicle for the launch of a small UAV," in *Technologies for Practical Robot Applications, IEEE International Conference on* 2009, pp. 78 - 83.

[31] K.-M. Lee and D. Zhou, "A real-time optical sensor for simultaneous measurement of three-DOF motions," *IEEE/ASME Transactions on Mechatronics,* vol. 9, pp. 499-507, 2004.

[32] H. Garner, M. Klement, and K.-M. Lee, "Design and Analysis of an Absolute Non-Contact Orientation Sensor for Wrist Motion Control," in *Proceedings of IEEE/ASME International Conference on Advanced Intelligent Mechatronics*, 2001, pp. 69-74.

[33] C. Hu, M. Q.-H. Meng, and M. Mandal, "A Linear Algorithm for Tracing Magnet Position and Orientation by Using Three-Axis Magnetic Sensors," *IEEE Transactions on Magnetics,* vol. 47, pp. 4096-4101, 2007.

[34] M. Tsai, C. Yang, M.-C. Tsai*, et al.*, "A flux-density-based electromagnetic servo system for real-time magnetic servoing/tracking," *IEEE/ASME Trans. on Mechatronics,* vol. 13, pp. 249-256, Apr 2008.

[35] K.-M. Lee and H. Son, "Equivalent voice-coil models for real-time computation in electromagnetic actuation and sensor applications," in

IEEE/ASME International Conference on Advanced Intelligent Mechatronics, Zurich, SWITZERLAND, 2007, pp. 1179-1184.

[36] S. Foong, K.-M. Lee, and K. Bai, "Magnetic Field-based Sensing Method for Spherical Joint," in *IEEE International Conference on Robotics and Automation (ICRA)*, Anchorage, AK, 2010, pp. 5447-5452.

[37] S. Foong, K.-M. Lee, and K. Bai, "Harnessing Embedded Magnetic Fields for Angular Sensing With Nanodegree Accuracy," *IEEE/ASME Transactions on Mechatronics,* vol. PP, pp. 1-10, 2011.

[38] W. Wang, J. Wang, G. Jewell*, et al.*, "Design and control of a novel spherical permanent magnet actuator with three degrees of freedom," *IEEE/ASME Transactions on Mechatronics,* vol. 8, pp. 457-468, Dec 2003.

[39] C. Xia, C. Guo, and T. Shi, "A Neural-Network-Identifier and Fuzzy-Controller-Based Algorithm for Dynamic Decoupling Control of Permanent-Magnet Spherical Motor," *Industrial Electronics, IEEE Transactions on,* vol. 57, pp. 2868 - 2878, 2010.

[40] Z. Li, "Robust Control of PM Spherical Stepper Motor Based on Neural Networks," *Industrial Electronics, IEEE Transactions on,* vol. 56, pp. 2945 - 2954, 2009.

[41] K.-M. Lee and H. Son, "Torque Model for Design and Control of a Spherical Wheel Motor," in *Proceedings of the 2005 IEEE/ASME International Conference on Advanced Intelligent Mechatronics*, 2005, pp. 335-340.

[42] Y. Liang, "Modeling and design of a three-degree-of-freedom permanent magnet spherical actuator," PHD Thesis, 2005.

[43] J. D. Jackson, *Classical Electrodynamics*: New York: Wiley, 1999.

[44] H. Son and K.-M. Lee, "Two-DOF magnetic orientation sensor using distributed multipole models for spherical wheel motor," *IEEE-ASME Transactions on Mechatronics,* vol. 21, pp. 156-165, Feb 2011.

[45] S. G. Krantz and H. R. Parks, *The Implicit Function Theorem: History, Theory, and Applications*, 1st ed.: Birkhäuser Boston, 2002.

[46] C. H. Edwards and D. E. Penney, *Multivariable Calculus*, 6 ed.: Prentice Hall, 2002.

[47] H. Son and K.-M. Lee, "Distributed multipole models for design and control of PM actuators and sensors," *IEEE-ASME Trans. on Mechatronics,* vol. 13, pp. 228-238, Apr 2008.

[48] K.-M. Lee, K. Bai, and J. Lim, "Dipole Models for Forward/Inverse Torque Computation of a Spherical Motor," *IEEE/ASME Transactions on Mechatronics,* vol. 14, pp. 46-54, Feb 2009.

[49] H. A. Haus and J. R. Melcher. Electromagnetic Fields and Energy [Online]. Available: http://web.mit.edu/6.013_book/www/book.html/chapter11

[50] N. I. J. P. A. Bastos. Forces in permanent magnets. Team workshop problems 23 [Online]. Available: http://www.compumag.co.uk/team.html [Online].

[51] Q. Li and K.-M. Lee, "An adaptive meshless method for magnetic field computation," *Trans. on Magnetics,* vol. 42, pp. 1996-2003, 2006.

[52] M. Xu and N. Ida, "Solution of magnetic inverse problems using artificial neural networks," in *Proc. 6th Int. Conf. Optimization Electr. Electron.Equipments*, 1998, pp. 67-70.

[53] J. T. Nenonen, "Solving the inverse problem in magnetocardiography," *IEEE Engineering in Medicine and Biology,* vol. 13, pp. 487-496, 1994.

[54] K. Bai, J. Ji, K.-M. Lee*, et al.*, "A two-mode six-DOF motion system based on a ball-joint-like spherical motor for haptic applications," *Computers and Mathematics with Applications,* vol. 6, pp. 978-987, 2012.

VITA

Kun Bai was born in China, 1984. He received his B.S. degree in Control Science and Technology from Zhejiang University, China, in 2006. Upon graduation, he began graduate study at the George W. Woodruff School of Mechanical Engineering at the Georgia Institute of Technology, Atlanta, US in 2007. He completed his M.S. degree in December, 2009 and is a Ph.D. candidate from 2009 to 2012.

His research interests include mechatronics, automation and control systems, machine vision, sensing technology and dynamic systems. The research on control and sensing systems of spherical motors during his graduate study has led to publications at several international conferences and journals. Kun Bai is a student member of IEEE.